ANISOTROPIC SHOCK RESPONSE OF 1,3,5-TRIAMINO-2,4,6-TRINITROBENZENE (TATB)

A Dissertation Presented to

the Faculty of the Graduate School

at the University of Missouri

In Partial Fulfillment

of the Requirements for the Degree

Doctor of Philosophy

---

by

Puhan Zhao

Prof. Tommy Sewell, Dissertation Supervisor

December 2020

The undersigned, appointed by the Dean of the Graduate School, have examined the dissertation entitled:

ANISOTROPIC SHOCK RESPONSE OF
1,3,5-TRIAMINO-2,4,6-TRINITROBENZENE (TATB)

presented by Puhan Zhao,
a candidate for the degree of Doctor of Philosophy
and hereby certify that, in their opinion, it is worthy of acceptance.

Prof. Tommy Sewell

Prof. Andrey Peverezev

Prof. Zhen Chen

Prof. C. Michael Greenlief

Dr. Edward Kober

TO

My mother, 曲淑珍

My step-father, 于杰

My boyfriend, Michael N. Sakano

My cat, 粿粿

九萌，晴杀，以及初级中华火锅研讨会的所有会员们

ACKNOWLEDGMENTS

I would like to express my profound gratitude to my advisor Prof. Thomas (Tommy) Sewell for his continuous support and opportunities he has given me during my graduate life, for his patience, enthusiasm and immense knowledge, which guided and helped me throughout my study and research. The challenges and supervision from him helped bring the work in this dissertation toward completion. His style of "being extremely careful" and "paying extra attention to details" had a significant influence on me both as a scientist and as a person, and I could not have imagined having a better advisor and mentor.

I would like to give my sincere thanks to Dr. Edward Kober at Los Alamos National Laboratory for the opportunity of a summer internship in 2019. This unique experience had a profound impact on my professional life.

I am deeply in debt to Dr. Matthew Kroonblawd, Dr. Nithin Mathew and Dr. Shan Jiang for their stimulating discussions and insightful comments on my research. In particular, I owe Matt many thanks and much appreciation for his brilliant ideas and his inspiration to me. I would like to thank Dr. Andrey Pereverzev for his generous answers to my (sometimes stupid) questions. I am grateful to Win Grace for all her help and spiritual support on both my graduate life and my personal life.

I would also like to thank all my former colleagues on the 3^{rd} floor for their kindness. I could not have survived my graduate life without them.

Last but not the least, my sincere thanks go to the rest of my thesis committee: Prof. Zhen Chen and Prof. Michael Greenlief for their hard questions and valuable suggestions.

TABLE OF CONTENTS

LIST OF TABLES

Table Page

LIST OF FIGURES

Figure Page

ABSTRACT

The thermo-mechanical response of shock-induced pore collapse has been studied using non-reactive all-atom molecular dynamics (MD) and Eulerian continuum simulations for the molecular crystal 1,3,5-triamino-2,4,6-trinitrobenzene (TATB). Three crystal orientations, bracketed by the limiting cases with respect to the crystal structure anisotropy in TATB, are considered in the MD simulations, while an isotropic constitutive model is used for the continuum simulations. Simulations with three impact speeds from 0.5 km s^{-1} to 2.0 km s^{-1} are investigated. Results from MD and continuum simulations are in agreement in terms of shock wave speeds, temperature distributions, and pore-collapse mechanisms. However, differences arise for other quantities that are also important in hotspot ignition and growth, for example, the skewness of high-temperature distributions and the local temperature field around the post-collapse hotspot, indicating the urgent need to incorporate anisotropic crystal plasticity and strength models into the continuum descriptions.

The deformation mechanisms of TATB crystals in the shock-induced pore collapse MD simulations were studied using Strain Functional Analysis. This new approach maps discrete quantities from atomistic simulations onto continuous fields *via* a Gaussian kernel, from which a unique and complete set of rotationally invariant Strain Functional Descriptors (SFD) is obtained from the high-order central moments of local configurations, expressed in a Solid Harmonics polynomial basis by SO(3) decomposition. Coupled with unsupervised machine learning techniques, the SFD successfully identifies and distinguishes the deformations presented in the MD simulations of shock-compressed TATB crystals. It enables automated detection of disordered structures in the system and can be readily applied to materials with any symmetry class.

Chapter 1

Introduction

1.1 Motivation

The study of energetic materials (EMs) has been the topic of much practical interest for centuries, especially since the 1940s. The first known chemical explosive (a.k.a. black powder), which consists of a mixture of sulfur, charcoal, and potassium nitrate, was discovered as a by-product of "elixir of immortality" by ancient Chinese alchemists in the 6^{th} century.[2] The usage of black powder was later replaced by the smokeless dynamite invented by Alfred Nobel in the 19^{th} century. Its stability and low cost led to its wide use during World War I (WWI). Nowadays, EMs are used for military purposes as well as in the field of civil engineering, such as mining and construction. The search for EMs that provide better performance, are safer to handle, and can be manufactured at a lower cost has never ended. And, of course, understanding of the thermal and mechanical responses of the EMs under perturbations is key to knowledge-based improvements in that direction.

Computer simulations offer a safer and more efficient way to obtain knowledge of

EMs under extreme conditions (*i.e.* high temperatures and high pressures). Many meso- and continuum-scale models have been parameterized (calibrated) against experimental data, aiming for accurate descriptions of the thermal and mechanical behaviors of EMs. However, the lack of well-controlled experimental characterization and diagnostics at the mesoscale has hampered efforts to build high-fidelity constitutive descriptions. Fortunately, molecular dynamics (MD) can help fill in some of the gaps in our knowledge and understanding. The focus of this dissertation is on the thermal and mechanical response of 1,3,5-triamino-2,4,6-trinitrobenzene (TATB) crystal under shock compression. Oriented single crystals, either initially defect-free or containing a cylindrical pore, were studied for impact speeds between 0.5 km s^{-1} and 2 km s^{-1}. Both 'traditional' and machine learning techniques were applied for the analysis, which emphasized properties that can be compared to mesoscale continuum predictions.

1.1.1 Energetic materials

Energetic materials refer to substances that can rapidly release large amounts of energy under certain conditions. They are usually divided into three categories: explosives, propellants, and pyrotechnics.[3] Among these, explosives are the most vigorous in terms of reaction violence. For explosives, the rapid release of energy is usually accompanied by the production of hot gases and therefore a large expansion in volume.

Explosives are often classified into two groups based on the mechanisms of explosion: low and high explosives.[4] In low explosives, chemical reactions can build up to a subsonic deflagration wave, in which the propagation of the chemical reaction front through the sample is slower than the local speed of sound.[5–7] Low explosives typically consist of a mixture of fuel and an oxidizer. For example, the sulfur and charcoal

in black powder are the fuel, and potassium nitrate is the oxidizer. Confinement is often required for low explosives to detonate. Conversely, high explosives undergo detonation in the absence of confinement or atmospheric oxygen. They have the fuel and oxidizer in the same molecule (or formula unit in the case of ionic substances), allowing reactions to occur much faster. In a detonation, decomposition of the materials is propagated by shock waves that travel at supersonic speeds and cause abrupt changes in local temperature, pressure, and density of the materials.[5–7] Explosives can also be categorized into primary, secondary, or tertiary explosives based on their sensitivity. Compared with primary explosives, secondary and tertiary explosives are less sensitive to external thermal, mechanical, and electrical perturbations such as impact, friction, shock, and heat and release more energy once detonated.

High explosives often exist as molecular crystals containing nitro functional groups, in which a large amount of chemical potential energy is stored in the bonds. Some common molecular high explosives include nitromethane and nitroglycerin, pentaerythritol tetranitrate (PETN), octahydro-1,3,5,7-tetranitro-1,3,5,7-tetrazocine (HMX), hexahydro-1,3,5-trinitro-1,3,5-s-triazine (RDX), and TATB. These molecular high explosives are used in both civil engineering and military fields. Thus, it is important to understand the mechanisms involved in the ignition-to-initiation process leading to a detonation for the purposes of safety and performance. Among them, TATB is a fascinating case owning to its insensitivity, which makes it resistant to accidental detonations.

1.1.2 Shock waves

Humans have been using explosives in many fields for centuries with little understanding of the physics and chemistry behind them. We learned "how" by experience, but

even today we do not fully understand "why". Demands of explosives have shifted from simple task accomplishments to task accomplishments with higher precision and efficiency and maximum safety. We are no longer satisfied with making the explosives explode; rather, we want to understand why.

There was a great deal of studies, both theoretical and experimental, focused on explosives in the past,[6,8–13] trying to understand the sensitivity and performance of a given explosive, as well as the mechanisms behind a detonation. Eyring *et al.*[14] and Bowden and Yoffe[8] proposed one of the most accepted shock initiation theories in fluids and homogeneous solids. The initial shock wave acts like an inert shock, increasing the temperature and pressure of material behind the shock. Initiation later occurs in the compressed material behind the inert shock wave, generating a detonation wave that propagates through the compressed material (often from the impact surface, where heating of the explosives has been the largest) and eventually overtakes the initial shock wave. They argued that the bulk temperature for impact strengths just above the detonation threshold is insufficient for initiation in homogeneous explosives. Since detonation usually takes place as a thermal explosion, "hotspot" formation (*i.e.* localization of high temperature and high pressure) has a significant impact on this initiation-to-detonation process. This theory of thermal explosion and the important role of hotspots were later confirmed experimentally by Campbell *et al.*[15] by tracking the trajectory of the shock and detonation waves in homogeneous explosives including liquid nitromethane, molten trinitrotoluene (TNT), molten diethanolnitramine dinitrate (DINA), and single crystals of PETN.

Whereas the detonation theory for homogeneous explosives is relatively straightforward, complications arise for systems containing defect structures, such as cracks, voids, or interfaces. Needless to say, the problem becomes extremely complex for plastic-bonded explosives (PBXs), which are heterogeneous consisting of explosive

crystallites, binders, plasticizers, and often other trace ingredients. Understanding of the laws governing shock wave propagation in explosives is foundational for understanding and predicting detonation phenomena.

Limited by experimental techniques, measurements of the thermo-mechanical properties of rapidly evolving shock-compressed explosives during the detonation initiation are not easy. A simple set of equations, known as the Rankine-Hugoniot (jump) conditions, which describe the states of materials ahead of and behind a shock wave, were developed by Rankine[16] and Hugoniot[17] for a one-dimensional (1D) system (see Figure 1.1). With the shock wave treated as a mathematical discontinuity and in a coordinate system that is moving with the shock front, the jump conditions can be expressed using the following equations:

Conservation of mass

$$\rho_1 \mathbf{u}_1 = \rho_0 \mathbf{u}_0 \equiv m, \tag{1.1}$$

Conservation of momentum

$$P_1 + \rho_1 \mathbf{u}_1^2 = P_0 + \rho_0 \mathbf{u}_0^2, \tag{1.2}$$

Conservation of energy

$$\epsilon_1 + \frac{P_1}{\rho_1} + \frac{\mathbf{u}_1^2}{2} = \epsilon_0 + \frac{P_0}{\rho_0} + \frac{\mathbf{u}_0^2}{2}, \tag{1.3}$$

where m is the mass flow per unit area per unit time, ρ is the density, $\mathbf{u}$ is the shock velocity, P is the pressure, and ϵ is the internal energy. The subscript "0" indicates unshocked material ahead of the shock front and "1" represents compressed material behind the shock front.

For shock waves in inert materials, the Hugoniot jump conditions are sufficient to

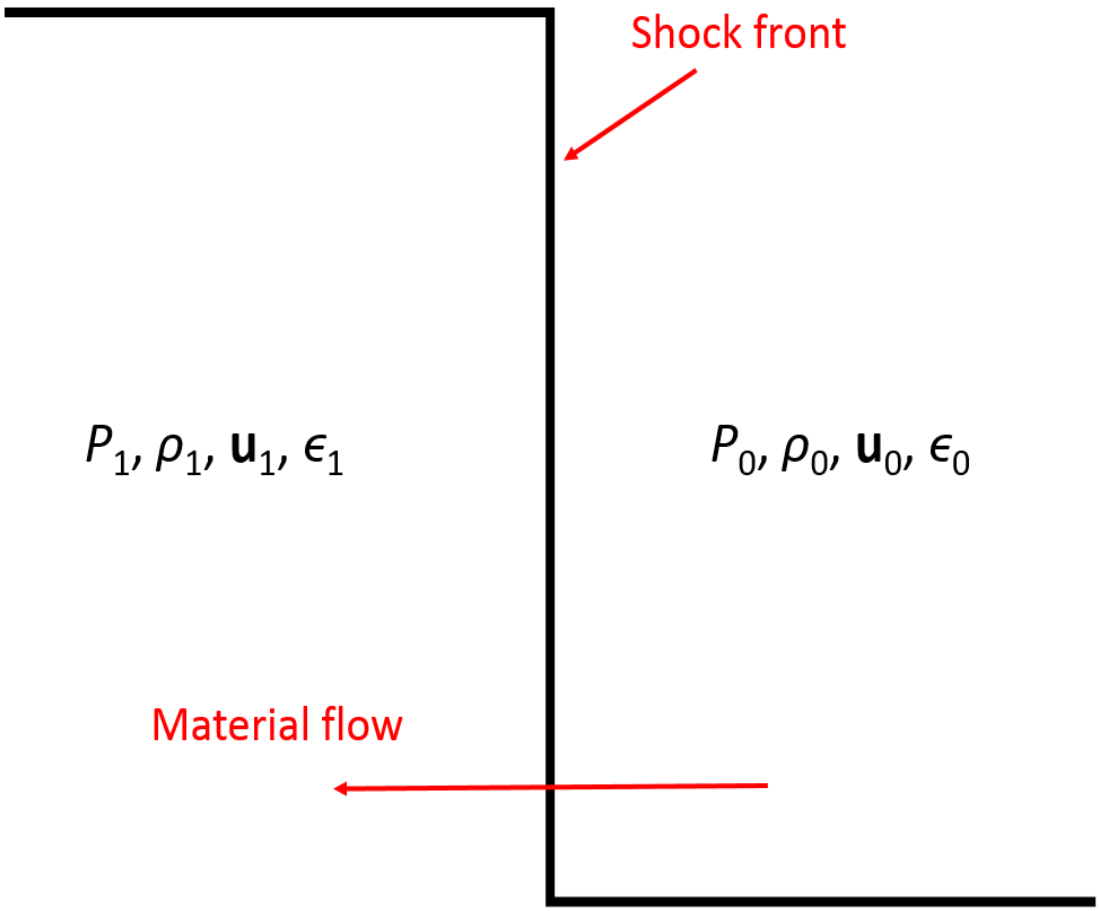

Figure 1.1: Depiction of a single shock wave in a 1D system. The shock front is stationary, and material flows from right to left.

determine the shock velocity $\mathbf{u}$ with known P, m, and ρ. The Hugoniot loci define a collective set of all the possible states of the material that can be reached by a single shock wave. The Hugoniot locus in a given state-state plane (such as P-ρ or P-$\mathbf{u}$) can be obtained by combining the Rankine-Hugoniot conditions with an equation of state for the material.

Taking the conservation of mass and momentum in Eqs. 1.1 and 1.2, one can obtain

$$\frac{P_1 - P_0}{\mathbf{u}_1 - \mathbf{u}_0} = -m. \tag{1.4}$$

With a constant shock velocity $\mathbf{u}$, Eq. 1.4 defines the Rayleigh line in the P-$\mathbf{u}$ plane. For a non-reactive system, the Rayleigh line intersects with the Hugoniot locus at (P_0, u_0) and at the final state (P_1, u_1) (Figure 1.2(a)). This is not true for a reactive system. The differences are well illustrated in Figs. 5 and 6 of Ref. 1 and also in Figure 1.2, where the initial and final states of the system are represented as intersections of the Hugoniot locus and Rayleigh line. Note that for an explosive, the Hugoniot locus does not pass through $P = 0$ (Figure 1.2(b)). Rather, the Rayleigh line for a high shock velocity (red dotted line) interacts the Hugoniot locus more than once, resulting in ill-defined final states for the system.

To resolve the ambiguity, Chapman[18] and Jouguet[19] separately developed the so-called CJ theory. It assumes that chemical reaction is completed at the shock front and the reaction zone has zero thickness. For a detonating high explosive, the shock wave is described as a self-sustained supersonic wave that travels through the material at a constant speed. An unsupported detonation, they argued, would have a minimum detonation velocity with non-zero pressure values. This minimum detonation velocity is given by the Rayleigh line that is tangent to the Hugoniot locus, and the intersection

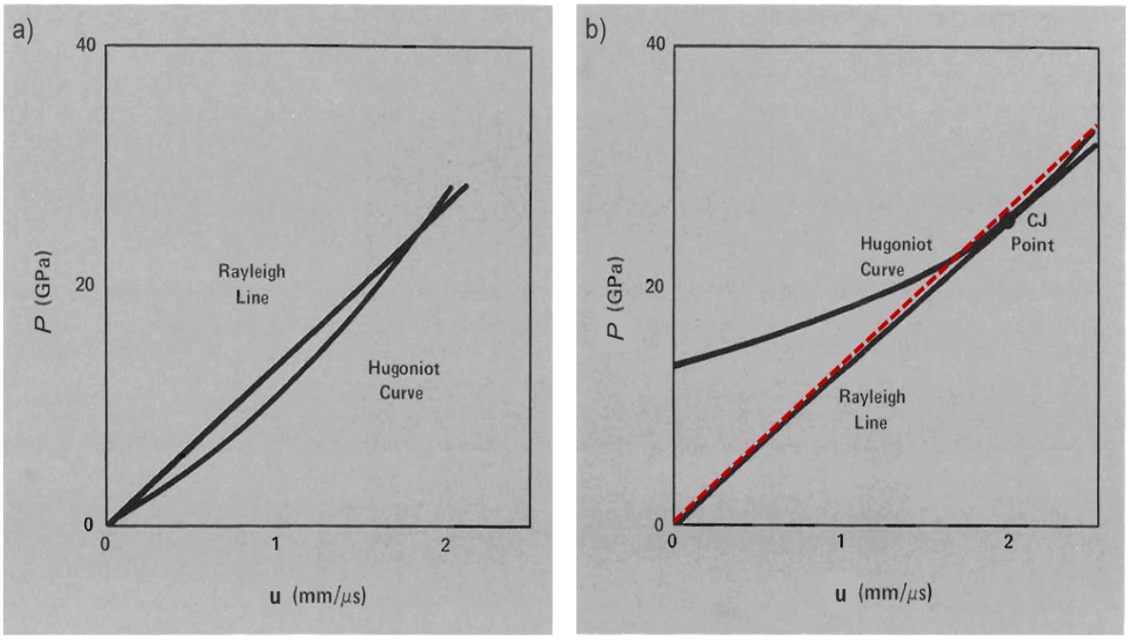

Figure 1.2: Hugoniot locus and Rayleigh line shown in the P-**u** plane for a) NaCl and b) an explosive. Red dotted line indicates a Rayleigh line with a higher shock velocity. This figure is taken from Ref. 1.

point, the CJ point, is the final state of the reacted explosives behind the detonation front.

The assumption of instantaneous completion of reaction in the CJ theory is not always true, especially for insensitive high explosives that have long reaction times, such as TATB and FOX-7 (1,1-diamino-2,2-dinitroethene). Zel'dovich,[20] von Neumann,[21] and Doering[22] independently developed a theory (a.k.a. ZND theory) that describes a detonation wave with a steady reaction zone. The shock wave is still treated as a discontinuity, but instead of assuming an instantaneous completion of chemical reactions behind the detonation front, an additional variable α, which describes the completeness of the chemical reaction, is included in the Rankine-Hugoniot conditions. This gives rise to multiple Hugoniot loci, each corresponds to a value of α for $0 \leq \alpha \leq 1$. The ZND theory predicts that the system is first compressed to

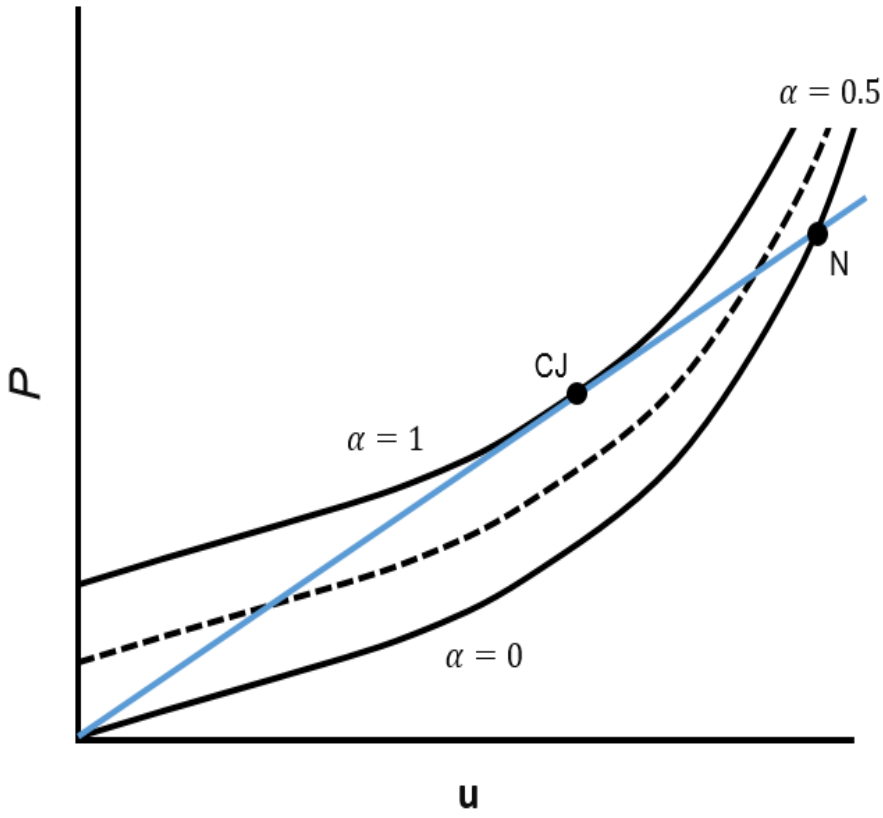

Figure 1.3: Three Hugoniot loci (black) with a Rayleigh line (blue) for a detonation predicted using the ZND theory. Zero α represents unreacted explosive, and $\alpha = 1$ for chemical reaction completion. Point N represents the von Neumann spike immediately behind the shock front.

a high pressure state, known as the von Neumann spike,[23] by the detonation wave passage, while the explosive remains unreacted. As chemical reactions begin, pressure decreases and volume expands; the state of the system follows the Rayleigh line and eventually reaches the CJ point (see Figure 1.3).

In the real world, the detonation process of explosives is much more complex than described by either the CJ or ZND theories. The variable α in the ZND theory implies a one-step chemical reaction with a single reaction rate. In fact, chemical reactions of explosives are often multi-step, multi-phase processes with many reaction rates. In addition, the theories focus only on waves propagating along the longitudinal

direction. The transverse waves are assumed to be planar, and the material is assumed to be homogeneous. The reality in a PBX is far more complex. Compression of the material and interactions of shock waves with the inhomogeneities in the explosives lead to non-uniform distributions of temperature and pressure. The inhomogeneities and their reaction zones are thought to have a large effect on the chemical reaction rate and the final state of the system.

1.1.3 Energy localization (hotspots)

The structural inhomogeneity of PBXs is much more complex than pure explosives mainly due to the presence of explosive crystallites embedded in a continuous binder phase. This leads to non-uniform distributions of temperature and pressure, which affect chemical reaction rates, in a coupled fashion, and lead to complex detonation phenomena. It is thought that the bulk temperature in a solid explosive just above its shock threshold is not sufficiently high for an initiation; instead, interactions between the shock wave and the microstructural defects behind the shock lead to energy localization (generation of "hotspots"), where chemical reactions begin, and ignition (local burning) in the materials. Initiation takes place if the ignition is strong enough to form a reaction shock front and lead to detonation. (Here, we use the definitions of "ignition" and "initiation" defined by Bourne.[24]) Properties of hotspots, such as the size, distribution, and formation mechanism and interactions among them, thus have a significant impact on this ignition-to-initiation process.

Hotspot formation mechanisms then become essential for predicting detonations. Field[25,26] and Davis[1] have proposed several hotspot formation mechanisms for shock initiation in solid high explosives, including adiabatic compression of trapped gases, cavity collapse, sliding of surfaces, shear, viscous heating, plastic deformation, struc-

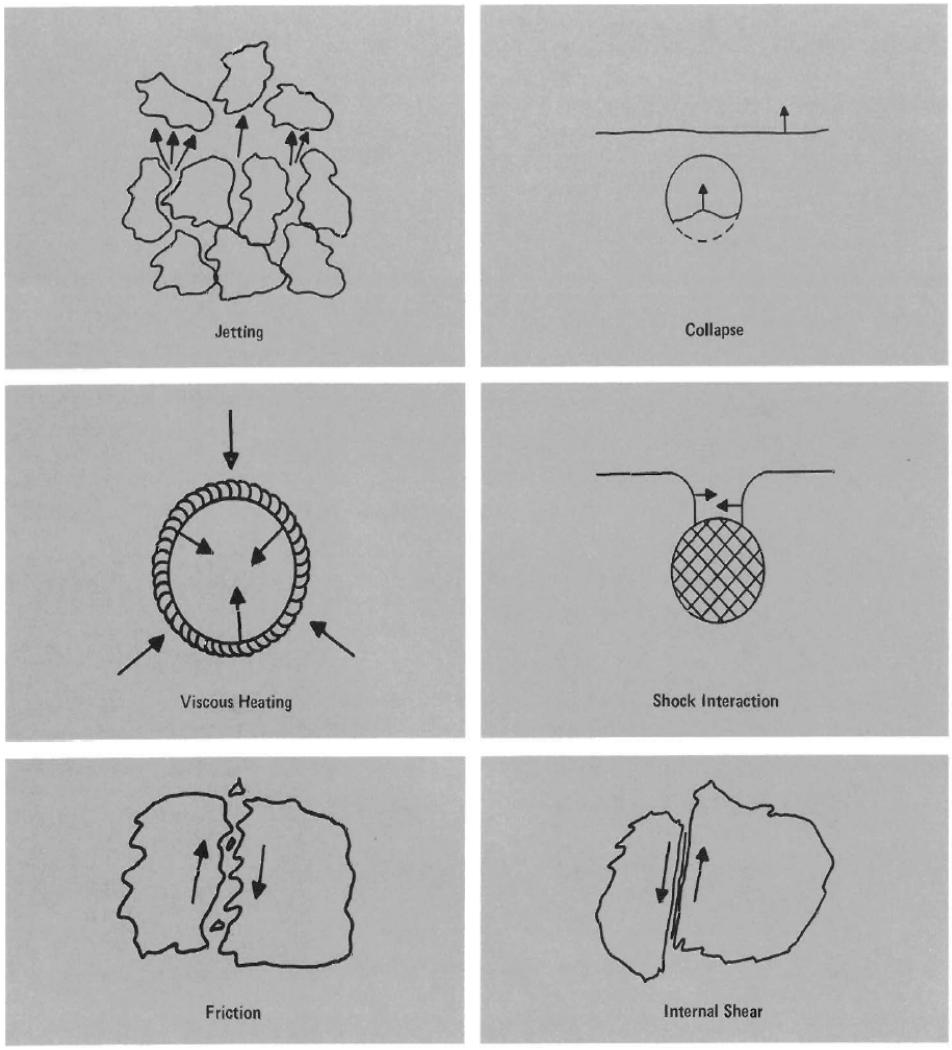

Figure 1.4: A Depiction of hotspot formation mechanisms from Ref. 1.

tural decomposition, and jetting. Several mechanisms mentioned above are captured in Fig. 25 of Ref. 1 and also in Figure 1.4 in this dissertation. Which one(s) will predominate in a given scenario will depend on external conditions and initial material state (composition, microstructure, damage, etc.). Therefore, understanding of them and predicting which one(s) apply in a given case help form the basis for both fundamental and applied studies.

1.2 Method

1.2.1 Molecular dynamics overview

Ignition-to-initiation is a multiscale process, involving phenomena across a broad spectrum of spatial and temporal scales. Precisely monitoring such multiscale processes is beyond the currently available experimental capabilities, especially at the extremely small spatial (Å) and temporal (fs) scale. Molecular dynamics (MD) focuses at the atomistic scale and aims to provide a better understanding of the phenomena by using (usually) analytical potential functions to solve the classical equations of motion for each particle in the system. Positions and momenta can be computed with high fidelity, along with anything else that can be expressed in terms of them; thermomechanical properties such as temperature, stress, strain, and so on.[27,28] MD simulations have been widely used in studies of EMs, including but not limited to spectroscopic analysis,[29–35] calculations and analysis of thermodynamic properties,[36–46] shock responses,[47–59] and chemical decomposition processes.[59–69]

A typical MD simulation usually contains three main components: initial conditions, integration of trajectories, and analysis. Initial conditions of the system refers to the initial phase space coordinates of the particles in the system. Motion of each particle is governed by the potential function:

$$\mathbf{F} = m\mathbf{a} = -\nabla U \tag{1.5}$$

where U is the potential energy function. The force $\mathbf{F}$, hence the position and momenta of the particles, at each instance can be calculated from Equation 1.5. The trajectory of each particle in the system is solved using an integration algorithm and a time step of interest. Properties including positions, momenta, and energies can be

outputted directly by the program or computed during post-processing.

Initial conditions of a system must be specified prior to the beginning of a simulation (solving a classical trajectory is an initial-value problem). For molecular crystals, the desired simulation cell can be constructed by taking the atomic coordinates of the unit cell and replicating along the crystal axes. Orthorhombic simulation cells are often preferred in shock simulations due to simplicity for construction and analysis. However, the low symmetry of molecular crystals makes such generation of simulation cells less straightforward. Kroonblawd *et al.*[70] have developed a Generalized Crystal-Cutting Method (GCCM), which enables automatic construction of 3D periodic orthorhombic simulation cells of any crystal described by Bravais lattices while preserving the underlying translational symmetry. The GCCM loop-searches for the most orthorhombic unit cell with the new crystal axes aligning with the desired direction in the Cartesian frame. This *generalized* unit cell can be further replicated into larger ones for simulation purposes. All simulation cells in this dissertation were constructed using the GCCM.

The primary simulation cell length varies from the order of tens to thousands of Å. Shorter cell lengths are sufficient for calculating physical properties such as elastic tensors,[71,72] lattice parameters,[72] and studies of vibrational mode excitation.[31] Cell lengths on the order of thousands of Å are often needed along the shock direction in explicit shock simulations to allow evolution of events happening behind the shock front.[50,51,73] However, this scale is still far too small to represent defects and extended interfaces in real materials. Periodic boundary conditions (PBCs)[27] are applied to reduce the finite-size effect, but even so, the longest wavelength phenomenon that can be simulated is limited by the size of the primary cell. Care needs to be taken to prevent artifacts when applying the PBCs. For example, a simulation cell consisting a liquid with 3D PBCs is essentially a repetitive "crystal structure" of such liquid

(unit cell).

In addition, well-defined integration algorithms and appropriate choice of time step, along with many other parameters, are keys to performing meaningful MD simulations. Among the various available integration algorithms, velocity Verlet[74,75] is the most commonly used due to its high accuracy and high efficiency.[76] The integration time step needs to be chosen with care. While a smaller time step can be computationally expensive, a time step that is too large may fail to provide proper resolution of the evolution of the system and lead to inaccurate solutions of the equation of motion.

With proper initial conditions and appropriate parameters, desired simulations can be performed using various statistical ensembles, such as microcanonical (NVE), canonical (NVT), and isothermal-isobaric (NPT). N is the number of particles in the system, V is the volume, P is the pressure, T is the total temperature, and E is the total energy of the system. Letters inside the parentheses are parameters that are held constant during the simulation. In this dissertation, thermal equilibration is performed using the NVT ensemble in order to obtain a representative sample at a finite temperature. Atomic positions, velocities, and forces are computed using LAMMPS[77,78] with an appropriate frequency of data recording for subsequent analysis. More details are included in Chapter 2 and Chapter 3.

1.2.2 MD shock simulations

At the atomistic level, shock waves are often studied using molecular dynamics (MD) simulations.[79] The steady profiles of properties in MD simulations are ideal for studies of the thermo-mechanical shock response of condensed fluids and solids.[80] In principle, there are three major ways to generate a shock wave in a MD simulation of solids:

(i) inertial flyer-plate, (ii) piston-driven, and (iii) reverse-ballistic.[80]

Using the first method, a shock wave can be generated by assigning the flyer plate a velocity of $2\mathbf{u}_\mathrm{p}$ traveling toward a stationary target (Figure 1.5(a)). Upon contact, shock waves moving in opposite directions can be generated in the two plates. The magnitude of the particle velocity is equal to $\mathbf{u}_\mathrm{p}$ in both samples if the two plates are identical, as shown in Figure 1.5(b). This method is more similar in spirit to experimental work than the other two methods. On the other hand, larger sample sizes may be needed in order to study the shock response of materials well behind the shock, which can be computationally expensive.

In a piston-driven configuration, the material is compressed by an infinitely massive piston moving at a constant velocity $\mathbf{u}_\mathrm{p}$. The material and the piston travel in the same direction. The systems for flyer-plate (Figure 1.5) and piston-driven (Figure 1.6) configurations are identical. Due to the difference in the ways that shock waves are generated, the amount of material behind the shock wave is greater in the piston-driven configuration compared to the flyer-plate configuration. Hence, this method is more ideal for studies of the long-time shock response of the material (*i.e.*, propagation and growth of deformations, and initiation of chemical reactions).

Similar to the piston-driven configuration, in the reverse-ballistic configuration, an infinitely massive piston is defined prior to the shock simulation. An illustration is shown in Figure 1.7. The material impacts the stationary piston with a velocity of $-\mathbf{u}_\mathrm{p}$, generating a shock wave traveling through the material in the opposite direction. The positions of particles in the lab frame of the piston-driven configuration and the reverse-ballistic configuration are related by a simple Galilean transformation. In particular, the relative positions of the atoms as functions of time are the same in both cases. Though both of the methods are suitable for studies of the shock response of material, it is easier to study the relaxation of shock-compressed material using

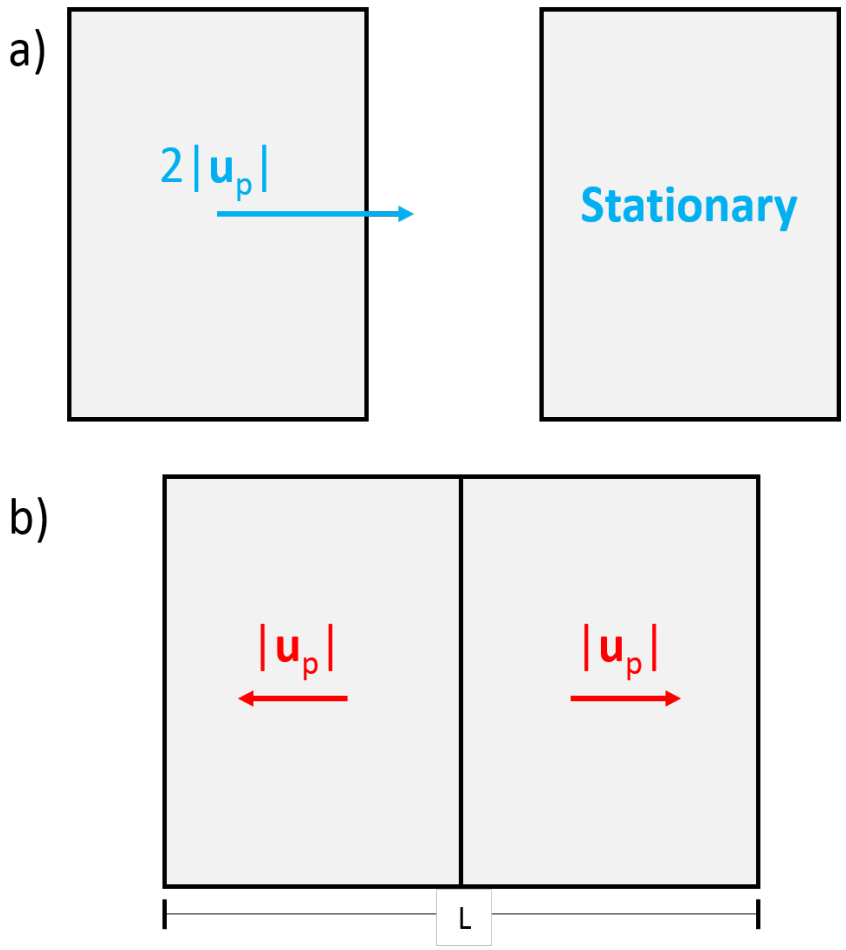

Figure 1.5: Depiction of a flyer-plate configuration for shock simulations at times a) before and b) after the flyer-plate hits the stationary sample. Waves with same particle speed but propagating in opposite directions are generated in two plates if sample masses are identical.

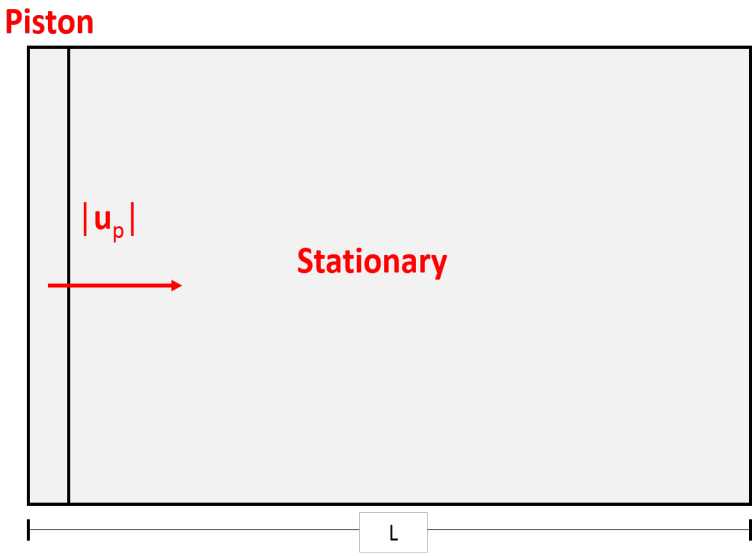

Figure 1.6: Depiction of a piston-driven configuration of shock simulations. The infinitely massive piston compresses the initially stationary sample with a constant velocity.

the later configuration by allowing the sample to recover to its original shape.

Other methods, including the moving window (MW) MD simulations[81] and the multiscale shock technique (MSST),[82] are often used in studies of shock response as well. In the MW MD simulations, the MW travels at the shock speed. Unshocked material is fed into the MW from one end and shocked material is removed from the other end. Shock waves can be simulated for an "infinite" amount of time, thus decoupling the system length and time scales in the simulations. The multiscale shock technique combines MD with continuum simulations (Euler's equations). It enables a much longer simulation time (ns) than MD does by simulating the shock wave passage using a continuum description, and the energies (*i.e.*, kinetic and potential) of the compressed system are obtained from a representative sample of the system in the MD simulation. No *a priori* knowledge of the system, such as sound speed or phase diagram, is required for such approach. This is a step forward in closing the spatial and temporal gaps between MD and continuum.

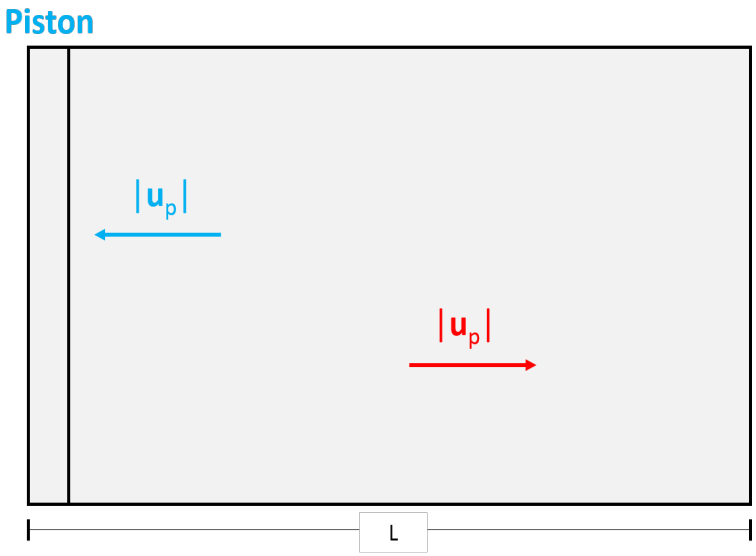

Figure 1.7: Depiction of a reverse-ballistic configuration for shock simulations. The sample hits the infinitely massive piston (which is held stationary throughout the simulation) with a constant particle velocity in order to generate a shock wave that travels in the opposite direction.

1.3 TATB

This dissertation focuses on the thermal and mechanical response of the molecular crystal 1,3,5-triamino-2,4,6-trinitrobenzene (TATB) under shock compression. Despite a large number of studies focusing on TATB under compression, there are still gaps in understanding the deformation mechanisms of this crystal. Few fundamental experimental data are available owning to the difficulties to synthesize high-quality single crystals of desired sizes. Numerical modeling thus becomes essential for studying the response of TATB under loading. Indeed, thermal and mechanical properties and shock response of single TATB crystals obtained from the atomistic scale MD simulations have become key components in building mesoscale models.[83,84]

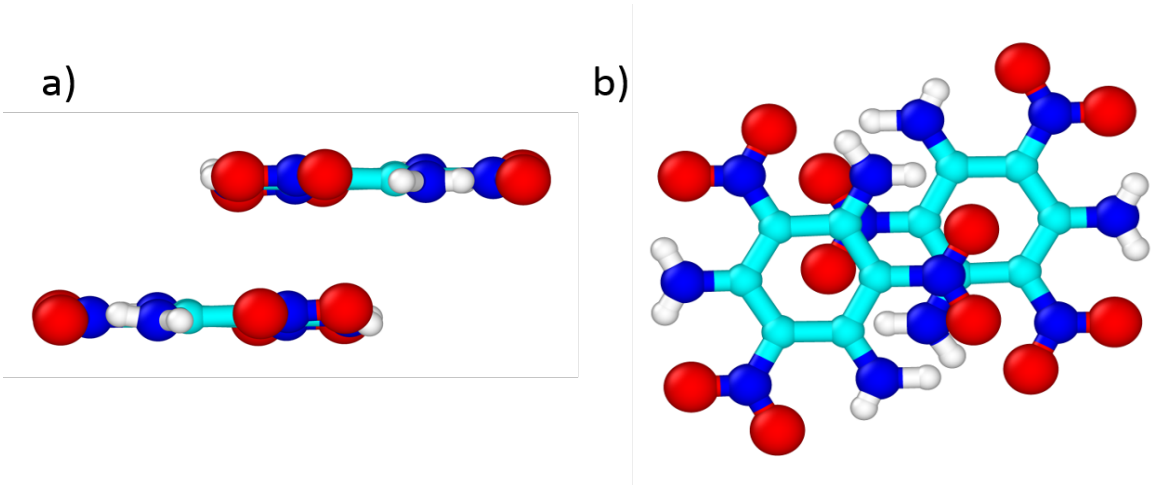

Figure 1.8: a) Side and b) top view of a TATB unit cell. Carbon atoms are shown in cyan, nitrogen atoms are shown in navy blue, oxygen atoms are shown in red, and hydrogen atoms are shown in white.

1.3.1 Crystal structure

1,3,5-triamino-2,4,6-trinitrobenzene (TATB) is an insensitive high explosive (IHE) with color ranging from transparent to yellow.[85] It is a layered triclinic crystal of $P\bar{1}$ space group at standard ambient conditions, with two molecules per unit cell.[85] A depiction of the TATB unit cell is shown in Figure 1.8. The planar TATB molecule consists a benzene ring bonded with alternating nitro (-NO_2) and amine (-NH_2) groups. Molecules within a layer are held together by strong hydrogen bonding, while there are only van der Waals interactions between the molecular layers. The distinct interactions, the graphitic-like molecular layers, and the low symmetry crystal structure together contribute to the highly anisotropic thermal and mechanical properties of TATB single crystal.[36,37,86] Previous studies[86–96] have shown that the crystal structure of TATB remains triclinic under high pressures. Recently, Steele *et al.*[97] discovered a pressure-induced phase transition in TATB, where the crystal structure becomes monoclinic around 4 GPa. This subtle transition is induced by an in-plane shift of molecular layers.

Experimentally synthesized perfect single crystals of TATB are rare and almost always exhibit large defects and impurities.[98–101] Difficulties in obtaining perfect crystals lead to the absence of experimental data of TATB single crystals. Hence, numerical modeling such as MD simulations plays a crucial role in understanding its thermal and mechanical behavior.

1.3.2 TATB force field

As mentioned earlier in Equation 1.5, the motions of particles in a MD simulation are governed by the potential energy surface of the system. Interactions between each particle and its neighbors are described with a set of mathematical equations. A common many-body force field (FF) often includes descriptions for covalent bonds, three-center angles, dihedral angles, and improper dihedral angles. The chemical structure of TATB is shown in Figure 1.9. The connectivity between atom C_1 and C_2 defines a single covalent bond; atoms C_1, C_2, and C_3 define a three-center angle; atoms C_1, C_2, C_3, and N_9 define a dihedral angle. An improper dihedral angle is the angle between two planes defined by different groups of atoms, such as the angle between the plane defined by atoms C_1, C_2, and C_3, and the plane defined by atoms C_2, C_3, and C_4. Non-bonded terms are also included to describe any interactions between atoms that do not belong to the categories mentioned above. These are typically of atoms belonging to the same molecule but separated by more than two covalent bonds (*i.e.*, 1-4 interaction) and intermolecular interactions between atoms that do not belong to the same molecule. The total potential energy of an isolated system is the sum of bonded and non-bonded terms.

Various non-reactive force fields have been developed for TATB.[86,102,103] Gee *et al.*[102] proposed a quantum-based fully-flexible FF based on high-level *ab initio* single-

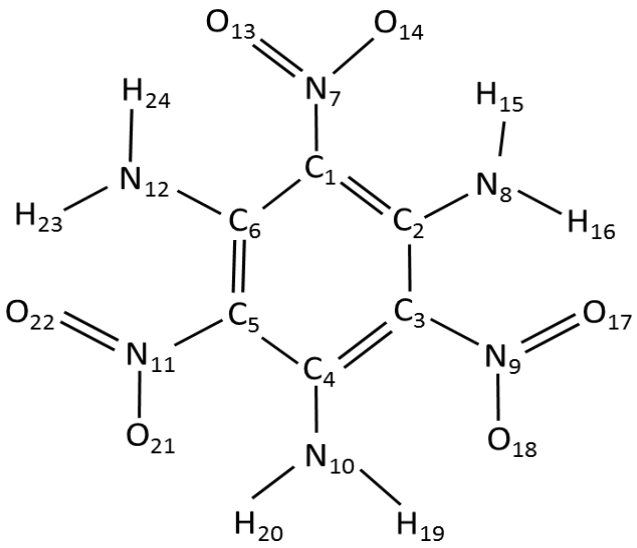

Figure 1.9: 2D chemical structure of a TATB molecule.

point energy calculations. At the opposite extreme, Rai *et al.*[103] treated TATB molecules as rigid. The Rai *et al.* FF was constructed via parameterization of the transferable potentials for phase equilibria (TraPPE[104]) of nitrobenzene ($C_6H_5NO_2$) and aniline ($C_6H_5NH_2$). An all-atom FF with constrained bonds (both polarizable and non-polarizable versions) has been developed by Bedrov *et al.*,[86] and later refined by Kroonblawd *et al.*[36] with flexible bonds. In this force field, all intramolecular non-bonded interactions are excluded, except the repulsion between O and H atoms.[39] This FF has been shown to reproduce the crystal lattice parameters[85] and vibrational spectra.[36] Mathew *et al.*[39] obtained the heat of sublimation of TATB using such FF, and the results are in close agreement with the experiments. This FF has also been implemented in the studies of thermal conductivity,[36,37,41] energy exchange,[40] hot-spot relaxation,[43] nanoidentation,[42] stacking-fault energy calculation,[38] melt curve prediction,[44] dislocation core structure,[105] and deformation mechanisms.[106]

The non-polarizable TATB FF implemented in this dissertation has the following form

$$U(r,\theta,\phi,\chi,R) = \sum_{bond} U_{\text{bond}}(r) + \sum_{angle} U_{\text{angle}}(\theta) + \sum_{dihedral} U_{\text{dihedral}}(\phi) + \sum_{improper} U_{\text{improper}}(\chi) + \sum_{atom\ i} \sum_{atom\ j>i}{}' U_{\text{NB}}(R) \tag{1.6}$$

$$U_{bond} = \frac{1}{2} k_{bond}(r - r_0)^2 \tag{1.7}$$

$$U_{angle} = \frac{1}{2} k_{angle}(\theta - \theta_0)^2 \tag{1.8}$$

$$U_{dihedral} = \frac{1}{2} k_{dihedral}[1 - cos(n\phi)] \tag{1.9}$$

$$U_{improper} = \frac{1}{2} k_{improper}(\chi - \chi_0)^2 \tag{1.10}$$

$$U_{NB} = Ae^{-BR} - \frac{C}{R^6} + D(\frac{12}{BR})^{12} + \frac{q_i q_j}{4\pi\epsilon_0 R} \tag{1.11}$$

where bonds, angles, and improper dihedrals are described using harmonic functions, dihedrals are modeled using a truncated cosine function, and non-bonded intermolecular interactions are described using a Buckingham-plus-Coulomb (exp-6-1) term. The very-short-range repulsive term ($1/R^{12}$) described by Bedrov *et al.*[86] is included to prevent possible 'overtopping' due to the Buckingham potential term at short distances.[84] See Appendix I for the implementation of the non-bonded term in LAMMPS, and Appendix II for a complete list of the LAMMPS coefficients corresponding to Appendix I.

1.3.3 Thermal properties

Classical MD simulations have been widely used in determining the thermo-mechanical properties of TATB single crystals. The graphitic-like molecular-layer structure, owning to the strong inter- and intramolecular hydrogen bonding within the layers and the weak van der Waal interactions between the layers, is believed to be responsible for the highly anisotropic thermal and mechanical properties of TATB. Thermal conductivity of TATB has been well studied by Kroonblawd and Sewell for single crystals with[37] and without[36] defects, and its dependence on pressure and temperature and sensitivity to intramolecular FF.[41] Three independent directions were considered for the study of thermal conductivity within the perfect (defect-free) single crystals with a reverse non-equilibrium MD method.[107] Using a fully-flexible FF,[36] they predicted that the thermal conduction within the molecular layers is approximately 1.7 times greater than between the layers. The thermal conductivity of crystalline TATB is similar to other organic molecular crystals, such as RDX and HMX, but exhibits significant anisotropy. In addition, they extended the study to assess the finite-size and molecular vacancy effects on the anisotropic thermal conductivity.[37] The study revealed that thermal conductivity within the molecular layers is invariant with respect to the supercell length, and conduction between the layers decreases with increasing system length. This counterintuitive result may be caused by nanoscale structural transitions along that direction. In addition, they predicted that the thermal conductivity decreased with increasing vacancy defects density in the sample. Kroonblawd and Sewell also investigated the effect of pressure (0.0 GPa to 2.5 GPa) and temperature (200 K to 700 K) on the thermal conductivity, and its sensitivity to intramolecular FF.[41] The thermal conductivity is predicted to increase with increasing pressure and decrease with increasing temperature. In both cases, the effect is highly anisotropic. An isotropic reduction in the conduction is observed when the high-frequency N-H

bond vibrations are removed.

Kroonblawd and Sewell have compared the hotspot relaxation in crystalline TATB using MD simulations with both analytical and numerical solutions of the diffusive heat equations at the continuum-level.[43] Two conduction directions were considered based on the results from their previous work: directions nominally within and between the molecular layers. Energy transfer was found to be primarily diffusive for both directions. Excellent agreement between MD and analytical solution was observed for conduction normal to the crystal layers, whereas some discrepancies for direction nominally within the layers were settled by introducing a temperature-dependent thermal conductivity in the heat equation.

The rate of energy exchange between inter- and intramolecular degrees of freedom in crystalline TATB was studied using MD simulations by Kroonblawd *et al.*[40] Comparisons on the exchange rates of intermolecular potential energy and translational kinetic energy between MD simulation and a coarse-grained Dissipative Particle Dynamics at constant Energy (DPDE) model were used to parameterize the friction term in the DPDE model. Two out of the three values of the parameter yielded "reasonable" results compared to all-atom MD. The effects of the parameter on the shock response of TATB single crystals were further investigated, and the mechanical behavior was found to be greatly influenced by the rate of energy exchange.

Melting of TATB single crystals with (100), (010), or (001) face exposed to vacuum was studied using MD simulations.[44] The normal melting temperature of TATB is predicted to be 851 ± 5 K, which is 17.7% higher than the experimental result of pressed-powder TATB.[108] Melting of the (001) face was incomplete with superheating above the melting temperature. Molecular vacancies at the crystal-vacuum interface were observed prior to the complete loss of order of the molecular layers and melting at the surface.

1.3.4 Mechanical properties

Due to the difficulties in obtaining perfect single crystals for experimental testing, many mechanical properties of TATB single crystal have been studied using simulations. The anisotropic crystal structure (extended hydrogen-bonding within the molecular plane) has been held responsible for the extremely anisotropic mechanical properties of TATB single crystal.

Knowledge of structural defects and inelastic deformation mechanisms are important in understanding the hotspot formation and initiation in energetic materials. Inelastic deformation mechanisms for similar layered crystals are often due to dislocation glide along planes parallel to the molecular layers (also referred as the basal plane).[109] In addition, dislocations in layered crystals are usually found to dissociate into partials,[109,110] which are governed by the stacking fault energies. To learn more about these properties of TATB single crystals, Mathew *et al.*[38] calculated the generalized stacking fault energies curves for the two glide plane types in the (001) basal plane at 0 K. A low-energy stacking fault and twinning are reported to be stable at pressures of both 1 atm and 5 GPa. Easy glide of dislocations in the basal plane and low critical stresses for dislocation motion are predicted at 1 atm. Additionally, slip along the crystallographic **a** direction is shown to be preferable over the **b** or **a-b** directions in TATB.

Mathew and Sewell[42] further investigated the elastic/plastic deformation mechanisms of TATB through nanoindentation at 77 K and 1 atm. Displacement-controlled indentations were performed on (100), (010), and (001) planes using a rigid, spherical indenter. A Hertzian response was observed for indentation on the basal ((001)) plane with plastic deformation: kinking and delamination of the basal plane with significant pile-up. A non-Hertzian response was predicted for the (100) and (010) planes with elastic bending of the molecular layers and much less pile-up compared to that on

the basal plane. An upper-bound Meyer's hardness of 1.02 ± 0.09 GPa was obtained. Recently, the first mechanical experiment (nanoindentation) on TATB single crystal was conducted by Taw *et al.*[111] using high-quality crystals. They reported a similar modulus compared to MD prediction, but a much smaller hardness. Notice the hardness reported by Mathew and Sewell is the upper-bound hardness. This study is a major step in experimental work on TATB single crystals and has significantly shortened the distance between experiments and simulations.

More recently, Lafourcade *et al.*[106] characterized the irreversible deformation mechanisms of TATB single crystals by applying uniaxial compressions and pure shear that span all possible orientations using MD simulations. By examining a total of 84 deformation paths, a 3D deformation contour was obtained including three distinct zones that correspond to gliding in the transverse (non-basal) planes, (001) basal plane gliding, and chevron-like deformation. This molecular buckling, microtwinning deformation mechanism was described as large stacking fault ribbons[105] and was observed in studies of shock-compressed oriented TATB single crystals, as well.[112]

1.3.5 MD shock simulations of TATB

The first shock simulation on TATB crystals using MD was reported by Fried and Tarver back in 1995.[113] The two-dimensional system studied consisted of planar sheets of TATB crystal with various degrees of porosity. A shock Hugoniot ($\mathbf{u}_\mathrm{s}$ vs. $\mathbf{u}_\mathrm{p}$ curve) was obtained for systems without pre-existing molecular vacancies. A decrease in shock velocity and a rise of temperature were observed with an increase of porosity.

Chemical reaction kinetics of TATB crystals were studied by Long and Chen with ReaxFF[68,114] (a force field that includes reactions).[115] More than 450 intermediate molecules were identified, among which some were believed to play a significant role

in determining the reaction path. A complete description of the detonation wave structure, from the lead shock wave to the fast reaction zone to the slow reaction zone behind the shock, was obtained through a combination of integrating both non-reactive (MD) and reactive (reaxFF) results with Hugoniotstat, JWL equation of state, and the CJ states (calculated using continuum models).

A very recent conference proceeding showed comparison in shock-induced pore collapse in TATB single crystal using MD and continuum models.[83] The anisotropic elastic/plastic response of TATB was incorporated by including slip mediated deformation mechanisms in the hydrocode. Quasi-2D systems of three crystal orientations of TATB were performed using MD simulations. The agreement between the MD and continuum predictions has shown much improvement due to the implementation of dislocation-based plasticity.

1.4 Dissertation outline

This dissertation focuses on the study of the thermo-mechanical shock response of oriented TATB crystals using MD simulations. The rest of the document is organized as follows: Chapter 2 will focus on the shock-induced pore collapse in oriented TATB crystals.[84] The orientations were selected based on results from our previous work on shock-compressed oriented TATB single crystals.[112,116] The continuum calculation of pore collapse was part of a collaborative effort performed by Prof. Udaykumar's group at University of Iowa. Application of the Strain Functional Analysis to the simulation results from Chapter 2 will be explored in Chapter 3. Chapter 4 will provide useful information and helpful tips on performing MD simulations using LAMMPS. Chapter 5 will conclude the current work and discuss possible future directions.

Chapter 2

Tandem Molecular Dynamics and Continuum Studies of Shock-Induced Pore Collapse in TATB

2.1 Abstract

All-atom molecular dynamics (MD) and Eulerian continuum simulations, performed using the LAMMPS and SCIMITAR3D codes, respectively, were used to study thermo-mechanical aspects of the shock-induced collapse of an initially cylindrical 50 nm diameter pore in single crystals of 1,3,5-triamino-2,4,6-trinitrobenzene (TATB). Three impact speeds, 0.5 km s^{-1}, 1.0 km s^{-1} and 2.0 km s^{-1}, were used to generate the shocks. These impact conditions are expected to yield collapse mechanisms ranging from predominantly visco-plastic to hydrodynamic. For the MD studies, three crystal orientations (relative to shock-propagation direction) were examined that span the limiting cases with respect to the crystalline anisotropy in TATB. An isotropic

constitutive model was used for the continuum simulations, thus crystal anisotropy is absent. The evolution of spatio-temporally resolved quantities during collapse are reported including local pressure, temperature, pore size and shape, and material flow. Multiple models for the melting curve and specific heat were studied. Within the isotropic elastic/perfectly-plastic continuum framework and for the range of impact conditions studied, the specific heat and melting curve sub-models are shown to have modest effects on the continuum hotspot predictions in the present inert calculation. Treating the MD predictions as 'ground truth', albeit with a classical rather than quantum-like heat capacity, it is clear that—at a minimum—extension of the constitutive model to account for crystal plasticity and anisotropic strength will be required for a high-fidelity continuum description.

2.2 Introduction

Detonation initiation in plastic-bonded explosives (PBXs) is a complex phenomenon involving the interplay among microstructure, mechanics, and chemistry. PBX materials are microscopically heterogeneous, highly filled (>90% w/w) polymer composites. The filler consists of high-explosive (HE) crystallites with irregular shapes and orientations, and a range of particle sizes that often exceeds three orders of magnitude from roughly $(0.1\text{ mm})^3$ to 1 μm^3 and possibly much smaller. The energetic crystals are embedded in a continuous-phase polymeric binder matrix that confers mechanical stability and partially mediates the sensitivity. The crystals are elastically soft but plastically brittle, and often exhibit substantial thermo-mechanical anisotropy and internal defect structures such as chemical impurities, dislocations and twins, empty or filled pores, and fracture surfaces. The binder is a visco-elastic/plastic fluid under standard ambient conditions. The composite is rife with crystal-binder,

crystal-crystal, and (crystal or binder)-pore interfaces as well as those associated with the intra-crystalline defect structures. The size of a representative volume element (RVE) of a PBX material, for purposes of shock initiation, is of the order of a few mm^3. Such an RVE contains a heterogeneous mixture of crystals and binder that, with appropriate homogenization, can be modeled as a continuum. For point of reference, using the unit cell of β-HMX as an example, a cube of crystal with a 1 mm edge length would contain $O(10^{20})$ atoms.

When a shock wave interacts with a PBX material, complex wave interactions result due to scattering of the shock at interfaces. This complexity is compounded by the intrinsic mechanical and failure response of the PBX constituents and the interfaces among them. Collectively, these processes lead to highly heterogeneous distributions of local temperature, stress, strain, and strain rate within the PBX structure. Spatially localized regions of high pressure and temperature, corresponding to the tails of the distributions, are known as *hotspots*. For those hotspots with sufficiently high temperature and pressure, the endothermic primary reactions will be followed quickly by fast, strongly exothermic ones and local ignition will occur. Beyond some critical surface in the hotspot size and temperature space,[117–120] the rate of energy release due to chemistry will overcome thermal dissipation, leading to sustained reactions that yield small-molecule products. This causes emission of stress and thermal pulses into the surrounding material, enhancing the spread of chemistry. If the spatial density of such violent hotspot ignition sites is sufficiently high, they will interact constructively with the shock wave and detonation initiation will commence.

The emergence of a detonation front in a PBX involves a complicated multi-physics, multiscale interplay among physical and chemical processes at spatial scales ranging from Ångstroms to $O(100\ \mu\text{m})$ with associated time scales extending from femtoseconds to microseconds. A robust and reliable capability for predicting deto-

nation initiation must therefore first identify and then characterize and incorporate both the salient underlying physics and chemistry as well as the grain-scale composition and morphology of the material. That is, predictive models for the response of PBX materials to shocks are intrinsically multiscale and must be both meso-informed and microstructurally aware.

Multiscale models usually fall into two broad categories: sequential and concurrent. In sequential approaches, which are relatively common and practically feasible to employ, information obtained using simulations at shorter length/time scales are used to guide the formulation and/or parameterization of physics or chemistry submodels required at larger scales. For example, important physical properties—such as the elastic tensor, specific heat, melting curve, transport coefficients, and chemical reaction rates—can be calculated as functions of temperature and pressure using molecular dynamics or electronic structure ("quantum chemistry") calculations and used directly to parameterize mesoscale continuum models. Wherever possible, fundamental information from experiment is also used. For energetic materials, this sequential approach is most commonly used for multiscale model development.[121–132]

In concurrent approaches, multiple methods are applied simultaneously, in real time and on-the-fly, to 'seamlessly' integrate information from a smaller-spatial-scale, more fundamental method into a larger/more engineering-oriented simulation. An obvious target for such approaches is to use fundamental methods to simulate the physics and chemistry in regions of a sample where the state of the system is evolving quickly and with a high degree of spatial localization, essentially discontinuously on the scale of a continuum simulation. During detonation initiation, such regions would likely be closely associated with interfaces, whether between materials or at pore surfaces. Clearly, such approaches face severe challenges, due to the numerical stiffness of the equations that must be solved: The time step in an all-atom MD simulation that

fully resolves the atomic motions, as would be required for simulations of chemistry, is set by the vibrational period of the highest frequency oscillators in the system (*i.e.*, X-H covalent bonds, where X = C, N, O) and is approximately 10^{-16} s. By contrast, the time step in a continuum simulation is set by the Courant-Friedrichs-Lewy (CFL) condition for transmission of a wave across a cell in the computational domain and, even in the case of a highly resolved simulation with a cell edge length on the order of a nanometer, is approximately 10^{-12} s. In practical engineering simulations, with a cell edge length of $\simeq$100 nm, the time step is correspondingly larger, exacerbating the difficulty of the approach. Although applications of concurrent methods would seem to be within reach as a means of elucidating the physics, we are unaware of applications of truly concurrent approaches to energetic materials that can predict macroscale responses in a multiscale framework. Moreover, given the large volume fraction corresponding to material interfaces in a PBX, and the fact that the regions of interest would shift substantially in the sample during the overall physical and chemical disintegration of the microstructure that accompanies initiation, system-scale application of concurrent methods to energetic materials is not practical at the present time.

Multiscale approaches that fall between fully sequential and fully concurrent exist and appear to be promising if formulated within an agile computational framework. An example of this is the Local Interpretable Model-agnostic Explanations (LIME) approach due to Barnes *et al.*[133–135] Those authors combined dissipative particle dynamics (DPD) with a Lagrangian continuum approach to simulate a Taylor impact of a sample of RDX onto a stationary platen.[136–138] The DPD model is a coarse-grain particle method that Barnes *et al.* calibrated separately against atomistic simulations. Starting from an EOS model that was known over limited intervals of thermodynamic space, the DPD model was used to calculate new EOS points, on the fly, whenever

the continuum simulation accessed regions of state space for which information was unavailable. The new information was then added to the EOS table.[136–138] Thus, as the overall simulation progressed, the amount of computational work associated with DPD sub-cycling decreased.

Independent of which type of multiscale method is employed, predictive models for PBXs must include descriptions at the nano, micro, and macro scales that accurately represent the critical physics at each scale, with appropriate filtering that passes successively less detailed information between successively larger scales. Calculations at each scale with the desired levels of accuracy and precision are computationally intense. For example, for a truly descriptive MD calculation of energetic crystals, current state-of-the-art computer hardware restricts the model size and times to the submicron and nanosecond regime. It is not, at this time, possible to fully resolve the molecular dynamics of crystals that are commonly seen in PBXs, that is, in the micron size range. Furthermore, fully three-dimensional (3D) simulations of crystals containing small but realistic defects are only on the verge of being feasible; accordingly, most MD studies are restricted to very small 3D samples or quasi-2D calculations in which the sample is 'large' in two dimensions but quite small in the third. On the other hand, at the mesoscale where hotspot initiation and growth must be modeled, continuum studies have shown[139] that pores must be resolved using several hundred grid points across the diameter to obtain reliable hotspot characteristics. While doable,[140,141] 3D continuum calculations are sufficiently expensive that production runs to characterize behavior across a range of loading regimes, pore sizes, and material morphologies will remain out of reach for the next few years. Furthermore, accurate simulations of fields of pores, anisotropic materials, description of rate-dependent material response, damage, fracture, and other complex physics that are inherent in PBXs under shock loading have been explored by various researchers

but are limited in terms of regime and model fidelity.[142–148] Thus, accurate MD and continuum calculations of hotspot formation are still active areas of research. They are not yet run-of-the-mill simulations that can be performed routinely as part of a multiscale calculation. The models are too uncertain, and both fundamental physics and practical computational challenges remain.

The clearest case where the state-of-the-art has begun to solidify in the past decade is the treatment of the collapse of a single pore or small array of pores in an energetic solid. Well-resolved simulations of the dynamics of such systems have been performed by several groups.[119,139,141,149–151] Even for this limited case, however, benchmarking calculations—even for the relatively benign case of an inert treatment of the energetic material—is not straightforward. Experiments on isolated pore collapse have yet provided data on important quantitative measures, such as the very important (from a hotspot-model perspective) post-collapse temperature. An alternative approach to establishing the correctness of limitations of continuum models of pore-collapse induced hotspot formation is to perform MD simulations and to treat the latter as "ground truth". Some previous work has attempted such continuum-MD comparisons. The study most similar in spirit to the present one is due to Wood *et al.*,[128] who presented side-by-side reactive MD and Eulerian (CTH) simulations of shock-induced pore collapse and chemistry in hexanitrostilbene (HNS). Their calculations for HNS showed significant differences in the calculated pore shapes during collapse as well as the hotspot temperatures.

Using MD as "ground truth" to benchmark mesoscale calculations of pore collapse is not without its pitfalls. Whereas MD simulations must rely on the best available interatomic potentials, continuum mesoscale pore-collapse simulations must rely on best available material models and parameterizations that can be found in the literature. For a head-to-head comparison between MD and mesoscale simulations, the

physical domain size studied must be the same (*e.g.*, pore diameters of tens of nm) and the boundary conditions must be treated in a functionally equivalent fashion. Anisotropy emerges naturally in MD calculations as a consequence of the molecular structure and interatomic forces but must be explicitly modeled in the continuum simulations; such anisotropic continuum models are just now emerging and are expensive to perform relative to isotropic cases. For large, continuum-compatible pore sizes—that is, tens of nanometers in diameter—3D simulations in MD are computationally too burdensome to be routine. Also, critically, it must be understood that MD simulations, even so-called 'quantum MD' simulations wherein the forces are obtained directly from an electronic-structure calculation rather than from a calibrated empirical-form force field, are inherently classical in nature. Tunneling, delocalization of light atoms, zero-point energy, and other quantum effects are absent. Of particular relevance to shock wave simulations, the specific heat in a MD shock simulation is constant (essentially the classical law of Dulong and Petit) whereas in reality (*i.e.*, quantum mechanically) it is a strong function of temperature for molecular materials over the range of temperatures relevant to detonation initiation—zero at 0 K and only approaching the classical limit for temperatures in excess of roughly 1000 K. A consequence is that MD predictions of shock temperature will be lower than it would be obtained in an 'equivalent' quantum-mechanical simulation or in reality. Because chemical reaction rates increase approximately exponentially with temperature, this discrepancy between classical and quantum pictures needs to be interpreted carefully. (Here we partially address it by using a MD force field for which chemistry does not occur and by not including chemistry in the continuum description. That is, we focus solely on the thermo-mechanical response.)

For the reasons just discussed, head-to-head comparisons between MD and continuum mechanics still have to compromise on the fidelity of the material description,

2D or quasi-2D system size and shape, isotropic assumptions, and so on. A true head-to-head comparison remains elusive yet highly desirable. The present study describes a step in that direction. The material chosen for study is 1,3,5-triamino-2,4,6-trinitrobenzene (TATB), which is among the more challenging molecules in the context of a direct MD-continuum comparison, for reasons we now explain.

TATB is a remarkably insensitive secondary high explosive.[152,153] The TATB molecule consists of a central benzene ring bonded with alternating amino (-NH_2) and nitro (-NO_2) groups. Despite the steric crowding of the pendent -NH_2 and -NO_2 groups, the molecule is planar due to the combined effects of push-pull electronic interactions and intramolecular hydrogen bonding between amino and nitro groups on adjacent carbon atoms.[154] In the crystal, individual TATB molecules pack into planar sheets, with a hexagonal-like arrangement of molecules and extensive intermolecular hydrogen bonding. These sheets stack into weakly interacting 'graphitic-like' layers that interact mainly through van der Waals forces. The crystal is triclinic with two molecules per unit cell. The structure of the crystal is strongly anisotropic and this is reflected in pronounced anisotropy for many of the thermal,[36,37,39–41,43,44,155–159] mechanical,[38,42,86,91,106,160–164] and optical properties.[85]

TATB is particularly useful for mesoscale model development. From the MD perspective, it is among the most anisotropic organic molecular crystal structures known; and because the crystal is triclinic—the most general crystal symmetry class—methods suitable for the simulations and analysis of TATB should be capable of treating other energetic molecular crystals such as HMX, RDX, and PETN as successively simpler (*i.e.*, higher symmetry) special cases. From the mesoscale perspective, what is known about the elastic and plastic behavior of the crystal strongly suggests that accurate simulations of the single-crystal response to dynamic loading will require the use of thermo-mechanically complete and detailed descriptions of the equation of

state (EOS) and constitutive behavior, including crystal plasticity. Therefore, TATB provides a good testbed for assessing the ability of standard continuum treatments of pore collapse to capture the full range of phenomena that are observed in 'ground truth' MD studies.

Here, we report comparisons between MD and continuum predictions of shock-induced pore collapse in crystalline TATB. The simulations were performed independently but using (almost exactly) same system size, geometry, and impact conditions. We discuss the differences between the MD and continuum results with the goal of identifying particular aspects of the continuum models most urgently require improvements to bring the continuum predictions into closer agreement with the MD. All continuum calculations were performed by Prof. Udaykumar's group at University of Iowa.

The MD and continuum methods and models used are described in Sec. 2.3. Results are presented in Sec. 2.4; namely, head-to-head MD/continuum comparisons in Sec. 2.4.1, an MD study of the effects of crystal orientation in Sec. 2.4.2, and a study of the sensitivity of the continuum predictions to the models used to treat the specific heat and the melt curve in Sec. 2.4.3. Additional discussion and suggestions for future work are provided in Sec. 2.5. Concluding comments are given in Sec. 2.6.

2.3 Methods

The computational setup, shown in Figure 2.1, is a 150 nm $\times$ 150 nm 2D or quasi-2D domain containing a 50 nm diameter pore at the center. The pore and domain sizes are sufficiently small to make MD calculations feasible while also ensuring that the continuum description still holds. The impact speeds studied are 0.5 km s^{-1}, 1.0 km s^{-1}, and 2.0 km s^{-1}. These span relatively weak loads for which material

strength is likely to play a role to strong loads for which inertia overwhelms strength. Below, MD and continuum simulations will be compared for calculated evolution of pore shapes, pressure, stress, and temperature fields over this range of flow conditions.

For a head-to-head comparison, postprocessing of the MD and continuum results is necessary to juxtapose them meaningfully and on an equal footing. To accomplish this, MD information residing on the particles (atoms) will be converted to field-based quantities with (essentially) the same spatial resolution as in the continuum simulations. The MD simulations are performed for three different crystal orientations. The isotropic continuum model is constructed using material descriptions that are based on MD calculations for TATB[40,44] and the resulting pore-collapse predictions will be evaluated against the MD results. Multiple models for the melting temperature and specific heat are investigated using the continuum simulations due to expected sensitivity of the predictions to them and/or large uncertainties among published fundamental data.

The specifics of the MD and continuum methods are described in Secs. 2.3.1 and 2.3.2, respectively.

2.3.1 Molecular dynamics models

2.3.1.1 Force-field model

The all-atom, nonreactive, fully flexible force field originally due to Bedrov *et al.*[86] and later refined by Kroonblawd and Sewell[36] and Mathew *et al.*[39] was used for the MD simulations. In the Bedrov *et al.* force field, terms for covalent bonds, three-center bends, and improper dihedrals are modeled using harmonic functions and dihedral interactions are approximated using truncated cosine series. Here, all N-H covalent bonds were constrained to the equilibrium distance using the RATTLE algorithm.[165]

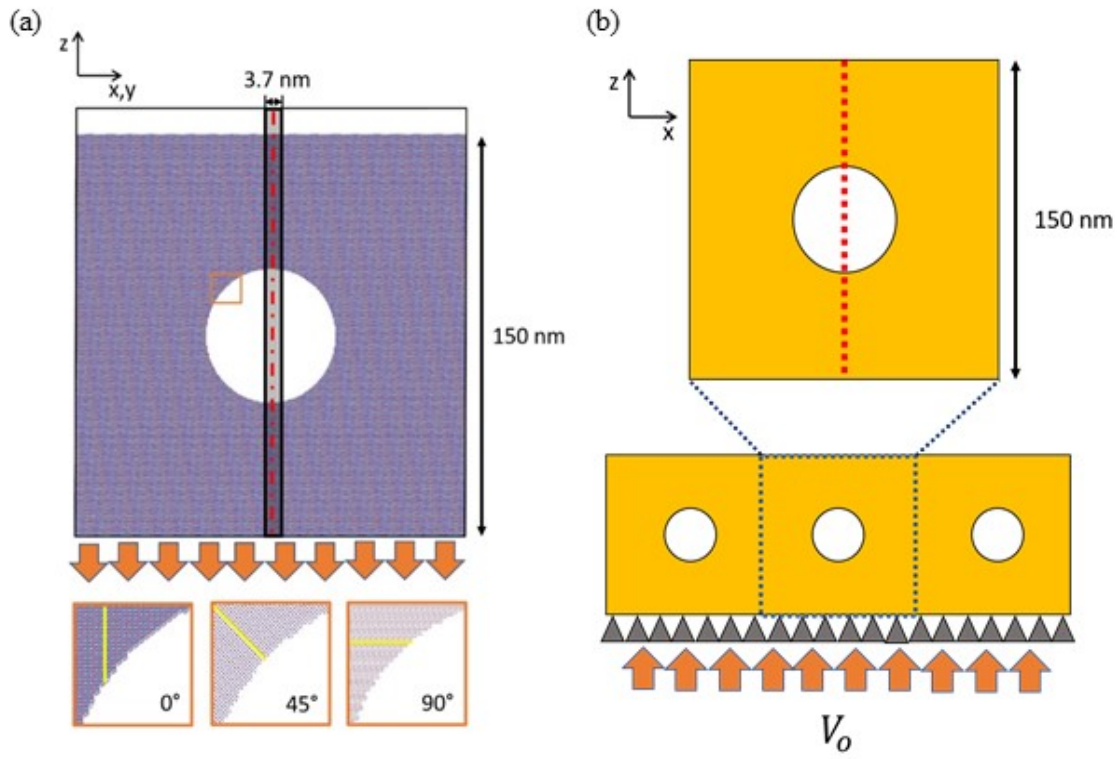

Figure 2.1: Geometric setups for the MD and continuum simulations. For the MD simulations (panel (a)), a reverse-ballistic configuration was used in which the sample impacts a rigid, stationary piston at the bottom of the sample. Periodic boundary conditions (PBCs) are applied in all directions. The thin vertical strip spanning the pore denotes the region of material studied using time-position (t-z) diagrams (discussed in Figure 2.3) and temperature time histories at particular locations along the pore centerline (discussed in Figure 2.12). The outsets at the bottom are zoom-in views that depict the three crystal orientations studied using MD. For the continuum simulations (panel (b)), a constant-velocity piston impacts the sample from below. (The MD and continuum results are relatable by a simple Galilean transformation.) The continuum domain consists of a horizontal array of three identical sub-samples, each the same size as the MD domain, designed to minimize reflection effects from the domain boundary and better emulate the effects of the PBCs used in the MD. The vertically arranged red dots denote a set of Lagrangian tracer particles embedded in the sample for the purpose of generating the t-z diagrams and temperature time histories mentioned above.

Non-bonded interactions between atoms belonging to different molecules are modeled using the Buckingham-plus-Coulomb form (exp-6-1). Non-bonded interactions between atoms within a given molecule are neglected, with the exception of a short-range repulsion introduced by Mathew *et al.* that acts between O and H atoms on adjacent pendent groups. The very-short-range non-bonded repulsion described by Bedrov *et al.* was used to prevent 'overtopping' of the exp-6-1 potential at very short distances. (The exp-6-1 potential exhibits a maximum for distances of approximately 1 Å then diverges to negative infinity, with concomitant divergence of the forces, for shorter distances. This non-physical artifact of the functional form is remedied by inclusion of the very-short-range repulsion.) Non-bonded interactions were computed in real space up to an 11 Å cutoff using the Wolf summation method.[166] Three-dimensional periodic boundary conditions (PBCs) were applied. The method by which the short-range non-bonded repulsion was implemented in LAMMPS, including an input deck, is described in Appendix I and II. Comparisons of atomic forces calculated using the PPPM and Wolf method are dicussed in Appendix III.

2.3.1.2 Simulation cell setup and equilibration

Simulation cells for three crystal orientations, spanning the limiting cases that correspond to shocks propagating exactly perpendicular ($\theta \equiv 0$) and exactly parallel ($\theta \equiv 90°$) to the surface-normal vector of the layers in the TATB crystal structure, were constructed using the Generalized Crystal-Cutting Method (GCCM) developed by Kroonblawd *et al.*[70] The intermediate orientation corresponds to shock orientation $\theta = 45°$. The angle θ is defined as that between crystallographic lattice vector $\mathbf{a}$ (which lies within the crystal layers) and the shock direction $\mathbf{S}$. The shock direction was constrained to lie within the plane defined by lattice vector $\mathbf{a}$ and the basal-plane normal vector $\mathbf{N}_{(001)} = \mathbf{a} \times \mathbf{b}$. *Generalized unit cells* for the three cases

were constructed under the constraint that they be approximately orthorhombic and have a simulation-cell-face normal vector parallel to **S**. These generalized unit cells, which were constructed based on the (300 K, 1 atm) unit cell lattice parameters for the crystal as predicted by the force field, were replicated in 3D space to yield primary simulations cells (*samples*) with edge lengths of approximately 150 nm along two directions and ≈3.5 nm in the third (thin) direction; that is, quasi-2D primary simulation domains.

Figure 2.1(a) depicts the overall MD simulation setup. It also contains zoom-in views of the three crystal orientations, including a segment of the pore surface in each case. A cylindrical pore with initial diameter 50 nm is located at the center of the sample with the cylinder axis of the pore parallel to the thin direction of the primary simulation cell. The samples contained 303,024, 272,594, and 328,076 molecules for $\theta = 0$, 45°, and 90°, respectively. The samples were rotated such that **S** is always parallel to $+z$ in the Cartesian lab frame. In this arrangement shocks propagate vertically upward. A 10.0 nm vacuum region was introduced along z at the "tops" of the samples to eliminate electrostatic interactions across the periodic boundaries.

All MD simulations were performed using the LAMMPS code.[77,78] System geometries were first energy minimized using the FIRE method[167] with a 0.25 fs timestep. The minimization was performed with 0.0 tolerance for both energy and force, and 200 and 2000 as the maximum numbers of iterations and evaluations. Isochoric-isothermal (NVT) and isochoric-isoenergetic (NVE) trajectories were calculated using the velocity Verlet integrator[74] with 0.25 fs and 0.20 fs time steps, respectively. Starting from the three GCCM-generated samples, each system was equilibrated to $T = 300$ K using a two-stage process. First, a 1.3 ps NVE simulation was performed during which temperature was computed every 10 fs and the atomic velocities re-scaled to 300 K if $|T(t) - 300\ K| > 10\ K$, with selection of completely new atomic velocities from

the Maxwell distribution every 100 fs. This was followed by 5 ps of NVT integration using the Nosé-Hoover thermostat[168,169] with the thermostat coupling parameter set to 100 fs.

2.3.1.3 MD shock simulations

Shocks were generated using a reverse-ballistic configuration[80] in which a fully flexible TATB sample impacts a rigid, infinitely massive piston of the same material. Specifically, starting from the final phase space point from the end of the NVT equilibration, all molecules with center-of-mass positions within 20 Å of the "bottom" of a given sample ($z = 0$) were assigned to the piston. Their velocities were set to, and maintained at, zero for the rest of the simulation. The velocity vectors $\mathbf{u}_\mathrm{p}$ = (0, 0, -0.5 km s^{-1}), (0, 0, -1.0 km s^{-1}), or (0, 0, -2.0 km s^{-1}) were added to the instantaneous thermal velocities of atoms in the flexible region for a given sample, thus completing the specification of initial conditions for the NVE production simulations. The approach just described results in a supported shock wave traveling with velocity $\mathbf{u}_\mathrm{w}$ parallel to the z-axis in the lab frame. Because of the inflow of material into the shock front in the reverse-ballistic configuration, the shock velocity is $\mathbf{u}_\mathrm{s} = \mathbf{u}_\mathrm{w} + |\mathbf{u}_\mathrm{p}|$. The simulation for a given crystal orientation and impact speed was continued at least until the lead shock wave reached the free surface at the top of the sample (25 ps – 50 ps, depending on the orientation and impact strength). The atomic Cartesian positions, velocities, and stress tensor components were recorded every 100 fs during the NVE production simulations.

2.3.1.4 Trajectory analysis

Two-dimensional maps of system properties were calculated by subdividing the simulation domain into a set of contiguous bins. The bins, which are stationary in the lab frame and are Eulerian in the sense that material flows through them as simulation proceeds, are approximately square (edge length ≈1.25 nm) in the large directions of the simulation cell and extend all the way through the depth of the material in the thin direction (≈3.5 nm). A molecular basis was used throughout wherein entire molecules were assigned to a bin based on their center-of-mass positions, with all atoms belonging to a given molecule assigned to that same bin.

In addition to calculating 2D property maps across the entire domain at selected instants of time, time-position (t-z) diagrams were calculated for a thin strip of material oriented parallel to the shock direction and centered on the vertical centerline (diameter) of the initial pore; see Figure 2.1(a). The t-z diagrams depict the time evolution of material in the strip as a function of location along the length of the strip. Properties studied using the t-z diagrams include the kinetic temperature T (*i.e.*, local kinetic energy density expressed in temperature units) and the pressure tensor component P_{zz} parallel to the shock direction.

The area (more precisely, volume in quasi-2D) of the pore, A_{pore}, was calculated as a function of time during collapse as the product of the number of empty Eulerian bins in the vicinity of the pore and the area (volume) of an individual bin. For simplicity, the occupancy of a given bin is defined in binary fashion; it is unity if one or more molecules is present and zero otherwise. The results for this quantity were presented in dimensionless units $A_{pore}(t/t^*)/A_0$ vs. t/t^*, where A_0 is the initial pore area, t is physical time, and $t^* = D/\mathbf{u}_\mathrm{s}$, where $D = 50$ nm and $\mathbf{u}_\mathrm{s}$ is the bulk shock speed for a given crystal orientation and impact strength. (Table 2.1 lists the calculated shock speeds for each impact velocity for both the MD and continuum models; the velocities

Shock load	MD (0°)	MD (45°)	MD (90°)	Continuum
2.0 km s^{-1}	6.2316 km s^{-1}	6.3225 km s^{-1}	7.0215 km s^{-1}	6.6589 km s^{-1}
1.0 km s^{-1}	6.0617 km s^{-1}	4.8178 km s^{-1}	5.4656 km s^{-1}	4.9769 km s^{-1}
0.5 km s^{-1}	6.1367 km s^{-1}	4.3917 km s^{-1}	4.3694 km s^{-1}	4.0727 km s^{-1}

Table 2.1: Shock speeds from the MD and continuum simulations.

in the MD model depend on the crystal orientation.) The physical significance of t^* is that it defines the time required for a shock in bulk crystal to traverse a length of material equal to the initial pore diameter. As such, it calibrates an internal clock against which the speed of collapse can be sensibly regarded as relatively fast or slow. In the case of a strong shock for which pore collapse is dominated by hydrodynamic-like flow, the scaled time required for pore collapse will be close to unity; whereas, for weaker shocks for which visco-plastic effects are dominant, the scaled time required for collapse will be greater than unity and will increase as the shock strength is decreased. The shock speed required was determined independently for each crystal orientation and impact speed, for material located between the piston and pore but 'far' away from both, using methods that have been described elsewhere.[47,80,112]

Specific equations used to compute the various other properties used for the MD analysis are described elsewhere.[47,50,56,112]

2.3.2 Continuum models

High-resolution continuum calculations of pore collapse were performed for a computational setup almost identical to the MD using the SCIMITAR3D code.[170–172] The continuum model is described below.

2.3.2.1 Governing equations and constitutive relations

The set of hyperbolic conservation laws including the conservation of mass, momentum, and energy are solved:[171]

$$\frac{\partial \rho}{\partial \mathrm{t}} + \mathrm{div}(\rho \tilde{\mathrm{u}}) = 0 \tag{2.1}$$

$$\frac{\partial \rho \vec{\mathrm{u}}}{\partial \mathrm{t}} + \mathrm{div}\left(\rho \vec{\mathrm{u}} \otimes \vec{\mathrm{u}} - \sigma\right) = 0 \tag{2.2}$$

$$\frac{\partial \rho \mathrm{e}}{\partial \mathrm{t}} + \mathrm{div}\left(\rho \mathrm{e} \vec{\mathrm{u}} - \sigma \vec{\mathrm{u}}\right) = 0, \tag{2.3}$$

where ρ is density, u is particle velocity, and e is internal energy.

The stress tensor is composed of deviatoric term S and hydrostatic pressure P,

$$\sigma = \mathrm{S} - \mathrm{PI}, \tag{2.4}$$

where I denotes the identity matrix. The deviatoric term is evolved using a Prandtl-Reuss formulation:

$$\frac{\partial \rho \mathrm{S}}{\partial \mathrm{t}} + \mathrm{div}\left(\rho \vec{\mathrm{u}} \mathrm{S}\right) + \frac{2}{3}\rho \mathrm{G}\,\mathrm{tr}(\mathrm{D})\mathrm{I} - 2\rho \mathrm{G}\mathrm{D} = 0, \tag{2.5}$$

where D and G denote strain rate and shear modulus, respectively. As described in previous work,[171] the evolution of the deviatoric stress first assumes a pure elastic deformation (*i.e.*, freezing the plastic flow) as a predictor step followed by a correction step to remap the predicted stress onto a yield surface by a radial return algorithm.[173] The Johnson-Cook flow rule is employed, but perfect plasticity is currently assumed. The yield surface is defined as

$$\mathrm{f} = \mathrm{S_e} - \sigma_\mathrm{Y} \tag{2.6}$$

and

$$\mathrm{S_e} = \sqrt{\frac{3}{2}\mathrm{S} \cdot \mathrm{S}}, \tag{2.7}$$

where the yield strength σ_Y is set to a constant[174] for TATB. This limits the continuum calculations to an isotropic elastic-perfectly plastic model.

2.3.2.2 Equations of state

To capture the shock-induced high pressure the present work employs the Mie-Grüneisen EOS for TATB:[175]

$$\mathrm{P} = \mathrm{P_C}\left(\mathrm{V}\right) + \frac{\gamma}{\mathrm{V}}\left[\mathrm{e} - \mathrm{e_C}\left(\mathrm{V}\right)\right], \tag{2.8}$$

where γ is the Grüneisen coefficient and V is specific volume. The pressure $\mathrm{P_C}$ on the cold curve is fit to a Birch-Murnaghan EOS[176]

$$\mathrm{P_C(V)} = \frac{3}{2}\mathrm{K_0}\left[\left(\mathrm{V/V_0}\right)^{-7/3} - \left(\mathrm{V/V_0}\right)^{-5/3}\right]\left\{1 + \frac{3}{4}(\mathrm{K_0'} - 4)\left[\left(\mathrm{V/V_0}\right)^{-2/3} - 1\right]\right\}, \tag{2.9}$$

where the coefficients $\mathrm{K_0}$ and $\mathrm{K_0'}$ are the calibrated isothermal bulk modulus and its pressure derivative,[88,117] respectively, and $\mathrm{V_0}$ is a reference volume. The internal energy corresponding to the isothermal state is obtained from

$$\mathrm{e_C}\left(\mathrm{V}\right) = \mathrm{e_o} - \int_{\mathrm{V_0}}^{\mathrm{V}} \mathrm{P_C}\left(\mathrm{V}\right) \mathrm{dV}, \tag{2.10}$$

where e_o is a reference internal energy. The Grüneisen coefficient is defined with respect to density,

$$\gamma\left(V\right) = a + b\left(V/V_o\right), \tag{2.11}$$

and the coefficients a and b are calculated from the calibration factor Z^{177} and zero-pressure Grüneisen parameter γ_o:[174]

$$a = \gamma_o + Z \tag{2.12}$$

$$b = -Z. \tag{2.13}$$

The temperature is obtained from

$$T\left(V, e\right) = T_o\left(V/V_o\right)^{\gamma_o} + \frac{e - e_C\left(V\right)}{C_v}, \tag{2.14}$$

where T_o is the reference temperature (298 K) and C_v is isochoric specific heat. The constitutive properties used are collected in Table 2.2.

Three different models for the melting curve and two for the specific heat were taken or adapted from the literature to enable assessment of the effects of these on the predictions. The melt curve and specific heat models are described in the following subsection.

2.3.2.3 Models for the melt curve and specific heat

Melting was treated using three different models, to reflect the variation of published TATB melting-point data. One model is a pressure-dependent melt curve obtained from recent MD simulations due to Mathew *et al.*,[44] which was obtained using es-

Parameter	Value
Density (ρ_o)	1900 kg m^{-3} ([174])
Yield strength (σ_γ)	0.1 GPa[174]
Shear modulus (G)	7 GPa[174]
Grüneisen parameter (γ_o)	0.8168[177]
K_o	17.1 GPa[88]
K_o'	8.1[88]
A	1.1261
B	0.3093

Table 2.2: Constitutive properties used in the continuum simulations.

sentially the same force field as employed here. In this case, the melt curve is given by

$$\mathrm{T_m(P)} = \left(\frac{\mathrm{P} + 6.4808}{1.6276 \times 10^{-7}} \right)^{1/2.5892}, \tag{2.15}$$

where P is the pressure expressed in kbar. The MD-based melt curve was only calculated up to 2 GPa. Thus, melting temperatures for higher pressures were obtained by extrapolation of the fitting form. The other two models correspond to constant (*i.e.*, pressure-independent), but different, melting points—623 K[174] and 735 K[173]—as determined from independent determinations of the normal melting point. In all cases, the material strength falls to zero for temperatures above the melting point. These three models for melting are shown in Figure 2.2(a).

Two qualitatively different specific-heat models were studied. The first is a temperature-independent, 'classical' specific heat corresponding to that in the MD simulations. In

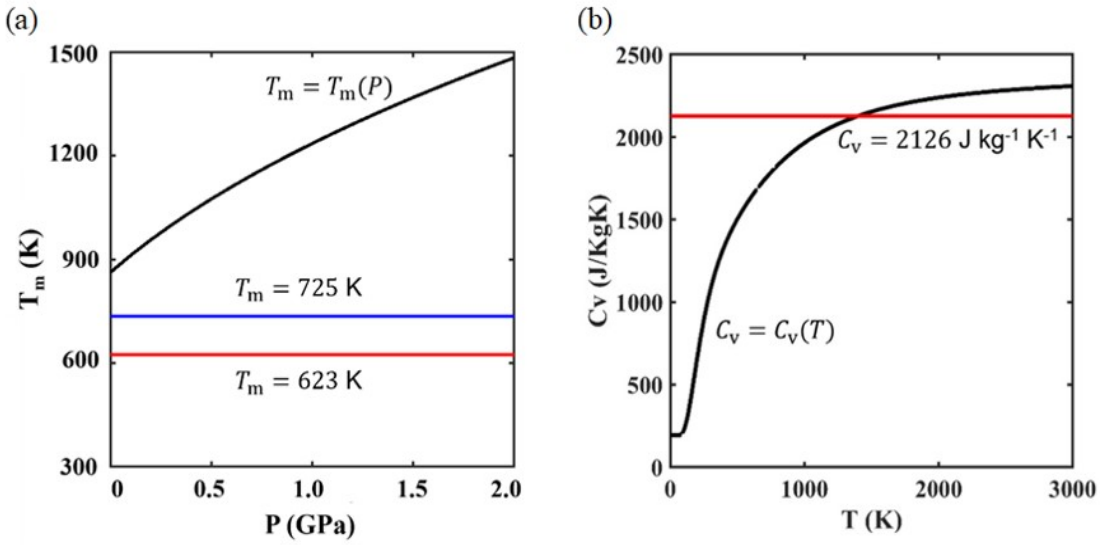

Figure 2.2: Models for melting temperature and specific heat used in the continuum simulations. (a) Melting temperature models. The red and blue lines correspond to TATB normal melting temperatures taken from the literature. The black curve is a pressure-dependent melting curve obtained from MD. In the continuum simulations the material strength goes to zero wherever the temperature exceeds the melting temperature. (b) Specific-heat models used in the continuum simulations. The solid red line is the classical (temperature-independent) specific heat corresponding to, and used for comparisons with, the MD simulations. It takes into account the six constrained N-H covalent bonds per TATB molecule in the MD. The black curve is a more realistic, temperature-dependent model based on quantum mechanical principles. The non-zero specific heat value at $T = 0$ follows from the assumption that molecular center-of-mass translations and librations about lattice sites in the crystal are practically classical at all temperatures. The quantum-based specific heat at high T is larger than the classical value because it takes into account the N-H oscillators, which are constrained in the MD simulations and therefore do not contribute to the classical specific heat.

this model, which is based on the classical equipartition theorem, each *oscillator* in the system contributes k_B to the heat capacity, where k_B is the Boltzmann constant. For a fully flexible molecular crystal composed of molecules containing N atoms apiece, each molecule contributes $3N$ oscillators and thus, because $N = 24$ for TATB, the specific heat per molecule is $72k_B$, which would correspond to the Dulong and Petit classical result. However, *because in the present MD simulations all six N-H covalent bonds per molecule are constrained to constant values*, those bonds do not contribute to the oscillator count, and the heat capacity per molecule is reduced from $72Nk_B$ to $66Nk_B$. The horizontal solid line in Figure 2.2(b) depicts this value, expressed in SI units, which is the one used for the head-to-head MD/continuum comparisons discussed in Sec. 2.4.1.

The second model for the specific heat takes into account the quantum-mechanical temperature dependence of that quantity, which is not captured in standard MD simulations. Based on a quantum chemistry calculation of the vibrational frequencies for an isolated TATB molecule, Kroonblawd *et al.*[40] calculated the temperature dependence of the specific heat per molecule, neglecting the three-apiece local translations and rotations of/about the molecular center-of-mass at a lattice site, and modelled it as a sum to two Einstein oscillators. Under the reasonable assumption that these six 'external oscillators' in the crystal would be classically populated (*i.e.*, in the high-temperature limit of quantum mechanics) even at very low temperatures, the final form used here for the temperature-dependent specific heat of the crystal is:

$$\mathrm{C_v\,(T)} = \mathrm{A_1}\left(\frac{\theta_1}{\mathrm{T}}\right)^2 \frac{\mathrm{e}^{-\frac{\theta_1}{\mathrm{T}}}}{\left(\mathrm{e}^{-\frac{\theta_1}{\mathrm{T}}}-1\right)^2} + \mathrm{A_2}\left(\frac{\theta_2}{\mathrm{T}}\right)^2 \frac{\mathrm{e}^{-\frac{\theta_2}{\mathrm{T}}}}{\left(\mathrm{e}^{-\frac{\theta_2}{\mathrm{T}}}-1\right)^2} + \mathrm{B} \tag{2.16}$$

where $\mathrm{A_1}$, $\mathrm{A_2}$, θ_1, and θ_2 are fitting coefficients due to Kroonblawd *et al.* The quantity $B = 6k_B$ is a constant offset that was added per molecule to account for the external

Parameter	Value
A_1	6.617481×10^{-22} J K^{-1} mol^{-1}
A_2	2.65277×10^{-22} J K^{-1} mol^{-1}
θ_1	803.186 K
θ_2	3088.48 K
B	8.286×10^{-23} J K^{-1} mol^{-1}

Table 2.3: Parameters for the temperature-dependent specific heat model (Eq. 2.16).

molecular degrees of freedom just discussed. The resulting model for the temperature-dependent specific heat is shown as the curve in Figure 2.2(b). Note that the classical and quantum-based results differ asymptotically due to the need to account for the six constrained N-H bonds per molecule in the MD simulations. The values of all parameters in Eq. 2.16 are listed in Table 2.3.

2.3.2.4 Numerical implementation and simulation setup

The continuum simulations were performed using a third-order accurate Essentially Non-Oscillatory (ENO) scheme[178] for the spatial derivatives in the governing equations. Time-stepping was accomplished using a 3$^{\text{rd}}$-order Runge-Kutta time integration. A modified ghost fluid method[178] and narrow-band level set scheme[179] were employed to handle the large deformation of interfaces, including collapse of the pore, in a sharp manner. Further details and validation exercises pertaining to the numerical schemes in SCIMITAR3D are available in the literature.[139,140,170,180]

Figure 2.1(b) shows the overall setup for the continuum simulations. To emulate the periodic boundary conditions used in the MD simulations, the overall compu-

tational domain consists of three contiguous, pore-containing 'unit cells' arranged side-by-side in the domain. Data were collected and displayed for the central pore only. A uniform, square Cartesian grid of edge length 0.1 nm was used, leading to 500 points across the diameter of the undeformed pore. The bottom boundary was fixed so that the shock load P_s emulates planar flyer-plate impact. All other boundaries were open to flow. To extract data at various instants, 61 observation points were located along the vertical centerline of pore as shown in Figure 2.1(b) (red dotted line). Time histories for pressure and temperature were captured in an Eulerian manner, that is, at the fixed probe points shown.

Note that whereas the MD simulations were performed using a reverse-ballistic impact configuration, the continuum simulations were performed using a constant-velocity flyer plate that impacts the initially stationary sample. In presenting the results, therefore, appropriate Galilean transformations were applied to the continuum results where required to enable direct MD/continuum comparisons. All other simulation conditions and corresponding results were designed to minimize, to the extent possible, differences between the MD and continuum simulations and their analyses.

2.4 Results

The results are organized as follows. Section 2.4.1 presents comparisons between MD and continuum predictions for three different shock strengths. The MD results are for crystal orientation of $\theta = 45°$, for which the shock direction $\mathbf{S}$ forms an angle of 45° relative to the surface-normal vector of the molecular layers in the unshocked crystal. The continuum simulations in Sec. 2.4.1 were performed using (1) the constant specific heat shown in Figure 2.2 that corresponds exactly to that in the MD simulation and

(2) the melt curve obtained in a previous MD study by Mathew *et al.*[44]

Section 2.4.2 contains a MD study on the sensitivity of the pore collapse mechanism for the three different crystal orientations. Section 2.4.3 contains a sensitivity study of the continuum predictions with respect to the models used for the specific heat and the melting curve.

2.4.1 Head-to-head comparisons between MD and continuum predictions

Figures 2.3 – 2.7 contain the results of the head-to-head comparisons between the MD and continuum predictions. Figure 2.3 shows, for all three impact speeds, t-z diagrams for the temperature and pressure (longitudinal pressure tensor component P_{zz} in the case of MD) for the thin strip of material along the vertical centerline of the pore as depicted in Figure 2.1. Figures 2.4 – 2.6 contain, for the 2.0 km s^{-1}, 1.0 km s^{-1}, and 0.5 km s^{-1} impacts, respectively, 2D maps of temperature and pressure in the samples at selected instants during pore collapse. Figure 2.7 contains, for all three impact speeds, plots of scaled pore area *vs.* scaled time during collapse; and, for impact speeds of 2.0 km s^{-1} and 1.0 km s^{-1}, temperature distributions after pore closure. In all cases except Figure 2.7(a), for which they appear in the same graph, MD results in Figures 2.3 – 2.7 appear directly above the corresponding continuum predictions. Abscissa and ordinate ranges are the same for a given MD/continuum comparison.

The t-z diagrams for all three impact speeds are discussed in Sec. 2.4.1.1. 2D maps of temperature and pressure are discussed, for successively lower impact speeds, in Secs. 2.4.1.2, 2.4.1.3, and 2.4.1.4. Pore-collapse time histories and temperature distributions after pore closure are discussed in Sec. 2.4.1.5.

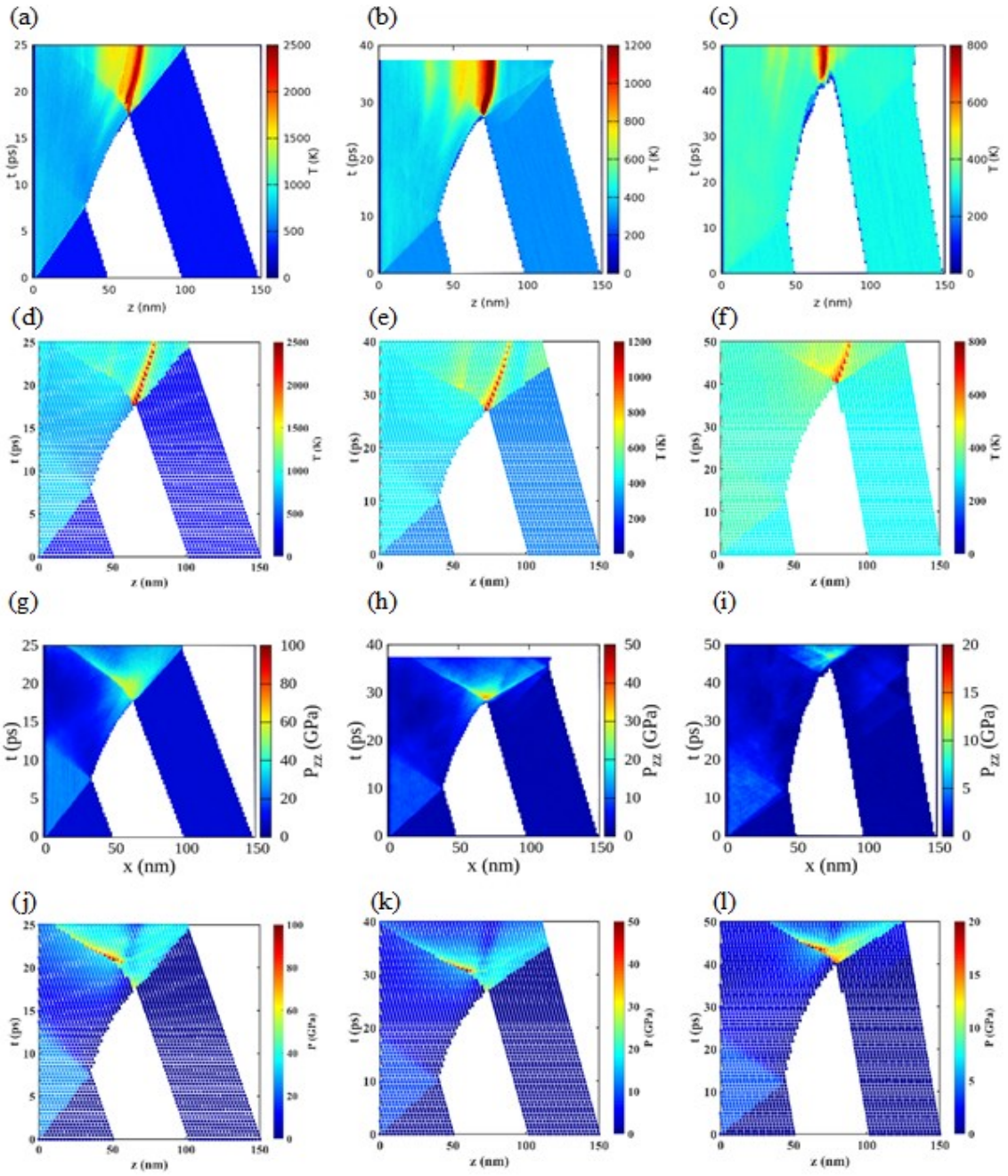

Figure 2.3: Time-position (t-z) diagrams for (a)-(f) temperature and (g)-(l) pressure, calculated for a thin strip of material along the vertical axis of the pore and parallel to the shock direction; see Figure 2.1. Panels (a)-(c) and (g)-(i) are MD results; panels (d)-(f) and (j)-(l) are the corresponding continuum results. From left to right, the columns correspond to impact speeds of 2.0 km s^{-1}, 1.0 km s^{-1}, and 0.5 km s^{-1}. The time axis and color bars differ from one condition to the next but are consistent for a given MD/continuum comparison. The MD simulations shown here and in Figures 2.4 – 2.7 were performed for the case $\theta = 45°$, for which the shock impacts the sample at an angle of 45° relative to the surface-normal vector of the molecular layers in the unshocked crystal.

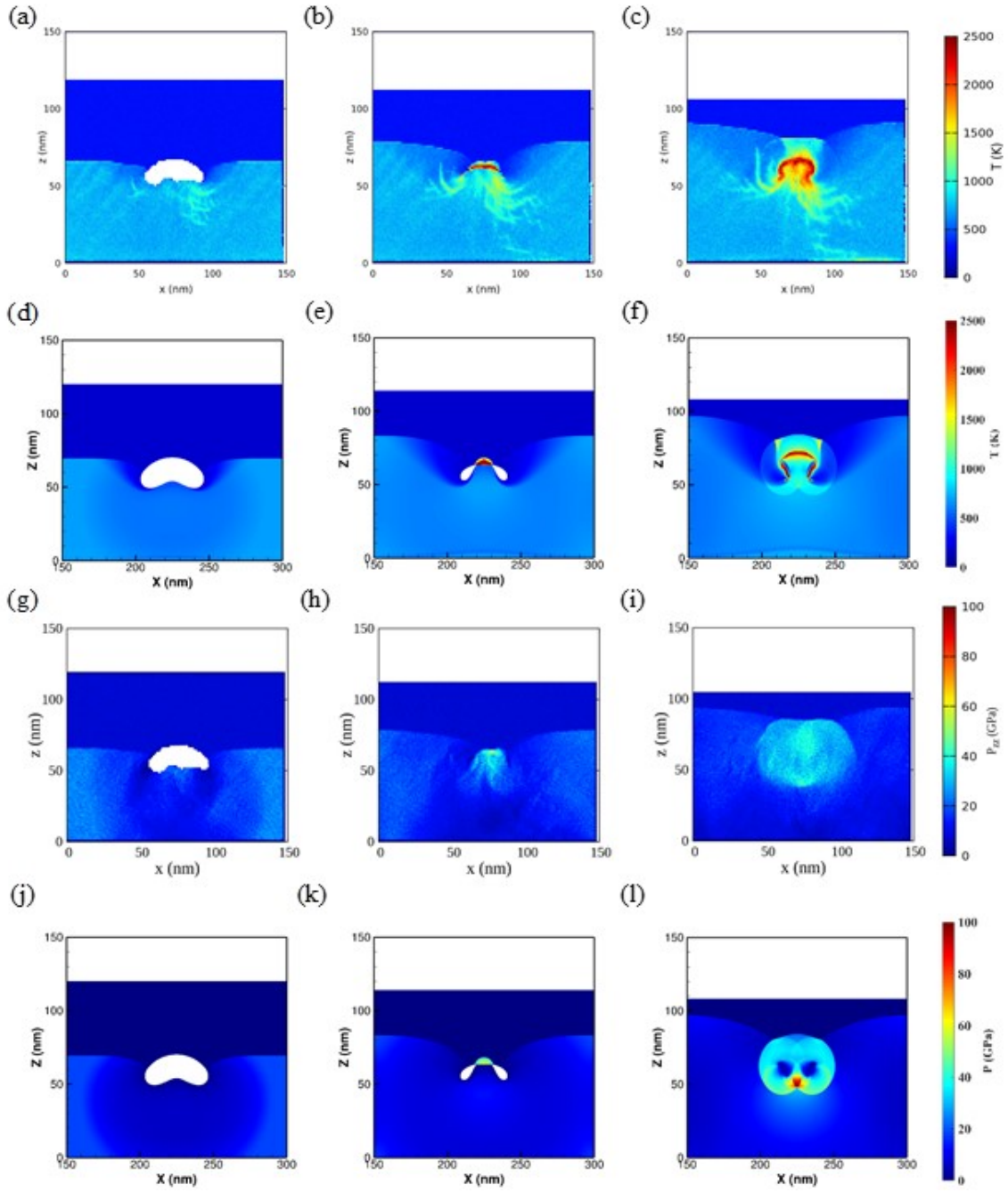

Figure 2.4: 2D spatial maps of (a)-(f) temperature and (g)-(l) pressure at three instants of time for the 2.0 km s^{-1} impact. Panels (a)-(c) and (g)-(i) are MD results, all for the case $\theta = 45°$; panels (d)-(f) and (j)-(l) are the corresponding continuum results. From left to right, the columns correspond to $t = 15.0$ ps, 18.0 ps, and 21.0 ps.

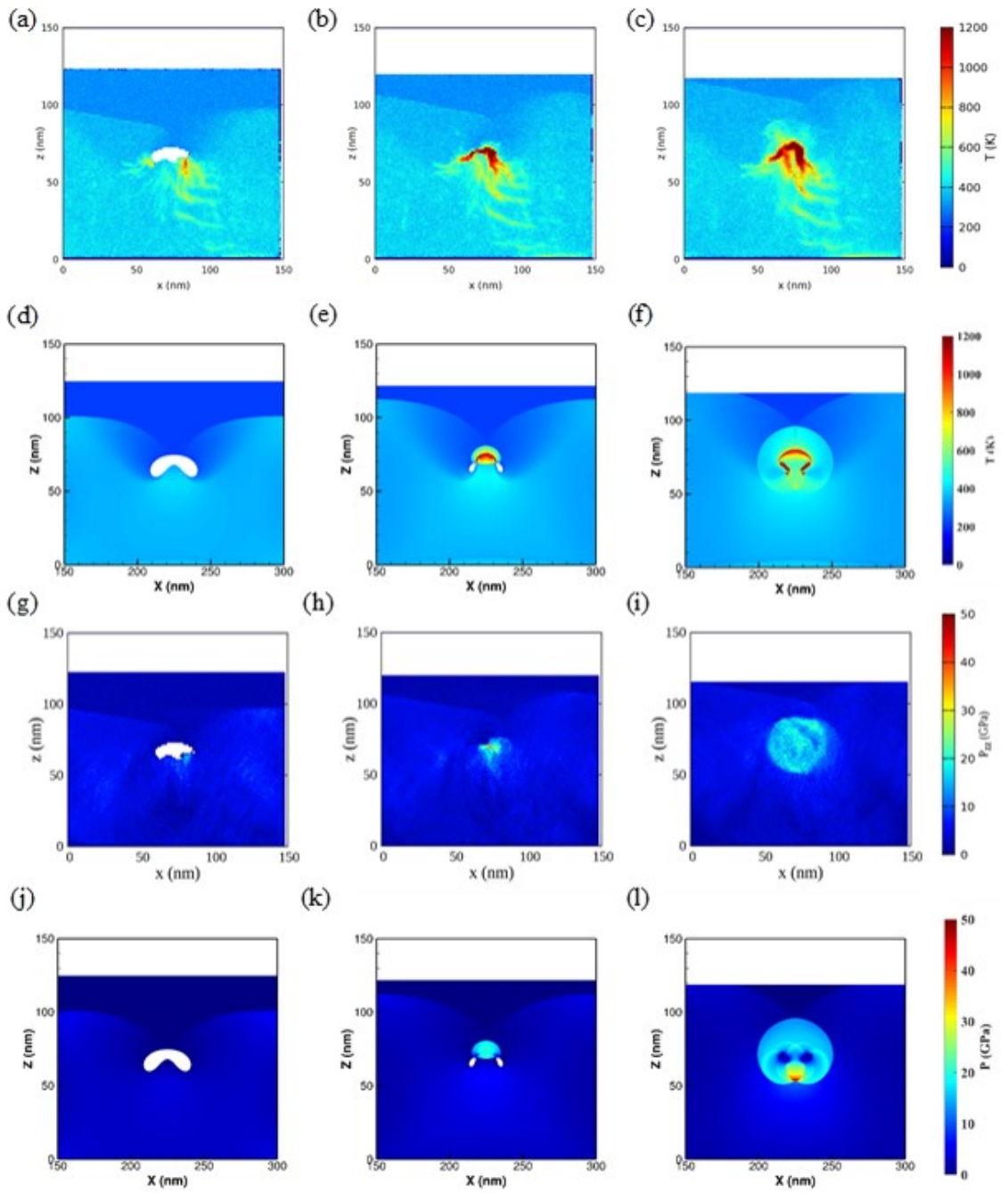

Figure 2.5: As in Figure 2.4 but for the 1.0 km s^{-1} impact. From left to right, the columns correspond to $t = 25.5$ ps, 28.5 ps, and 31.5 ps.

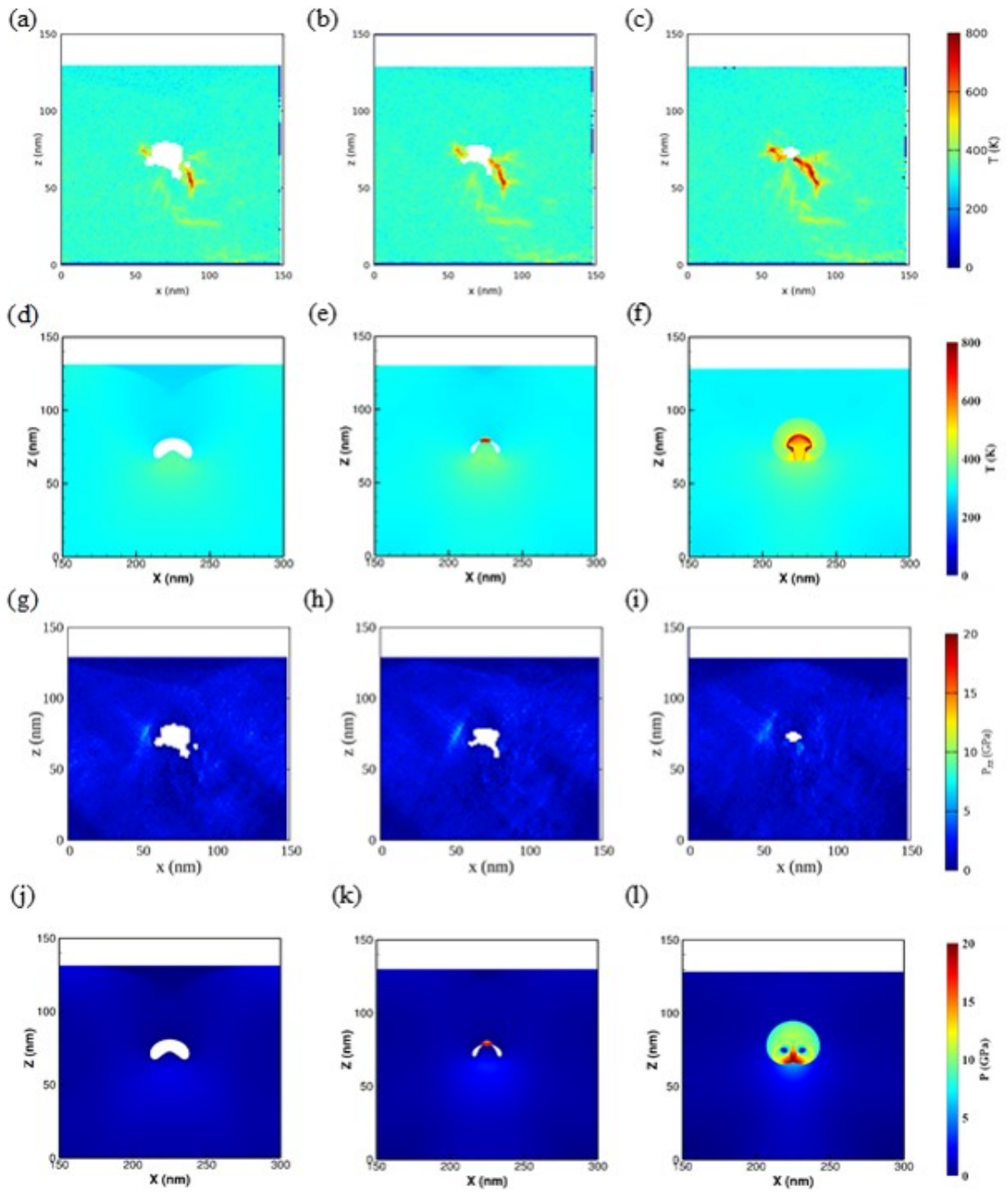

Figure 2.6: As in Figures 2.4 and 2.5 but for the 0.5 km s^{-1} impact. From left to right, the columns correspond to $t = 37.5$ ps, 40.5 ps, and 43.5 ps.

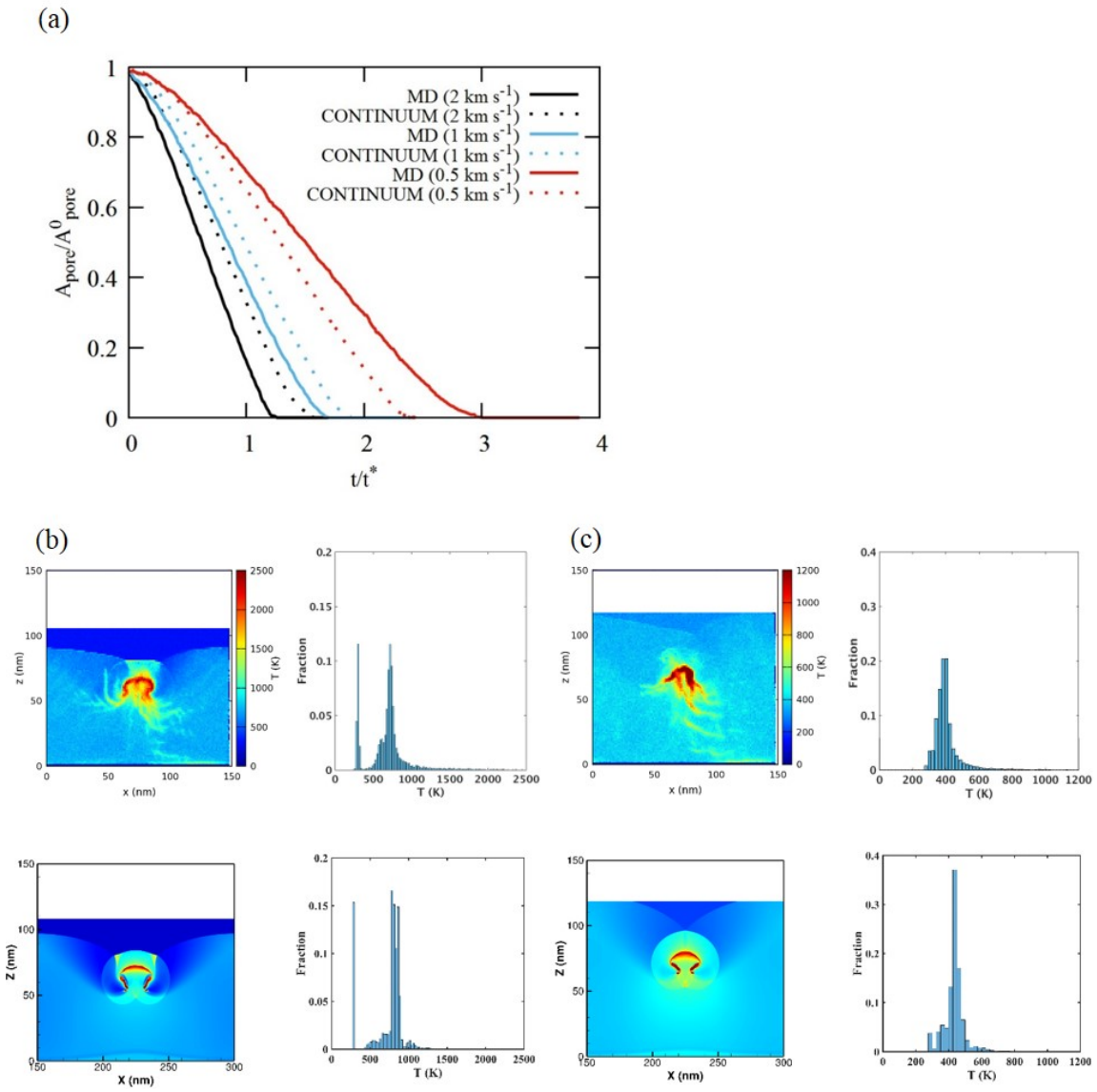

Figure 2.7: (a) Comparisons of scaled pore area $A_{pore}(t)/A_0$ vs. scaled time t/t^* for the MD and continuum simulations, shown parametrically as functions of impact speed. Solid and dotted curves are for MD and continuum mechanics, respectively. Black, blue, and red curves are for impact speeds of 2.0 km s^{-1}, 1.0 km s^{-1}, and 0.5 km s^{-1}, respectively. Panels (b)-(e): 2D snapshots and histogrammatic distributions of temperature at a time close to pore closure. Panels (b)-(c) and (d)-(e) are for MD and continuum mechanics, respectively. The left-hand and right-hand columns are for impact speeds of 2.0 km s^{-1} (at $t = 21.0$ ps) and 1.0 km s^{-1} (at $t = 31.5$ ps), respectively. The abscissa scales are different for the two columns but identical within a column.

2.4.1.1 t-z diagrams

The first, second, and third columns of Figure 2.3 contain t-z diagrams for impact speeds of 2.0 km s^{-1}, 1.0 km s^{-1}, and 0.5 km s^{-1}, respectively. The top two rows contain results for temperature and the bottom two rows for pressure (P_{zz} in the case of MD). In all the diagrams, the pore regions are shown as white.

It can be seen from Figure 2.3 that the continuum and MD predictions of the instants when the shocks reach the upstream pore wall are in close agreement. The shocks strike the upstream pore wall at times between ≈7 ps and ≈12 ps, depending on impact speed. Corresponding times for pore closure are between ≈17 and ≈42 ps. For all three impact speeds, the pore collapse times and pre- and post-collapse characteristics predicted by MD and continuum mechanics along the vertical centerline are in qualitative-to-good agreement.

In the remainder of Sec. 2.4.1 we compare 2D spatial distributions of temperature and pressure in the samples at selected instants of time (Secs. 2.4.1.2 – 2.4.1.4), and the shapes of the pores during collapse (Sec. 2.4.1.5), to obtain a more comprehensive picture of the impact of anisotropy and the concomitant differences between MD and the continuum predictions.

2.4.1.2 2D maps of T and P for 2.0 km s^{-1} impact

Figures 2.4 – 2.6 each depicts, at three evenly spaced instants during and after collapse, the pore contours as well as corresponding 2D maps of temperature and pressure for the MD and continuum calculations. In each figure time increases from left to right in 3 ps increments. The first two rows contain temperature results, with continuum predictions positioned directly below the corresponding MD results. The third and fourth rows are similar but contain results for pressure.

Figure 2.4 contains results for the 2.0 km s^{-1} impact at t = 15 ps, 18 ps, and 21 ps. Figure 2.4(a) shows the shape of the pore during the collapse process in the MD simulation. The pore shape is asymmetric and the pore surface is non-smooth due to the anisotropy of the TATB crystal. In the corresponding isotropic continuum model the pore shape is smooth (Figure 2.4(d)) and distinct jet formation is apparent; the MD calculations do not display a similarly distinct jet. Pore collapse in the MD case (Figure 2.4(b)) leads to an intense hotspot without secondary pores, whereas the continuum pore collapse leads to the formation of sidelobes, with secondary pores that collapse later in time.[139] The post-collapse hotspot from MD (Figure 2.4(c)) remains asymmetric, reflecting crystal anisotropy; the mesoscale hotspot displays the effect of rotational fluid elements seen often in such calculations.[151] The vortical flow 'rolls up' the hotspot in the regions of the sidelobes. While this rollup and concentration of the high temperatures in the vortex cores have been observed in MD calculations as well,[56,60,128] in the present study the strong anisotropy appears to disrupt the formation of concentrated vortical structures. Despite these differences, the overall locations of the incident shock wave, the blast wave emanating from the collapse site, and the location of the Mach stem and triple points all appear to be in fairly good agreement between the MD and continuum predictions. Figure 6.3 of Appendix IV contains an alternative approach to comparing the MD and continuum results, namely, 2D maps of the temperature *difference*, $T_{CONTINUUM} - T_{MD}$, at the instants of pore closure, for both the 2.0 km s^{-1} and 0.5 km s^{-1} impacts. Whereas the MD/continuum comparisons in Figure 2.4 (and analogously in Figures 2.5 – 2.6) are for identical instants in physical time, the results in Figure 6.3 were obtained by calculating the temperature differences in the samples at the respective instants of pore closure in the MD and continuum simulations; thus, a direct comparison between Figures 2.4 – 2.6 and Figure 6.3 is not possible.

The overall agreement in wave propagation characteristics between the MD and continuum predictions is also observed in the pressure contours shown in the bottom two rows of Figure 2.4. The third row contains the MD results and the fourth row the continuum results. The pressure fields have different magnitudes, particularly in the maximum values of pressure at the point of collapse. This is correlated with the formation of a strong jet in the case of the continuum model and the lack of a similarly distinct jet in the MD case. However, the relative distribution of the pressure fields is similar in the two cases. Pore collapse leads to a blast wave centered around the collapse location in MD (Figure 2.4(h)) as well as continuum (Figure 2.4(k)). This blast waves expands outward from the collapse site; the envelope of the blast wave is in general agreement between MD (Figure 2.4(i)) and continuum cases (Figure 2.4(l)).

It is interesting to observe that whereas the 2.0 km s^{-1} case is expected to correspond to hydrodynamic collapse, distinct shear effects are seen in the MD results; these "shear bands" manifest most prominently in the shocked regions in the vicinity of the pore. The shear effect can be visualized by the high-temperature striations and incipient herring-bone patterns in Figures 2.4(a-c). These patterns arise in the regions of intense shear that form as the shock bends around the pore. The high strain rate resulting from the 2.0 km s^{-1} impact leads to strong shear; inspection of analogous figures for the lower velocities, that is, 1.0 km s^{-1} and 0.5 km s^{-1}, exhibit less distinct shear effects. For the 2.0 km s^{-1} impact, the shear-induced deformation of the material in the shocked region leads to a post-collapse hotspot that is surrounded by a region of high temperature. Temperatures in the shear-heated zones are close to 1000 K while the hotspot due to collapse itself is at more than 2500 K (see Figure 2.4(c)). Note by way of contrast that the continuum hotspot (Figure 2.4(f)) is more localized than the MD hotspot (Figure 2.4(c)). The implications of these observations for the growth of the hotspot can be significant and are discussed later

in this chapter.

Pore collapse for the 2.0 km s^{-1} impact leads to local transient temperatures in excess of 2000 K in the vicinity of the pore. Even for TATB, neglect of chemistry under such conditions is a severe approximation that could lead to significant differences between predicted results and reality. This concern may be partially mediated by the very small mass fraction of material that reaches such high temperatures. Reactive MD or continuum simulations that include chemistry could be used to assess this, although the computational expense would be quite high in the case of MD for the system sizes studied here.

2.4.1.3 2D maps of T and P for 1.0 km s^{-1} impact

The head-to-head comparison for the 1.0 km s^{-1} shocks, shown in Figure 2.5, is arranged in the same fashion as for the 2.0 km s^{-1} case (Figure 2.4). At 1.0 km s^{-1} the influence of inertia is still expected to be strong; in the continuum calculations pore collapse again involves formation of a jet (Figure 2.5(d)). The continuum pore profiles and hotspot shape display the distinctly inertial (*i.e.* hydrodynamic jetting) mode of collapse, with the typical mushroom-shaped post-collapse hotspot and sidelobes drawn out by strong vortical flow. Comparing the MD and continuum results, while the magnitude of the temperature in the hotspot as well the concentration of high temperature in a rather localized zone are similar for this 1.0 km s^{-1} case, the pore shapes and resulting hotspot shapes are quite different. These differences were also noted for the 2.0 km s^{-1} case. As was the case for the 2.0 km s^{-1} impact, the spatial distribution of the high- and low-pressure zones around the collapsing pore for the 1.0 km s^{-1} impact are similar for the atomistic and continuum models.

In general, for the two higher velocity cases just discussed the overall extent of the hotspot and the temperature distributions around the hotspot are in fair agreement

between the atomistic and continuum models. The spatial distribution of pressure, in terms of the extent of the blast wave around the point of collapse and the location of the shock/blast wave and the Mach stem are also in good agreement, although the magnitude of pressure exhibits marked differences owing to the reasons discussed above. The weakest impact, that is, 0.5 km s^{-1}, approaches the regime where inertia and deviatoric stresses are both likely to be important.

2.4.1.4 2D maps of T and P for 0.5 km s^{-1} impact

For the 0.5 km s^{-1} impact, the effects of plastic dissipation are expected to influence shock propagation and pore collapse. The t-z plots in Figures 2.3(a-c) and (d-f) reveal significant differences in the hotspot evolution as the impact velocity is decreased from 2.0 km s^{-1} to 0.5 km s^{-1}. Although the times of collapse of the pore are in good agreement, even for the 0.5 km s^{-1} case (cf. Figures 2.3(c) and 2.3(f)), the agreement in velocity of advection of the hotspot becomes poorer with decreasing impact velocity. The effect of the deviatoric stresses for the weak impact is apparent in the contour plots of temperature and pressure shown in Figure 2.6. First, unlike the high-velocity cases, there are significant deviations between MD and continuum models. These are most evident in the pore shapes during the collapse process. The MD pore collapses in a distinctly asymmetric and uneven manner, with a secondary pore formed in the early stages. In addition, the temperature and pressure distributions at each time instant are quite different between the atomistic and continuum situations. Although the temperatures of the hotspot formed are in a similar range, the shapes of the hotspots are clearly different. The continuum (perfectly plastic) model does not capture the strong plastic dissipation effects that arise in the MD calculation. For the continuum calculation, the pore-shape evolution and associated temperature and pressure fields are qualitatively similar to those obtained for the 2.0 km s^{-1} and 1.0 km s^{-1} cases

although the magnitudes are diminished. An interesting observation with regard to the MD results is that whereas a distinct signature of strong shear was seen in the shocked region upstream of the pore for the 2.0 km s^{-1} case, such effects are less apparent for the 0.5 km s^{-1} impact. Plastic dissipation and the lower values of strain rate in this weaker impact likely lead to smaller concentrations of shear.

2.4.1.5 Pore area *vs.* time and temperature distributions during pore closure

In the previous sections, we compared qualitatively the results obtained from MD and continuum simulations for three different impact speeds, highlighting the pore shapes and temperature and pressure fields during collapse. We now compare the hotspots resulting from the collapse events on a quantitative basis, to shed light on the implications of the similarities and differences for predictions of sensitivity of the energetic material. As shown in previous work on multiscale modeling of the response of a porous energetic material,[127,132] the continuum model must yield reliable estimates of the pore-collapse mechanics and the temperature distribution around the collapsed pore, thereby defining the hotspot that sets up the ignition and growth of chemistry. These (mechanical) hotspot data enable the calculation of key hotspot quantities of interest that inform burn models such as the Lee-Tarver ignition-and-growth (IG) model[181] or the Menikoff-Shaw SURF model.[182]

Figure 2.7(a) contains, for both the MD and continuum cases, plots of scaled pore area $A_{pore}(t/t^*)/A_0$ *vs.* scaled time t/t^* (see Sec. 2.3.1.4) for all three impact velocities. For ease of comparison among the various cases, the zero of time in Figure 2.7(a) is taken to be that at which a given shock first reaches the upstream pore wall.

Solid and dotted curves in Figure 2.7(a) correspond to MD and continuum results, respectively. Results for 2.0 km s^{-1}, 1.0 km s^{-1}, and 0.5 km s^{-1} impacts are shown as

black, blue, and red curves, respectively. The continuum predictions exhibit slower closure of the pore (scaled time) relative to MD for all but the lowest impact speed. Agreement between the MD and continuum results is closer for the 2.0 km s^{-1} and 1.0 km s^{-1} cases than for the 0.5 km s^{-1} case. This is not surprising given the distinctly different collapse mechanisms for MD *vs.* continuum mechanics for the weaker impact case; compare Figure 2.6 to Figures 2.4 – 2.5.

The relative delay in the continuum pore closure for the higher velocities may be due to the distinct jet that forms in the continuum simulations but which is not observed in the MD case (see Figures 2.4 and 2.5). The jets are accompanied by sidelobes that form secondary pores, which close later in time. The difference in pore-area time histories between MD and continuum mechanics for the 0.5 km s^{-1} case is most likely due to the plastic dissipation in MD. Indeed, Figure 2.7(a) shows that the continuum prediction for the 0.5 km s^{-1} case is very close to the corresponding MD prediction at early times, whereas at later times the MD collapse slows compared to the continuum result. The continuum pore collapses in standard jet-followed-by-sidelobe collapse mode, while the MD pore collapses *via* an uneven and asymmetrical path.

The shape, size and temperature distribution in the hotspot immediately following pore collapse are all important quantities for predicting hotspot ignition-and-growth phenomena. Figures 2.4 – 2.6 qualitatively compare the hotspot shapes and sizes and Figure 2.7(a) provides quantitative comparisons of scaled pore area *vs.* scaled time. To further quantify the differences in the hotspots, Figures 2.7(b-e) show the temperature contours at the end of the collapse, for both MD and continuum calculations, and corresponding histograms for the mass fractions of TATB that are at different temperatures. The histograms were constructed using bins of 25 K width and captured all the material in the samples.

Several insights regarding hotspot predictions from MD and continuum mechanics can be obtained from the snapshots and temperature histograms shown in Figures 2.7(b-e). First, as noted above, the MD simulation for the 2.0 km s^{-1} impact predicts a strong, concentrated hotspot due to the impact of the lower pore surface onto the upper pore surface (Figures 2.4 and 2.7(b)). Additionally, shear-induced heating (akin to shear band formation in continuum models[143] of pore collapse) also occurs in this case, concentrated in the post-shock, upstream side of the original pore region. This is due to the strong shear stresses induced by the curvature of the shock as it bends around the curved pore surface. The average temperature jump is rather large (>400 K) and the distribution of local temperature in the sample is rather broad (Figure 2.7(b)). The peak of the histogram lies at approximately 700 K, in rough agreement with that of the corresponding continuum case (Figure 2.7(d)). The high-temperature tail of the distribution is critical for hotspot ignition and growth. For the 2.0 km s^{-1} case (Figures 2.7(b) and 2.7(d)), both MD and continuum mechanics predict significant amplitude in the distribution even for temperatures >1000 K. However, the distributions also exhibit significant differences, in alignment with the differences observed from the temperature contours in Figure 2.4. The continuum-based histogram is narrower and is concentrated at the peak values; that is, the continuum hotspot is more localized than the MD-based hotspot. Therefore, for 2.0 km s^{-1} the peaks are in good agreement but the distribution, both on the low temperature side as well as in the high-temperature tail, exhibit sizeable differences. The situation is qualitatively similar for the 1.0 km s^{-1} case, as shown in Figures 2.7(c) and 2.7(e) for MD and continuum mechanics, respectively, although the extent of heating is smaller in this weaker impact case.

2.4.2 Crystal-orientation dependence of shock-induced pore collapse from MD

Figures 2.8 – 2.10 contain MD predictions of pore collapse for all three impact speeds and all three crystal orientations. Although the simulations are quantitative—they yield atomic positions, velocities, forces, and stress tensors as functions of time—the goal in the present study is to draw attention to the qualitative differences in pore collapse depending on shock strength and direction. This focus is reflected in the discussion below.

2.4.2.1 Nature of the flow

Figure 2.8 shows, at particular instants of time for all nine simulations, snapshots of material that was initially (*i.e.*, at $t = 0$) within 25 nm of the pore wall. The times chosen are when $A_{pore}(t)/A_0 = 0.20$, 0.15, and 0.10 for the 2.0 km s^{-1}, 1.0 km s^{-1}, and 0.5 km s^{-1} impacts, respectively. As a guide for the eye, molecules are colored according to initial distance from the center of the pore and whether they were initially above or below the horizontal pore centerline. The initial radial thickness of each semi-annulus is 5 nm.

The first row of Figure 2.8—panels (a)-(c)—is for $\theta = 0$, for which shock propagation is parallel to the molecular layers in the unshocked crystal; the second row, panels (d)-(f), for $\theta = 45°$; and the third row, panels (g)-(i), for $\theta = 90°$, for which the shock direction is perpendicular to the molecular layers. From left to right, the three columns correspond to impact speeds of 2.0 km s^{-1}, 1.0 km s^{-1}, and 0.5 km s^{-1}, respectively.

Animations analogous to Figure 2.8 but showing the entire collapse, as well as animations of the full simulation cells—all prepared at the same physical-time frame rate—are available in Appendix V. They show the evolution of the flows, which are

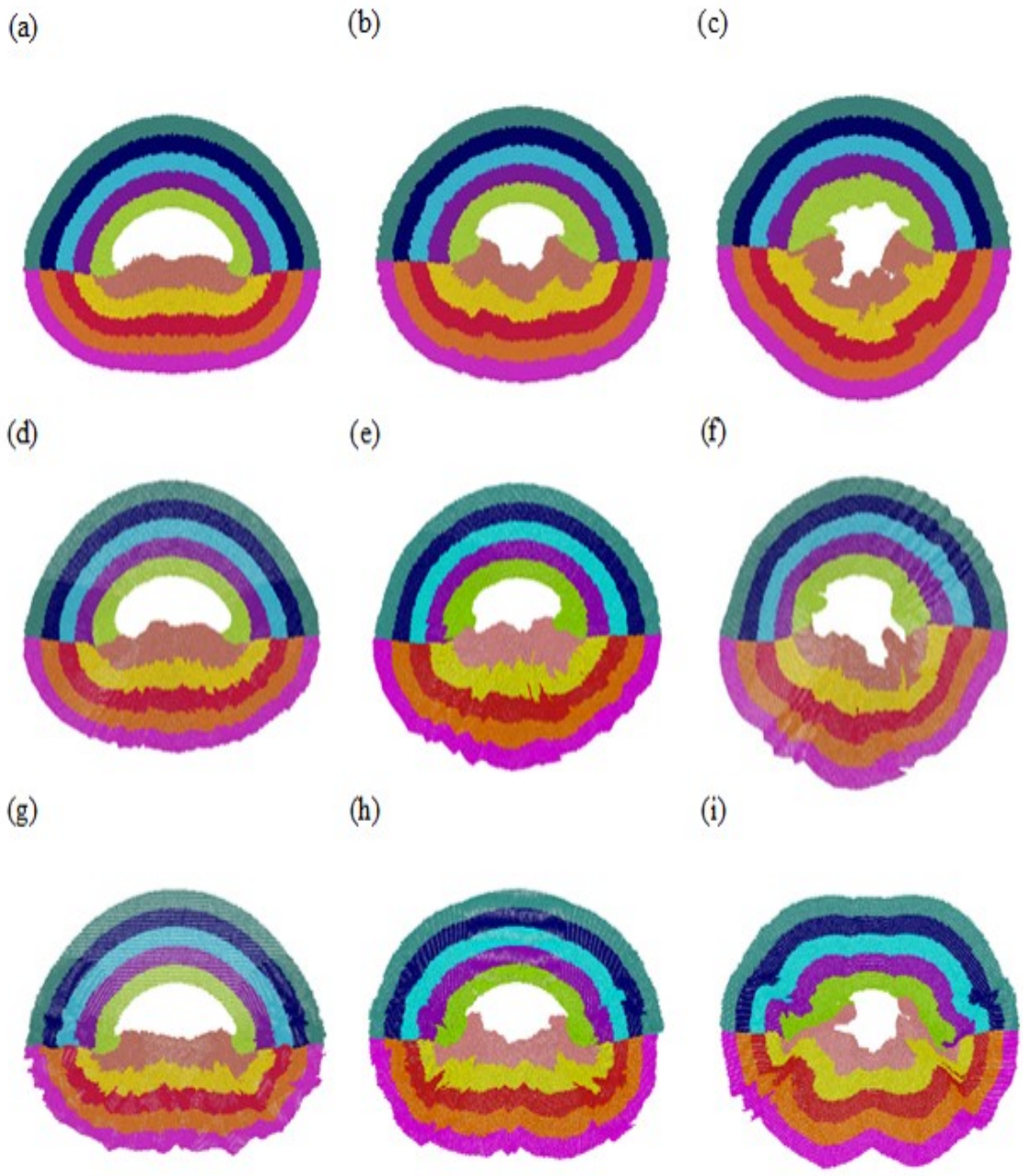

Figure 2.8: Snapshots of material flow in the vicinity of the pore at selected instants, simulated using MD, for all three impact speeds and all three crystal orientations. Top row: $\theta = 0$; middle row: $\theta = 45°$; bottom row: $\theta = 90°$. Columns from left to right: impact speeds of 2.0 km s^{-1} (panels (a), (d), and (g)), 1.0 km s^{-1} (panels (b), (e), and (h)), and 0.5 km s^{-1} (panels (c), (f), and (i)). The instants shown correspond to the times for which $A_{pore}(t)/A_0 = 0.20$, 0.15, and 0.10 for impact speeds of 2.0 km s^{-1}, 1.0 km s^{-1}, and 0.5 km s^{-1}, respectively.

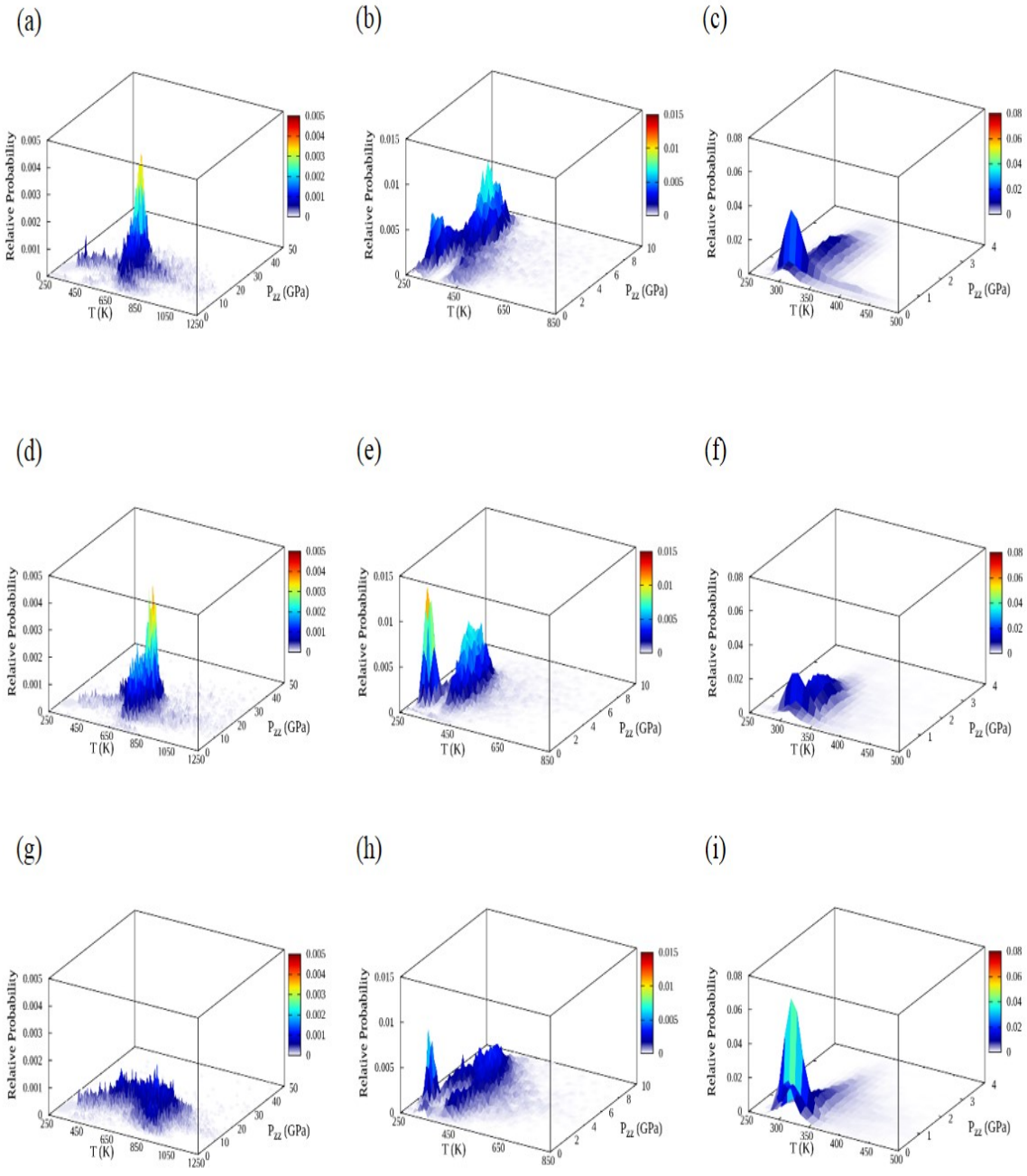

Figure 2.9: As in Figure 2.8, but for histogrammatic distributions of the relative probabilities of local (T, P_{zz}) states in the sample, calculated using MD, at the instants of complete pore collapse. The abscissa and ordinate ranges vary from one column (impact speed) to the next but are consistent within a given column.

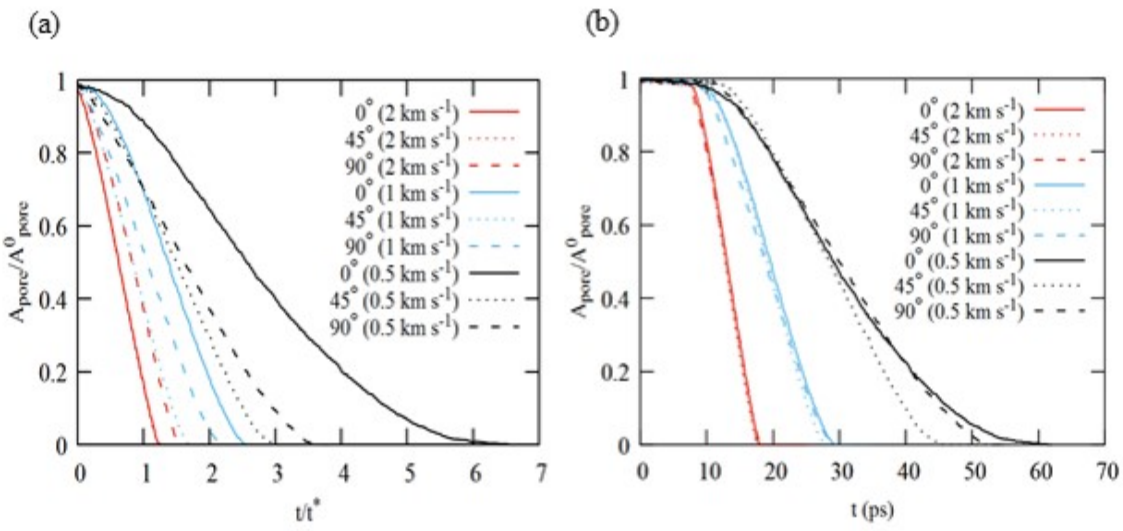

Figure 2.10: (a) Comparisons of scaled pore area $A_{pore}(t)/A_0$ *vs.* scaled time t/t^* for the MD simulations, for three different impact speeds 0.5 km s^{-1} (black), 1.0 km s^{-1} (blue) and 2.0 km s^{-1} (red), and three different orientations, $\theta = 0$ (solid curves), 45° (dotted curves), and 90° (dashed curves). (b) As in panel (a), but plotted against physical time t.

quite distinct and exhibit interesting patterns of material entrainment in the vicinity of the collapse. While the panels of Figure 2.8 are evocative, Secs. 2.4.2.1.1 – 2.4.2.1.3 are best read in conjunction with the animations.

2.4.2.1.1 Shock parallel to the molecular layers. The results for $\theta = 0$ are shown in the first row of Figure 2.8. For the 2.0 km s^{-1} impact, a two-lobed jet is beginning to form (brown material in panel (a)). Involution is still underway at the instant shown, but is essentially complete when the jet strikes the downstream pore wall such that a nascent plug-shaped jet impacts that material. The flow of the brown material is essentially vertical throughout the collapse. High-shear entrainment of material above the pore equator into the flow leads to formation of lobes that develop some amount of vorticity post-closure (green and green-brown interface), though not

to the extent observed in the continuum simulations. In this high-velocity, inertia-dominated case, the surface of the pore is relatively smooth and the pore shape throughout collapse is close to symmetric, for all three crystal orientations (different rows in the first column), showing the near-hydrodynamic nature of material flow.

For the 1.0 km s^{-1} impact, material is extruded from the pore wall in regions at and just below the equator (brown, panel (b)). Flow from the upstream pole is slower than for the extruded material. At later times the extruded material is accelerated and forms two 'proto-jets' that flow symmetrically toward the downstream wall (green) at an angle of approximately $|45°|$ from the horizontal. This material sweeps along the periphery of the downstream wall and entrains some material from it. The two flows strike the downstream wall on either side of the centerline and are deflected horizontally inward such they collide at the pore vertical centerline. The final remnant of the pore is pinched shut interior to the brown region. Some material further upstream (yellow and red) from the pore surface is pulled nonuniformly into the pore-collapse flow. The effects of material mechanics are apparent in these regions, as the flow is not completely smooth. Note that in this 1.0 km s^{-1} case the MD calculations show two proto-jets forming and impinging on the downstream pore surface for all three crystal orientations. By contrast, in the continuum calculations, only one central (and better formed) jet is observed as can be seen in panels (d)-(f) and (j)-(l) of Figure 2.5.

The most distinct differences between MD and continuum results are seen for the lowest velocity case of 0.5 km s^{-1}. In this case, shown in Figure 2.8(c), the MD pore collapse is asymmetric and occurs by a pinching mechanism without distinct jets. Rather, there are deformations in both the upstream and downstream sides of the pore in contrast to the 2.0 km s^{-1} case where the downstream regions near the pore are nearly undeformed until upstream material impinges on the downstream wall.

These results are consistent with the results of recent MD simulations of controlled uniaxial strain and strain-rate deformation[106] and 1.0 km s^{-1} shock-wave simulations[112] of TATB, both performed for the case of no pre-existing defects and using essentially the same force field as here.

2.4.2.1.2 Shock at 45° relative to the molecular layers. The results for $\theta = 45^\circ$ are shown in the second row of Figure 2.8. The result for the 2.0 km s^{-1} impact (panel (d)) is qualitatively similar to that for $\theta = 0$ at the same impact speed. At the instant shown, the collapse is less symmetric than for $\theta = 0$, but a vertically propagating proto-jet forms and by the time it strikes the downstream wall it is essentially symmetric about the vertical pore centerline, although the shape of the final 'mushroom' formed is less perfect. However, in contrast to the $\theta = 0$ case, here the inflow of material into the pore region is less symmetric and exhibits strong 'intrusions' of material from one semi-annulus into that of another. The lack of symmetry of the inflow about the vertical pore centerline is due to the differing crystal surfaces exposed on the left-hand and right-hand surfaces of the pore. For surface material at polar angles $|45^\circ|$ below the equator, to the left the maximum shear stress induced by shock passage acts perpendicular to the molecular layers; whereas to the right it acts parallel to them. Given that basal plane slip is the most facile plastic deformation mechanism in TATB,[44,119] this asymmetry in mechanical response leads to different slip, failure, and flow mechanisms to the left and right of the centerline. At later times, these differences become increasingly apparent in the flow. Finally, for material initially further from the pore surface, flow in the first and third Cartesian quadrants is noticeably different from that in the second and fourth quadrants, with larger and more complicated intrusions in the latter quadrant pair than the former.

For the 1.0 km s^{-1} impact (panel (e)), the flow is less symmetric compared to the

2.0 km s^{-1} case. Material to the right of the vertical centerline strikes the downstream pore wall slightly sooner than does material to the left and final pore closure occurs to the left of the centerline. The inflow patterns are more complicated than for the (45°, 2.0 km s^{-1}) case and far more so than for any of the $\theta = 0$ cases discussed in Sec. 2.4.2.1.1.

For the 0.5 km s^{-1} impact (panel (f)), the flow is less symmetric than for any of the cases discussed thus far. Collapse clearly occurs over the entire surface of the pore. The flow is distinct in all four quadrants but generally corresponds to localized extrusion of material into the pore in the second and fourth quadrants *vs.* formation of broader bulge-like flow in the first and third. Final collapse occurs in the irregularly shaped remnant of the original pore, entirely within the green region of material (which initially defined the semi-annulus of material at the pore surface above the equator) with the exception of a tendril-like intrusion of brown material originally located at the pore surface below the equator. The final flow pattern is decidedly asymmetric.

2.4.2.1.3 Shock perpendicular to the molecular layers. The results for $\theta = 90°$ are shown in the third row of Figure 2.8. Collapse for the 2.0 km s^{-1} impact is symmetric about the vertical centerline (panel (g)). From the time the flow reaches the equator, what is essentially a flat-top plug of material extending across the entire horizontal diameter of the pore flows vertically upward, closing the pore with left-right symmetry. The symmetry of the final mushroom formed is intermediate between those for the other two 2.0 km s^{-1} impact cases; more so than for $\theta = 45°$ (panel (d)) but less so than for $\theta = 0$ (panel (a)). Analogous comments apply regarding the intrusions.

Collapse for the 1.0 km s^{-1} impact is also nearly symmetric about the vertical cen-

terline and dominated by nearly vertical flow (panel (h)), but in this case, rather than a flat-topped flow, once material initially at the pore surface near the equator begins to move upward it does so more rapidly than material initially at the lower pole. As the collapse proceeds, this initially equatorial material sweeps across the downstream pore wall and is deflected such that in the final stage of closure this material is essentially flowing horizontally toward the vertical centerline. The two counterflowing horizontal branches collide almost simultaneously with arrival of material initially at the lower pole, likely decreasing the strength of the impact of upstream material onto the downstream wall.

Collapse for the 0.5 km s^{-1} impact (panel (i)) is both symmetric and relatively smooth until material in the vicinity of the equator begins to flow. From that time onward symmetry is broken, though not as drastically as was the case for (45°, 0.5 km s^{-1}) (panel (f)). Material from both ends of the equator is launched into the pore region at relatively low angles relative to the equator. Flow from the right is composed almost entirely of material initially below the equator (brown) whereas from the left it is composed approximately equally of material from above and below the equator (green and brown). Both regions of flow skirt the downstream pore wall, but more closely and with less subsequent entrainment of material from above the equator for flow from the right compared to from the left. Small, transient sub-pores are formed and closed. The final cavity is highly irregular in shape and entirely embedded in material that was originally located near the upstream pore surface (brown). The complexity of the final flow pattern is arguably similar to that for (45°, 0.5 km s^{-1}) but the degree of distortion, and abrupt disruption, of the semi-annular rings is much greater.

2.4.2.2 Simultaneous probability distributions of temperature and longitudinal stress at the instants of pore closure

Figure 2.9 contains, for all nine simulations, simultaneous normalized probability distributions of temperature and stress component P_{zz} at the instants of complete pore closure (which can be read from Figure 2.10(b)). The arrangement of panels is the same as in Figure 2.8: $\theta = 0$, 45°, and 90° from top to bottom and impact speeds 2.0 km s^{-1}, 1.0 km s^{-1}, and 0.5 km s^{-1} from left to right. Ordinate and abscissa scales are consistent within a given column (*i.e.*, for all three orientations at a given impact speed) but differ from one column to the next (*i.e.*, for different impact speeds). For the 2.0 km s^{-1} impacts (left-hand column), the lead shock has not reached the end of the sample at the instant of analysis. Although the distributions are for the entire sample, for presentation purposes we have manually suppressed the intense peak at (300 K, 0 GPa) that otherwise would dominate the amplitude for the 2.0 km s^{-1} impacts.

As expected, the general trend is a shift toward increasingly high temperature and P_{zz} values with increasing impact speed. Nominal most-probable P_{zz} values at the instants of analysis are approximately 10 GPa, 4 GPa, and 1 GPa for successively slower impact speeds. These values are lower than for corresponding shocks in bulk crystal (20 GPa, 12 GPa, and 5 GPa). The most likely explanation for this is the effect of material flow into the pore. [We confirmed that P_{zz} values in the present simulations, evaluated just prior to the shock striking the pore for material between the piston and the pore (but at least 10 nm from either), agree with the bulk shock speeds.]

Some interesting features are apparent. For example, whereas the 2.0 km s^{-1} impacts (left-hand column) yield qualitatively similar distributions for $\theta = 0$ and 45° (panels (a) and (d)), the result for 90° is distinctly different (panel (g)). All three

distributions exhibit a branch that extends to low T and P_{zz}, but the distribution for 90° exhibits significant amplitude over a larger temperature interval than do the other two cases. The distinct peak in temperature for 0° and 45° is perhaps due to the proto-jet formation noted in connection with Figures 2.8(a) and 2.8(d) versus the flatter flow toward the pore surface in Figure 2.8(g).

All three 1.0 km s^{-1} impacts (center column) yield strongly bimodal distributions along the temperature axis and horseshoe-shaped distributions in the overall (T, P_{zz}) space. The amplitude along the horseshoe is different from one orientation to the next. The $\theta = 90°$ distribution (panel (h)) exhibits a flatter ridge along P_{zz} on the 'high temperature' arm of the horseshoe, compared to the other two orientations. The amplitude along the pressure axis for the 45° orientation (panel (e)) does not extend to as large P_{zz} values as for the other two orientations at the same impact speed.

For 0.5 km s^{-1} impacts (right-hand column), the distributions for the three orientations are quite distinct from their counterparts in the 1.0 km s^{-1} and 2.0 km s^{-1} cases. The region of high amplitude for $\theta = 45°$ (panel (f)) is broad and weakly bimodal along the P_{zz} axis compared to that for the 90° case (panel (i)), which features a sharp single peak located at $P_{zz} \approx 1$ GPa.

The aprons of the distributions differ from one case to the next. (Recall that results in different columns are plotted on different abscissa intervals.) The regions corresponding to high T and P_{zz} are of greatest interest with respect to ignition of chemistry. It is likely that the distributions would shift toward higher temperatures and pressures at a slightly later post-closure time, but the instant of pore closure is well-defined for all systems. An analysis designed to capture transient amplitude in the high-(T, P_{zz}) regions of the aprons is certainly feasible but would require detailed analysis of the simulations and is beyond the scope of the present study. We hope to report on this in the future.

2.4.2.3 Time scales for pore collapse

Figure 2.10(a) shows scaled pore area $A_{pore}(t/t^*)/A_0$ *vs.* scaled time t/t^*. Figure 2.10(b) shows the same ordinate data as Figure 2.10(a) but plotted against physical time in picoseconds. Solid, dotted, and dashed curves correspond to shock directions parallel, at 45°, and perpendicular to the molecular layers in the unshocked crystal ($\theta = 0$, 45°, and 90°, respectively). Red, blue, and black curves correspond to impact speeds of 2.0 km s^{-1}, 1.0 km s^{-1}, and 0.5 km s^{-1}, respectively. Because A_0 is the same in all cases, ordinate values in the figure panels can be compared directly. However, the shock speeds differ from one combination of crystal orientation and impact speed to the next (see Table 2.1) and, thus the scaled times must be interpreted with care.

Consistent with an expectation of largely hydrodynamic collapse, for the strong shocks (red) pore closure for all three orientations is complete at scaled time t/t^* close to unity (Figure 2.10(a)); $t/t^* \approx 1.5$ for $\theta = 90°$ and ≈ 1.2 for $\theta = 0$ and 45°, for which the profiles are almost indistinguishable. The largest value of t/t^* at pore closure, 6.2, occurs for (0°, 0.5 km s^{-1}) for which strength properties are clearly important. The values of t/t^* at pore closure for any given impact speed are larger than those for higher shock strengths. No obvious orientation-dependent trends are evident.

Figure 2.10(b) shows the data just discussed but plotted against physical time. The weaker the shock the larger the collapse time. There is very little orientation dependence of either the collapse time or the time history for the 2.0 km s^{-1} and 1.0 km s^{-1} impact speeds (red and blue). The situation is different for the 0.5 km s^{-1} cases (black), for which the range of orientation-dependent collapse times spans nearly 25%, in a way that does not correlate with the bulk shock speeds). For the 0.5 km s^{-1} impacts, the material properties strongly affect the collapse. For the higher velocity cases, the collapse process is dominated by inertia; the collapse is nearly hydro-

dynamic and therefore is less sensitive to the crystalline orientations, even for the strongly anisotropic TATB crystal.

2.4.3 Continuum sensitivity to models for the melt curve and specific heat

In Sec. 2.4.1, we compared MD and continuum predictions of pore collapse over a range of shock strengths. While broad similarities in predicted pore closure histories and flow fields were demonstrated, important differences between MD and continuum predictions are apparent. In particular, the tail of the temperature distribution in the hotspot, the distribution of temperature around the hotspot, and the evolution of pore shapes during collapse all exhibit differences between the MD and continuum predictions. In Sec. 2.4.2, we evaluated the variation of MD results due to anisotropy, which is not modeled in the present isotropic continuum calculations. This provided insight into the degree of variability in response with respect to crystal orientation for a given impact speed.

In this subsection, we assess how strongly other modeling assumptions, in particular thermophysical model functional forms and parameters, affect the continuum predictions. Two primary inputs to the continuum model are examined, namely the models for melting temperature and specific heat. Each model is evaluated independently for shock speed 1.0 km s^{-1}. Taken together, the studies in this subsection and Sec. 2.4.2 provide insights into why MD and continuum models yield different results.

2.4.3.1 Effect of the melting-point model

Figure 2.11 shows the comparison of pore shape and temperature, at two instants of time, for the three different models for melting temperature depicted in Figure 2.2(a).

Results in the left-hand column of Figure 2.11(panels (a) and (d)) were obtained using an MD-derived[44] pressure-dependent melt curve $T_m = T_m(P)$. Those in the center and right-hand columns were obtained using a pressure-independent melting point, T_m = constant, for two different normal melting points taken from the literature; T_m = 623 K[174] (center, panels (b) and (e)), and T_m = 725 K[44] (right, panels (c) and (f)). The top row (panels (a)-(c)) compares the pore shape and temperature at time $t = 30$ ps, close to the time of pore closure; and the bottom (panels (d)-(f)) at $t = 36$ ps, which is post-collapse. In all six figure panels, melted regions are shown in black. The simulations were performed using the constant specific heat corresponding to the MD simulations. Recall that when the material melts, the strength goes to zero.

The results in Figure 2.11 are consistent with qualitative expectations: The temperature-dependent melting model, for which the melting point increases by ≈175% between 0 and 2 GPa, yields the least melting (left-hand column). Comparing results for the two constant-melting-point models, more extensive melting occurs when $T_m = 623$ K (center column) than when $T_m = 725$ K (right-hand column).

The largest qualitative difference among the results in Figure 2.11 is that the two constant-melting-point models both predict melting all along the downstream pore wall stagnation zone and in the regions of vortical roll-up, whereas melting is largely localized to regions of vortical roll-up when the pressure-dependent melting model is used. These observations apply at both times studied.

Despite these differences in location and extent of melting obtained using the three models, the overall temperature fields and wave profiles are quite similar at a given time, as are the qualitative features of hotspot shape and size. For the 1.0 km s^{-1} impact studied, the rather restricted zone of melting diminishes the influence of the melting-point model. The effect is expected to be even smaller for weaker impacts

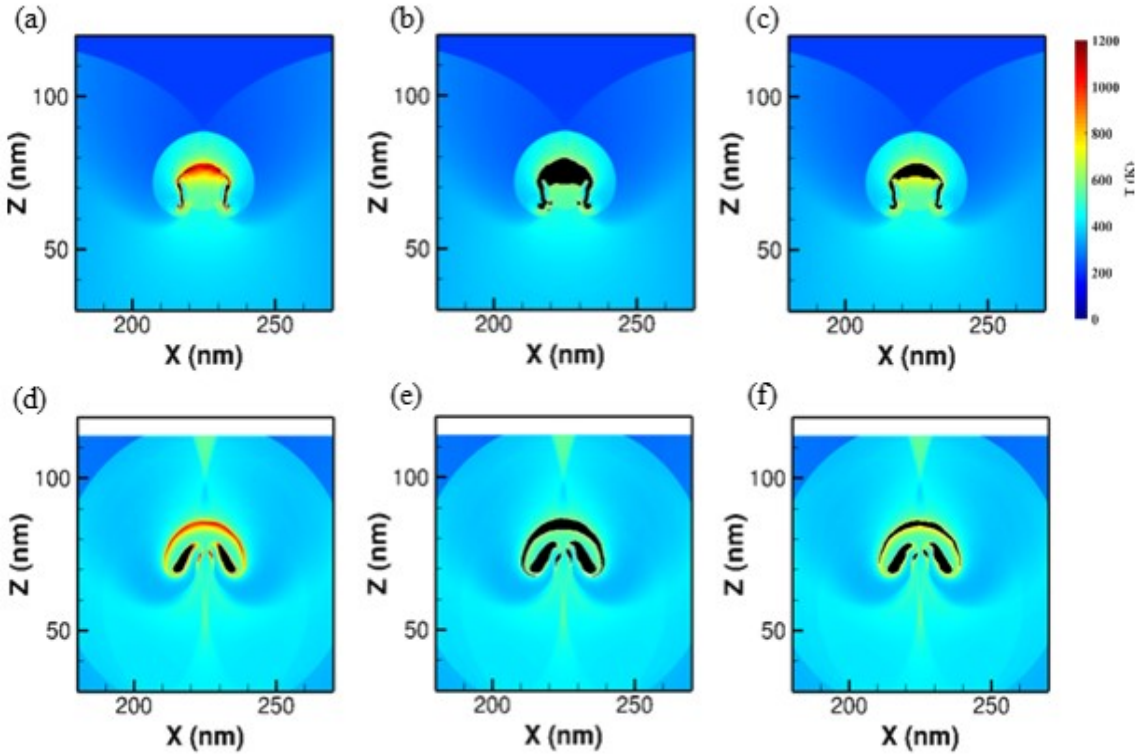

Figure 2.11: Effect of melt-curve model in the continuum simulations for the 1.0 km s^{-1} impact. Top row: pore shape, temperature, and melt regions at time $t = 30$ ps, for: (a) $T_m = T_m(P)$; (b) $T_m = 623$ K; (c) $T_m = 735$ K. Bottom row (panels (d)-(f)): as in the top row, but for $t = 36$ ps. In all cases, melted regions are colored black. All six simulations were performed using the constant specific heat value corresponding to the MD simulations.

due to decreased melting; whereas for stronger impacts pore collapse will be hydrodynamic such that strength effects, including the drop of material strength to zero upon melting, will likely play a minimal role. Therefore, from a purely thermo-mechanical perspective, the model for melting temperature does not seem to exert a strong influence on the predictions. The situation might be quite different when chemistry is included, for example if liquid reaction rates are significantly higher than those in the crystal at the same temperature and pressure.

2.4.3.2 Effect of the specific-heat model

A second material property that can affect calculated hotspot characteristics is the specific heat. Various values of the specific heat for TATB have been published.[174,177,183] Here, we consider two different models for the specific heat; one using a constant value $C_v = 2126$ J kg^{-1} K^{-1} corresponding to the present MD simulations and a temperature-dependent model $C_v = C_v(T)$ that emulates the quantum-mechanical temperature dependence. These models are depicted in Figure 2.2(b). Recall that the quantum-based specific heat approaches the classical value, from below, for temperatures greater than $\sim$1000 K. Thus, the qualitative expectation is that the quantum-based specific heat will yield higher temperatures compared to when the classical specific heat is used. The results discussed below were all obtained for the 1.0 km s^{-1} impact speed in conjunction with the pressure-dependent melting-point model.

Figures 2.12(a-b) provide comparisons of temperature fields in the sample at a selected instant ($t = 24$ ps) during pore collapse, for both specific-heat models. Panels (a) and (b) contain predictions for the classical and quantum-based specific heats, respectively. As expected, use of the temperature-dependent (quantum-based) specific heat yields higher temperatures overall than when the constant specific-heat (classical) model is used. Away from the pore the difference is approximately 50 K for the

impact studied. However, the qualitative features of pore collapse in Figures 2.12(a) and 2.12(b) are otherwise similar.

Figures 2.12(c-e) contain time histories for local temperature at three different locations in the sample. Blue and red curves correspond to continuum simulations performed using the classical and quantum-based specific heats, respectively. Also shown are the corresponding predictions from MD ($\theta = 45°$, black curves). The results were obtained for small test volumes located along the vertical centerline of the pore (as was done for the t-z diagrams discussed in Sec. 2.4.1.1). Panel (c) is for a test volume located 40 nm upstream from the location at which pore closure occurs; this test volume is well-removed from the pore region. Panel (d) corresponds to the location at which pore closure occurs. Panel (e) is for a region 5 nm downstream from the location of pore closure. The locations used in panels (c)-(e) were determined independently for the continuum and MD simulations, based on the t-z data for the 1.0 km s^{-1} impact in Figure 2.3. The locations in panel (d) serve as reference values against which the locations used in panels (c) and (e) were specified.

Focusing on the continuum models (blue and red) for the test volume well ahead of the pore (panel (c)), shock wave arrival at $t \approx 10$ ps leads to temperature jumps of ≈125 K (classical C_v) and ≈175 K (quantum-based C_v). This approximately 50 K difference between temperatures for the two models at this location in the sample is maintained for the rest of the simulation, despite subsequent heating in the flow and arrival of a reflected shock from the pore surface at $t \approx 33$ ps. For material located at the point of pore closure (panel (d)), the test volume is initially located inside the pore such that the temperature is 'zero' (*i.e.*, there is no material in the test volume). When collapse occurs at the test volume location ($t \approx 28$ ps), a transient peak emerges with temperatures between ≈900 K and ≈1000 K depending on specific-heat model. The temperature jump is very sharp as the sample volume

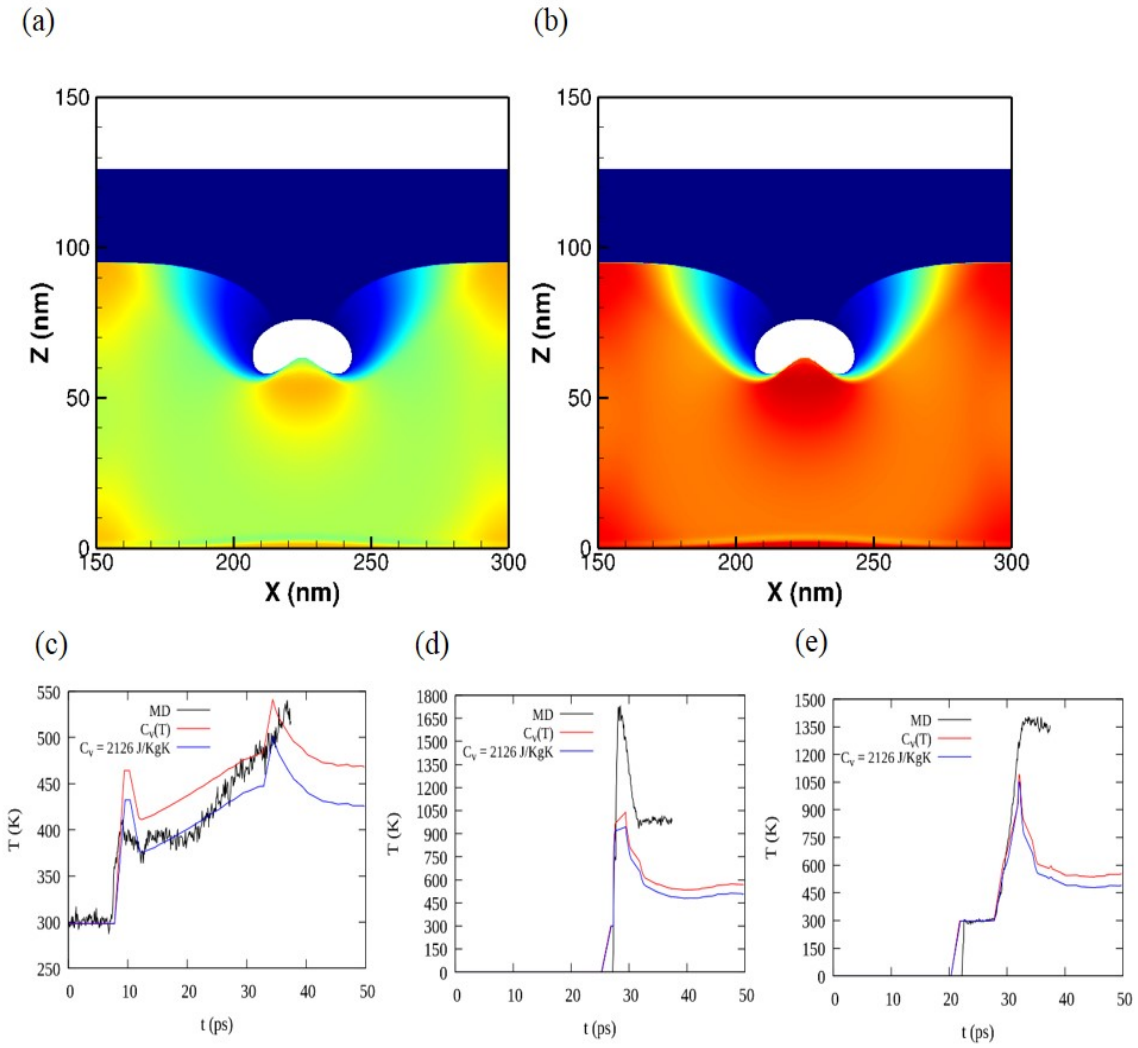

Figure 2.12: Effect of specific-heat model in the continuum simulations for the 1.0 km s^{-1} impact. Top row: 2D maps of temperature at $t = 24$ ps for: (a) $C_v = 2126$ J kg^{-1} K^{-1} (corresponding to the MD simulations); (b) $C_v = C_v(T)$ (quantum-based). Bottom row: Time histories for temperature at three different locations along the vertical centerline of the pore, obtained from continuum mechanics with both specific-heat models and from MD (for the case $\theta = 45°$). Blue: continuum with $C_v = 2126$ J kg^{-1} K^{-1}; red: continuum with $C_v = C_v(T)$; black: MD. (c) 40 nm upstream from the location of pore closure; (d) location of pore closure; (e) 5 nm downstream from the location of pore closure. The locations of pore closure were extracted from the relevant t-z diagrams in Figure 2.3. Both continuum simulations were performed using the pressure-dependent melting curve obtained from MD.

is located precisely at the point where the jet impacts the downstream pore wall. As with material ahead of the pore, and as expected, the quantum-based specific heat leads to the larger temperature; and this temperature difference is essentially maintained for longer times. For material initially 5 nm downstream from the pore (panel (e)), material flows into the test volume prior to shock arrival, hence the initial jump from "$T = 0$" to $T = 300$ K at $t \approx 22$ ps. When the collapse-induced shock reaches this test volume ($t \approx 28$ ps) there is a large temperature jump from 300 K to ≈ 1000 K (classical) and ≈ 1050 K (quantum-based). Whereas shock arrival ahead of the pore and at the collapse stagnation point is almost instantaneous, in panel (c) the temperature jump occurs over an interval of ≈ 3 ps. The temperature excursion relaxes toward $\approx$500 K – $\approx$550 K over the subsequent $\approx$8 ps. As with the other cases, the classical specific heat leads to lower temperatures than does the quantum-based model.

Figure 2.12(c) shows that the effect of the different models for C_v on the calculated temperature value is rather modest. At early stages, prior to pore collapse, this can be expected from the expression for C_v in Eq. 2.14 as, at lower temperatures, the effect of temperature on C_v will be overshadowed by the first, adiabatic compression, term in Eq. 2.14. This situation holds for the first location in Figure 2.12(c), that is, 40 nm upstream of the pore since the temperature rise at that location is mainly due to bulk shock heating, as can be seen in Figure 2.12(d). It would be expected that as the temperature rises, for example, at the downstream location (Figure 2.12(d)), which is collocated with the pore collapse site, the effect of different C_v models would become stronger, since the second term on the right hand side of Eq. 2.14 will play a predominant role at such locations. However, at the high temperatures resulting at the collapse zone, the temperature dependent model for C_v approaches the classical constant C_v value. Therefore, the differences between the classical and quantum-

derived specific heat models are small at higher temperatures. This in turn leads to modest differences in the resulting temperature values at the post-collapse location as well, as seen in Figure 2.12(e). Thus, the continuum calculations show limited deviations due to the two different treatments of C_v with regard to the computed post-collapse temperature fields over the entire duration of pore collapse and hotspot generation.

Focusing now on comparisons between the continuum and MD results in Figures 2.12(c-e), one can see from panel (c) that ahead of the pore the temperature time history from continuum mechanics with the classical C_v model (blue) closely matches the MD prediction (black), consistent with expectations. Note however that the peak temperature in panel (c) associated with lead shock arrival ($t \approx 10$ ps) is higher in the continuum simulation than from MD by ≈30 K. The two temperature peaks relax back to approximately the same temperature over an ≈5 ps interval. For times greater than ≈25 ps the temperature in the MD simulation increases at a greater rate than in the continuum simulation. We suspect, but cannot prove as of this writing, that this is due to plastic flow and heat dissipation mechanisms that are present in the MD but not accounted for in the continuum model.

The differences between predictions from continuum mechanics and MD are much larger in Figures 2.12(d-e). In particular, although the shock arrival times and slopes of the shock-rise profiles at the locations of pore collapse are quite similar (panel (d)), the magnitudes of both the transient temperature rise and the long-term temperature from MD are approximately twice as large, referenced to 300 K, as when modeled using continuum mechanics with either specific-heat model. The situation is similar in the downstream heating region captured in panel (e) except that, while still large, the disparity between MD- and continuum-based transient temperature rises is not as large as was the case at the location of pore closure (panel (d)) and the subsequent

decrease toward a long-time temperature appears to be slower in the case of MD. Understanding these differences would be quite attractive as a topic for future study.

2.5 Discussion

2.5.1 MD predictions

It is important to recognize that finite-size effects will exist in the present MD simulations. Although the numbers of atoms are 'large', the quasi-2D simulation cells are quite thin in one direction. Practically, this dictates that defects which nucleate and grow to more than approximately two crystallographic unit-cells extent along the thin direction will either be blocked or fill the sample at an unrealistic density along the shock direction, due to geometric constraints imposed by the periodic boundary conditions. However, we think the salient features of the collapse studied here would be preserved for cylindrical collapse in fully 3D simulation domains: Prior to shock arrival at the upstream pore surface, the present simulations yield deformation mechanisms that are qualitatively similar to those reported for controlled-strain, controlled strain-rate, rigid-molecule MD simulations of initially defect-free TATB[106] as well as all-atom MD simulations of explicit shocks in oriented, initially defect-free 3D (as opposed to quasi-2D) samples.[112]

2.5.2 Continuum predictions

The continuum models in this paper adopted material parameters that are largely derived from MD simulations and therefore closely reflect the material response modeled in the atomistic calculations. The primary difference and the largest effect that led to differences between the MD and continuum results is therefore the material strength

model and the anisotropy of the TATB material. Although the overall collapse behavior of the continuum calculations is in general agreement with the atomistic results, key features of the hotspot that are relevant to ignition and initiation exhibited important differences that need to be understood. The features of primary concern are differences in the tails of the temperature distributions (Figure 2.7) and significantly different transients and long-time temperatures observed in the time histories shown in Figures 2.12(d-e). Both of these would surely affect the ignition of hotspots and the subsequent growth or quenching of the hotspot. For greater confidence in hotspot ignition and growth in continuum mesoscale simulations, models for material deformation, guided by MD calculations, will need to be improved before they can be relied upon for extracting hotspot ignition and growth rates. An obvious initial path forward would be incorporation of dislocation-based plasticity in the continuum simulations with specific parameterization obtained from MD simulations. A forthcoming conference proceeding[83] suggests that this would significantly improve the agreement between MD and continuum predictions for pore collapse in TATB. Another feature that will need to be incorporated is anisotropic strength.

2.5.3 Additional thoughts

The MD results for temperatures around the collapsed pore indicate, counterintuitively, that for the higher velocity impacts the effects of shear may be significant because of the formation of shear bands (Figures 2.4 and 2.5). This can affect the environment for the hotspot that results from pore collapse and can change the hotspot evolution characteristics. In the case of weaker impacts the effect of shear may not be as significant as naively expected, as the temperature rise in the shear bands is rather modest (Figure 2.6). Rather, as mentioned above, for the weaker impacts a

high-fidelity mechanical description will likely be required to bring the salient features of the continuum pore-collapse simulations into better agreement with the MD predictions.

The impact of anisotropy on the differences between MD- and continuum-based temperature fields appears to be significant. The effects of material models and parameters, such as the melting point and specific heat studied here, appear to exert relatively little effect on the continuum pore-collapse results for the conditions studied. Nevertheless, the results presented here serve to focus attention on the types of data and models that need to be improved for reliable mesoscale continuum computations of hotspot generation due to pore collapse.

Although our strategy is to focus first on the non-reactive response, the need to incorporate chemistry into the simulations is obvious: For the stronger shocks studied here, pore collapse leads to local transient temperatures in excess of 2000 K. Ignition of chemistry is expected to couple to and modify the flow, with the eventual outcome–*i.e.*, growth of chemistry or quenching—determined by a complicated, indeed complex, interplay among physical and chemical factors. We hope to investigate this in future studies.

2.6 Conclusions

We present head-to-head comparisons of MD and continuum pore-collapse simulations for TATB. As far as possible, material properties for the continuum pore-collapse calculations were drawn from MD data. Crystalline TATB is a good candidate material for such comparisons due to the extreme structural anisotropy and because the crystal structure is triclinic, which is the most general crystal symmetry class. The continuum model in the present study is isotropic whereas the MD simulations implicitly

incorporate the anisotropy of the crystal.

The predicted MD and continuum results are in broad agreement as regards overall pore collapse characteristics such as pore volume evolution, shock and blast-wave propagation, and general aspects of temperature distribution. However, there are distinct differences in key quantities of importance to hotspot ignition and growth, including the high-temperature tail of the temperature distribution and the temperature field in the vicinity of the post-collapse hotspot. These differences are mainly due to the nature of collapse of the pore and, we think, arise from anisotropy and material deformation patterns that are present in the MD simulations but cannot be accounted for in the present baseline continuum description.

The sensitivity to thermophysical parameters, specifically the pressure dependence of the melting temperature and the temperature dependence of the specific heat, are shown to have noticeable but modest effects on the hotspot temperature following pore collapse in the continuum calculations, at least for the configuration and impact conditions studied and in the absence of chemistry. The relative insensitivity to these models suggests a critical need to account for anisotropic strength and explicit crystal plasticity in the continuum framework.

Future efforts should focus on obtaining better fundamental material model descriptions, ideally guided by both MD and experiments, so that continuum pore-collapse-mediated hotspot ignition and growth rates can be predicted accurately. Once this is achieved, the collective response of fields of pores or other defect structures can be usefully studied to provide datasets for the construction of homogenized macroscale continuum models. Further, once the overall approach has been successfully developed and demonstrated for one energetic material, it should be readily adaptable to others.

2.7 Acknowledgments

This work was a collaboration with Prof. Udaykumar's group at University of Iowa. This work was performed under the auspices of grants from the U.S. Air Force Office of Scientific Research (AFOSR) within the Dynamic Materials and Interactions (DMI) portfolio (program officer: Dr. Martin J. Schmidt). Puhan Zhao and Tommy D. Sewell were supported by grant number FA-9550-16-1-0437. Sangyup Lee and H. S. Udaykumar were supported by grant number FA9550-15-1-0332. The MD simulations were enabled by a special grant of 500,000 high-priority core-hours on the "Lewis" high-performance institutional computing infrastructure provided by Research Computing Support Services at the University of Missouri-Columbia. The Lewis cluster is partially supported by a grant from the National Science Foundation under grant number CNS-1429294.

Chapter 3

Application of Strain Functional Analysis to Shock-Compressed Oriented TATB Crystals

3.1 Abstract

A new approach for characterizing the local configuration of particles in atomistic simulations, referred to as Strain Functional Descriptors (SFDs), has recently been developed. In this method, discrete quantities from Molecular Dynamics (MD) simulations such as number density, velocities, and forces are mapped onto continuous fields using a Gaussian kernel. The local particle configurations in Cartesian coordinates are derived from the n^{th} order central moments of the local number density and later transformed to a Solid Harmonics polynomial basis by SO(3) decompositions. A unique and complete set of rotationally invariant SFDs is obtained by applying Clebsch-Gordan coupling to terms in the SO(3) decompositions. This set of descriptors contains geometric meaning of the local particle configurations in terms of size,

shape, and orientation, and uncovers the underlying information on n-fold symmetry axes and net shapes of the local environment. Here, we present a case study by applying the SFDs to MD simulations of shock-compressed TATB crystals. Coupled with machine learning techniques, the SFDs are shown to have successfully identified the defects and deformations presented in the finite temperature MD simulations of TATB, which is triclinic, and thus can be applied to materials with any symmetry.

3.2 Introduction

Extracting information on material response from the atomistic scale is important to the development of fundamental understanding of the macroscopic properties. A common way to achieve this is by characterizing the local configurations/geometries of particles. Defect structures and deformation mechanisms can often be identified using measurements of the local particle environments. Many methods have been developed for this purpose. Some of them are designed for specific structures (especially of higher symmetry class systems),[184,185] and some of them are limited by the symmetry functions used and are not robust under thermal flunctuations.[186–190] Methods that are constructed using information about 'shape, orientation, and geometries' have received much success.[191–196] One approach, which relies on the power spectrum components of the local number density expansion (SOAP descriptors[197–201]), has been used to characterize the atomic environments in grain boundaries of metallic systems.[202] While this approach seems promising, the SOAP descriptors do not provide any underlying information about the symmetry of the local particle environment. The list of studies here is by no mean exhaustive. Interested readers are referred to the article by Stukowski for a more complete and comprehensive review on structural analysis.[203]

A more recent approach, known as the Strain Functional Descriptors (SFDs), has been developed by Mathew *et al.*[204] It provides a complete set of descriptors that characterizes the local particle configurations and identifies symmetry elements. This approach relies on moment analysis, which has been commonly used to characterize three-dimensional (3D) structures.[205] In this approach, the moments are directly related to gradients of local property fields, allowing the SFDs to identify symmetry elements from group theory. In order to obtain the n^{th} order moments, discrete particle properties, such as number densities, velocities, and forces from MD simulations, are first transformed to continuous fields using a Gaussian kernel smoothing function. This is the least-biased smoothing function and has been used in several studies.[206–209] The n^{th} order moments (expressed in the form of rank n Hermite polynomial tensors) are obtained through the Taylor series expansion of the local number density for each particle. For convenience, the Cartesian moments are expressed in terms of harmonic polynomial functions, which transform the moments into an independent frame of reference. For the SFDs to be general, they have to be orientationally independent. That is, they must be described using the 3D rotationally invariant group SO(3), and defects and deformations have to be expressed using the rotationally invariant basis functions of that group. Incorporation of rotational invariance into moment analysis has been achieved with techniques from group theory.[210–212] The set of rotationally invariant SFDs are derived by combinations and contractions of the basis functions using the Clebsch-Gordan coupling coefficients. By trial and error, the unlimited number of possible descriptors are reduced to form a minimal, complete, orthogonal set. This set of SFDs is further coupled with machine learning techniques such as Principal Component Analysis (PCA) and the Gaussian Mixture Model (GMM) to achieve automated detection of defects and deformations in finite temperature MD simulations of metals.

Here, we present a case study of applying SFDs to MD simulations of shock-compressed oriented 1,3,5-triamino-2,4,6-trinitrobenzene (TATB) crystals. The SF analysis was applied to the molecular center-of-mass (COM) quantities. It successfully highlights defects in the system and classifies molecules associated with different deformation mechanisms. The triclinic TATB unit cell is comprised of two molecules, and each molecule consists of a benzene ring bonded to alternating nitro and amino groups. The molecule is planar due to the push-pull intramolecular interactions between the nitro and amino groups and the benzene ring.[154] The crystal consists of planar sheets of planar molecules, sometimes referred to as a graphitic-like crystal packing motif. Molecules within the planar sheets are held together by extensive intermolecular hydrogen bonding, while there are only van der Waals interactions between the molecular layers. The triclinic symmetry of the crystal makes TATB the most general and suitable candidate for studies, as methods applicable for analysis of TATB should be applicable, in principle, to systems of materials with any symmetry class. In this study, MD shock simulations of TATB single crystals with different system dimensions are considered. In one case, the system contains perfect TATB crystals with no pre-existing defects, and the simulation cell is approximately square in the transverse directions and 10 times longer in the longitudinal direction.[112,116] In the other case, a 50.0 nm diameter pore is introduced in the middle of a quasi-2D simulation cell, which is approximately square in the transverse directions and extremely thin in the third direction.[84] (See Ch. 2 for more details.) Both studies were performed using an all-atom fully-flexible force field.[36,39,84,86] Calculated molecular (COM) positions and orientation parameters were used as data for the Strain Functional analysis, which successfully identified the initiation and propagation of defects and deformations throughout the simulations.

Details of the SFDs approach and brief descriptions of the MD simulation methods

are described in Sec. 3.3. Results and discussion of the applications of SFDs to MD simulations are discussed in Sec. 3.4. More precisely, analysis of shock-compressed oriented TATB single crystal is included in Sec. 3.4.1, and analysis of the shock-induced pore collapse in oriented TATB crystal is presented in Sec. 3.4.2. Additional thoughts on directions for future work are given in Sec. 3.5.

3.3 Computational methods

3.3.1 Strain functional descriptors

Strain functional descriptors (SFDs) comprise an exhaustive symmetry-adapted basis that can be used to characterize the configuration of particles in the system. Initially, discrete quantities such as positions, forces, and velocities from MD simulations are mapped onto continuous fields through Gaussian kernels, which have been extensively applied in SOAP[197–201] and the SNAP[206,207] and Moment Tensor Potentials.[208,209] It is considered to be the least-biased kernel.[213] The normalized isotropic Gaussian kernel has the following form,

$$w_j(\mathbf{r}) = \frac{1}{(2\pi)^{3/2}\sigma^3} exp(-\frac{|\mathbf{r}-\mathbf{r}_j|^2}{2\sigma^2}), \tag{3.1}$$

where $\mathbf{r}$ is the general coordinate of a particle of interest, $\mathbf{r}_j$ is the position of the j^{th} neighbor, and σ is the width of the Gaussian distribution and has a unit of length. This kernel function is used to define the number density N in the continuous field,

$$N(\mathbf{r}) = \sum_j w_j(\mathbf{r}) = \frac{1}{V_0}\sum_j exp(-\frac{|\mathbf{r}-\mathbf{r}_j|^2}{2\sigma^2}) \tag{3.2}$$

where

$$V_0 = (2\pi)^{3/2}\sigma^3. \tag{3.3}$$

The width σ is assumed to be constant because the systems consist of TATB crystal only. (SFA is done using molecular properties in this study.) The analogous approach of mapping discrete properties to continuous fields can be applied to other properties including velocities and forces.

The number density can be expanded around the neighborhood of atom i ($\mathbf{r}+\delta\mathbf{r}$) using the Taylor series expansion:

$$n_i(\mathbf{r}) = N(\mathbf{r}_i + \delta\mathbf{r}) \approx N(\mathbf{r}_i) + \delta\mathbf{r} \cdot \frac{\partial N}{\partial \mathbf{r}}|_{\mathbf{r}_i} + \frac{1}{2}(\delta\mathbf{r} \times \delta\mathbf{r}) \cdot \frac{\partial^2 N}{\partial \mathbf{r}^2}|_{\mathbf{r}_i} + \cdots \tag{3.4}$$

Note that the general three-dimensional coordinates $\mathbf{r}$, $\mathbf{r}_j$, and their products (*i.e.* $\delta\mathbf{r} \times \delta\mathbf{r}$) are expressed in tensoral form.

The individual differential terms in Eq. 3.4 can be expressed using Eq. 3.2.

$$\frac{\partial N}{\partial \mathbf{r}}|_{\mathbf{r}_i} = \sum_j \frac{\partial w_j}{\partial \mathbf{r}}|_{\mathbf{r}_i} = -\frac{1}{\sigma}\sum_j \frac{\mathbf{r}_{ij}}{\sigma} w_{ij} \tag{3.5}$$

$$\frac{\partial^2 N}{\partial \mathbf{r}^2}|_{\mathbf{r}_i} = \sum_j \frac{\partial^2 w_j}{\partial \mathbf{r}^2}|_{\mathbf{r}_i} = \frac{1}{\sigma^2}\sum_j (\frac{\mathbf{r}_{ij} \times \mathbf{r}_{ij}}{\sigma^2} - \mathbf{I}_2) w_{ij} \tag{3.6}$$

$$\frac{\partial^3 N}{\partial \mathbf{r}^3}|_{\mathbf{r}_i} = \sum_j \frac{\partial^3 w_j}{\partial \mathbf{r}^3}|_{\mathbf{r}_i} = -\frac{1}{\sigma^3}\sum_j (\frac{\mathbf{r}_{ij} \times \mathbf{r}_{ij} \times \mathbf{r}_{ij}}{\sigma^3} - 3\frac{\mathbf{r}_{ij}}{\sigma} \times \mathbf{I}_2) w_{ij} \tag{3.7}$$

$$\frac{\partial^4 N}{\partial \mathbf{r}^4}|_{\mathbf{r}_i} = \sum_j \frac{\partial^4 w_j}{\partial \mathbf{r}^4}|_{\mathbf{r}_i} = \frac{1}{\sigma^4}\sum_j (\frac{\mathbf{r}_{ij} \times \mathbf{r}_{ij} \times \mathbf{r}_{ij} \times \mathbf{r}_{ij}}{\sigma^4} - 6\frac{\mathbf{r}_{ij} \times \mathbf{r}_{ij}}{\sigma^2} \times \mathbf{I}_2 + 3\mathbf{I}_4) w_{ij} \tag{3.8}$$

Here, w_{ij} represents the function $w_j(\mathbf{r})$ evaluated at $\mathbf{r} = \mathbf{r_i}$, and $\mathbf{I}_2$ and $\mathbf{I}_4$ are the rank 2 and rank 4 identity matrices. The number density of the i^{th} atom depends on its distance to other atoms (*i.e.*, $\mathbf{r}_{ij} = \mathbf{r}_i - \mathbf{r}_j$).

The recursive property of the Gaussian function greatly reduces the complexity of the derivatives: they can be rewritten in the form of scaled Gaussian-weighted sums over the particle distances in the system. The Gaussian kernel also makes higher order derivatives, which cannot be solved analytically with either discrete or low-order polynomial functions, accessible. In addition, geometric information about the neighborhood can be extracted from the simplified derivative terms. For example, the gradient of the number density represents the first-order moment of the spatial distribution of the neighborhood (Eq. 3.5), and the second-order moment of the spatial distribution measures the uniaxial and shear deformation as shown in Eq. 3.6. The identity matrix measures the volumetric strain (*i.e.*, change in size), and terms inside the parentheses together measure the deviatoric strain (*i.e.*, change in shape) of the local neighborhood. The third-order moments are related to three-fold rotation symmetries, centrosymmetry, and the strain-gradient of the local environment. The fourth-order moments indicate four-fold rotation symmetries and cubic crystal symmetries.

The tensor polynomials in Eqs. 3.5-3.8 have the same form as Hermite polynomials. They can generally be written as:

$$\frac{\partial^n N}{\partial \mathbf{r}^n}|_{\mathbf{r_i}} = \sum_j \frac{\partial^n w_j}{\partial \mathbf{r}^n}|_{\mathbf{r}_i} = \frac{1}{\sigma^n} \sum_j w_{ij} \mathbf{H}_n(\frac{\mathbf{r}_{ij}}{\sigma}), \tag{3.9}$$

where $\mathbf{H}_n$ are the n^{th} order Hermite polynomials that are equivalent to terms inside of the parentheses in Eqs. 3.5-3.8. These polynormials can be expressed in terms of individual Cartesian components,

$$\frac{\partial^n N}{\partial x^p \partial y^q \partial z^s}|_{\mathbf{r}_i} = \frac{1}{\sigma^n} \sum_j w_{ij}(x_i - x_j)^p (y_i - y_j)^q (z_i - z_j)^s, \tag{3.10}$$

where p, q, and s are non-negative integers with a sum equals to n.

Generally, information expressed in Cartesian coordinates is less convenient, especially when the symmetry axes do not align with the coordinate axes. The Hermite polynomials in Eq. 3.10 can be rewritten using a rotationally invariant format. This can be achieved by following the method derived from the principles of angular momentum.[210] First, the Cartesian Hermite polynomials need to be transformed to solid harmonics $R^m_{l(n)}$,

$$R^m_{l(n)} = r^{n-l} r^l Y^m_l, l \geq 0, l = n, n-2, \ldots, m = -l, -l+1, \ldots, l-1, l \tag{3.11}$$

where r is the magnitude of the distance vector $\mathbf{r}$, l is the overall order of the harmonic polynomial, and Y^m_l is the spherical harmonic function. The solid harmonic function $R^m_{l(n)}$ contains both the radial dependence and angular dependence terms. Transformation between H_n and $R^m_{l(n)}$ for second, third, and fourth rank tensors has been demonstrated elsewhere.[210,212] Using this, the moments of spatial distribution about atom i can be written as:

$$v^m_{l(n)}(i) = \sum_i R^m_{l(n)}(\mathbf{r}_{ij}) \tag{3.12}$$

The $v^m_{l(n)}$ terms that are expressed in terms of angular momentum functions are elements of the Irreducible or Spherical representation of the moment tensors (Spherical Tensors), which are expressed in terms of the solid harmonics basis. The rotationally invariant descriptors are then derived from the Spherical Tensors using the Clebsch-

Gordan coupling procedure,[211] in which a tensor N can be arbitrarily taken as the product between any two Spherical Tensors using the following equation

$$\mathbf{N}[l_1, l_2]_h^k = \sum_{m=-1}^{m=l} \langle l_1, m, l_2, k-m | l_1, l_2, j, k \rangle v_{l_1(n_1)}^m v_{l_2(n_2)}^{k-m}, \tag{3.13}$$

where N is the tensor of rank h and $|k| \leq h$. The terms inside the brackets $\langle\rangle$ are the Clebsch-Gordan coefficients which indicate the specific terms that are coupled. These coefficients only depend on the values of (l, m) and are independent of (n_1, n_2). There are infinite numbers of possible combinations of tensors. Mathew *et al.*[204] obtained a minimal, complete, exhaustive orthogonal set of the tensors by trial and error. They demonstrated that a unique, one-to-one mapping between the Cartesian moments, Spherical Tensors, and the rotationally invariant terms derived using the Clebsch-Gordan exists up to the 4^{th} order. Those terms are necessary to describe the geometries independent of the coordinate frame and are referred to as the Strain Functional Descriptors (SFDs).

The size of the Gaussian neighborhood σ has been shown to have an effect on the magnitudes and values of the SFDs.[204] A small σ would result in few neighbor particles being detected and a quick fall of SFDs to zero; on the other hand, more neighbor particles would be included with a large σ, resulting in an isotropic neighborhood and a rapid fall of SFDs to zero.[204] A value of 13 Å is used for σ for analysis on TATB. This optimal value is selected based on the near-neighbor calculation of our previous study.[112]

The dimensionality of the orthogonal set of SFDs is first reduced by using Principal Component Analysis (PCA), which converts the correlated data into a linearly independent orthogonal basis set with fewer components.[214] The reduced set of SFDs is then classified into groups with the Gaussian Mixture Model (GMM), which is an

unsupervised machine learning classification algorithm.[215] The automated detection of defect structures using GMM, as implemented in Scikit-learn,[216] worked well on metals with higher symmetry class.[204] The underlying distribution of the data is assumed to be a mixture of n Gaussians, where n is a parameter defined by the user. Between $m = 3$ to $m = 6$, the best classification scheme that gives the cleanest classification of defect structures in the system is given by $m = 5$ for MD shock simulations of TATB crystals for $\theta = 90°$.

3.3.2 Molecular dynamics simulation details

Simulation cells for shock propagate exactly parallel ($\theta \equiv 90°$) to the normal of the molecular layer surface in the TATB crystal structure was constructed using the GCCM.[70] The angle θ is defined as the angle between the lattice vector **a** and the shock direction **S**, which is constrained to remain in the **a**-**b** plane ($\mathbf{N}_{001} = \mathbf{a} \times \mathbf{b}$) defined by the crystallographic lattices. A *generalized unit cell* was selected with the conditions that it is approximately orthorhombic and the face normal of the simulation cell is parallel to **S**. The cell was rotated so that **S** is always parallel to $+z$ in the Cartesian frame. The *generalized unit cell* is then replicated in three-dimensional space to yield simulation cells with desired dimensions. Two different systems were considered. One consists of a TATB single crystal with no pre-existing defects. This system has dimensions of $\approx$ 10 nm in the transverse directions and $\approx$ 100 nm in the longitudinal (shock) direction. A 5.0 nm vacuum region is introduced along z at one end of the simulation cell to reduce the long-range electrostatic interactions across the periodic boundary. For the other system, a 50.0 nm diameter cylindrical pore is positioned in the center of a quasi-2D simulation cell with dimensions of approximately 150 nm $\times$ 150 nm and $\approx$3.5 nm in the third (thin) direction. A 10.0 nm vacuum region is

introduced along z at one end of the simulation cell for the same reason mentioned earlier in this paragraph. (The first simulation is the $\theta \equiv 90^\circ$ case described in Refs. 116 and 112. The second simulation is the $\theta \equiv 90^\circ$ described in Refs. 84 and Chapter 2.) The two systems contain 105,792 and 328,076 molecules, respectively. All simulations were performed using the LAMMPS code[77,78] along with the all-atom fully-flexible non-reactive force field of TATB introduced in Chapter 1.

Isochoric-isothermal (NVT) and isochoric-isoenergetic (NVE) trajectories were integrated using the velocity Verlet algorithm.[74] Both systems were equilibrated at $T = 300$ K with NVE dynamics followed by NVT dynamics. Specific parameters used for the single-crystal system can be found in Refs. 116 and 112, and detailed descriptions of the quasi-2D simulation setup are included in the method section of Chapter 2 and Ref. 84. Shocks were generated using a reverse-ballistic configuration for both simulations. A 20 Å thick piston is defined at the "bottom" ($z = 0$) of the cell, and velocities of molecules within the piston are set to and maintained at zero during the simulations. A particle velocity $\mathbf{u}_\mathrm{p} = (0, 0, -1.0 \text{ km s}^{-1})$ is added to the thermal velocities of atoms in the flexible sample. This results in a supported shock wave that travels with velocity $\mathbf{u}_\mathrm{w} = |\mathbf{u}_\mathrm{s}| + |\mathbf{u}_\mathrm{p}|$ along the $+z$ direction in the frame of the stationary piston.

Two orientation parameters (vectors) were calculated for all molecules in the system at a given instant. The first parameter was computed, for a given molecule, as the vector from molecular COM position to a carbon atom of the same molecular such that the vector is approximately parallel or antiparallel (due to centrosymmetry) to the lab-frame basis vector $\hat{Y}$. The second parameter was simply the TATB benzene-ring normal vector, which is parallel to the lab-frame basis vector $\hat{Z}$ for the $\theta \equiv 90^\circ$ case.

3.4 Results and Discussion

3.4.1 Application to shock-compressed oriented TATB single crystals

The SFDs of the shock simulations were computed using the molecular COM positions and the orientation parameters. Only the SFDs that describe the size and shape of the local particle environment (19 descriptors per molecule) were used here. Training and prediction were performed using the first 9 principal components of the SFDs, which cover 99.5% of the data. The GMM classifier was trained using snapshots at three instants from the MD simulations of shock-compressed oriented TATB single crystal, at the beginning of the shock simulation ($t = 0$), at the instant of maximum compression ($t_{max} = 20$ ps), and when the shock wave was halfway through the sample ($t_{half} = 10$ ps), to obtain approximately equal numbers of molecules located behind and ahead of the shock wave. This yielded ≈125,000 molecules in total as the training data. The parameters of the five Gaussian classes were estimated using the expectation-maximization algorithm.[215] The probability of a given molecule belonging to each Gaussian was determined, and molecules were assigned to the most probable class.

The resulting five classes are shown in Figure 3.1. Two (shown in navy and green) of the five classes are identified as 'uncompressed' TATB molecules with basal plane sliding. Note the system of TATB single crystals is at thermal equilibrium ($T = 300$ K) before the shock simulation, and it is known to be prone to basal plane sliding under standard ambient conditions.[38] As the shock passes through the material, some of the 'uncompressed' molecules (shown in navy and green) become compressed and are classified as two new groups (shown in cyan and yellow, respectively) while the rest becomes 'disordered' (shown in red). This process is better demonstrated in the

animation (available in Appendix VI). All images and animations are rendered using the visualization tool OVITO.[217]

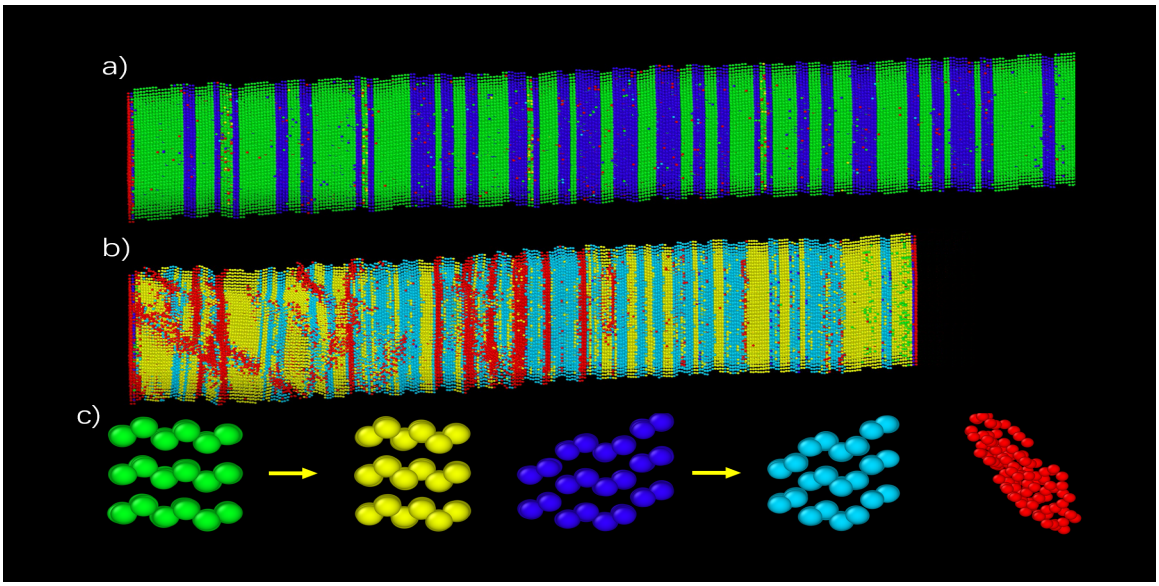

Figure 3.1: Snapshots of the shock simulation of TATB single crystal for $\theta = 90°$ at a) $t = 0$ and b) $t = t_{max}$ showing only the molecular COM positions. c) Molecules are colored according to the five Gaussian classes: 'Uncompressed' TATB molecules are shown in navy and green, 'compressed' molecules are shown in cyan and yellow, and 'disordered' TATB molecules are shown in red.

We recognize that the raw classification is not perfect. In Figures 3.1(a) and (b), molecules within the piston are shown in red, which is categorized as 'disordered' molecules. In fact, the Gaussian classification is defined based on the status of the majority of the molecules within that class. The local configuration of molecules within the piston is distinct from molecules that belong to the other four classes and thus is classified as 'disordered'. A value of $m = 6$ is considered for the GMM, but it does not separate molecules within the piston from the disordered molecules. In addition, note that there are a few 'disordered' molecules scattered across the sample at $t = 0$ (Figure 3.1(a)). This may be due to the thermal noise.

In our previous study of the thermo-mechanical response of the shock-compressed oriented TATB single crystals, deformation mechanisms of the crystals are inves-

tigated by monitoring the near-neighbor relative displacement maps (NNRDs) of molecules in the flexible sample.[112] It is defined as the difference in molecular COM position vectors in the Cartesian frame for selected molecular pairs behind the shock and the position vectors for the same molecular pairs in the perfect crystal. This method was first introduced by Zimmerman[218] and has been applied in studies of α-HMX[219] and PETN-I.[55] As shown in Figures 3.2(a) and (b), there are 14 near-neighbor molecules for each TATB molecule, including 6 in-plane and 8 out-of-plane neighbor molecules. Figure 3.2(c) contains three snapshots of a subgroup of the sample prior to the shock arrival (left), shortly after shock passage (middle), and close to the time of maximum compression (right); where the shock wave propagates vertically upward. The molecule with the largest NNRD in the sample and its 5^{th}-generation of cluster are selected. (See Refs. 116 and 112 for more details.) The deformation mechanism shown in Figure 3.2(c) corresponds to a stacking fault (middle image) followed by a non-basal dislocation (right-hand image). Interested readers are referred to Ref. 112 and 116 for more details of the analysis.

Figure 3.2 shows the dominant deformation observed for the $\theta = 90^\circ$ case. However, the deformations at larger scales are much more complex compared to the "local" results of Figure 3.2(c). Figure 3.3 contains snapshots of the entire system at the time of maximum compression analyzed using the Strain Functional analysis (SF, panel (a)) and the NNRD analysis (panel (b)). Figure 3.3(a) is identical to Figure 3.1(b)). Molecules near the piston and the free surface were excluded in the NNRD analysis (panel (b)). Molecules in the NNRD analysis were colored according to the magnitude of the largest NNRD among the 14 near-neighbor molecules. To focus on regions with significant changes, only molecules with maximum NNRD greater than a threshold value (3 Å) are presented.

As shown in Figure 3.3, results using the two methods are in good agreement

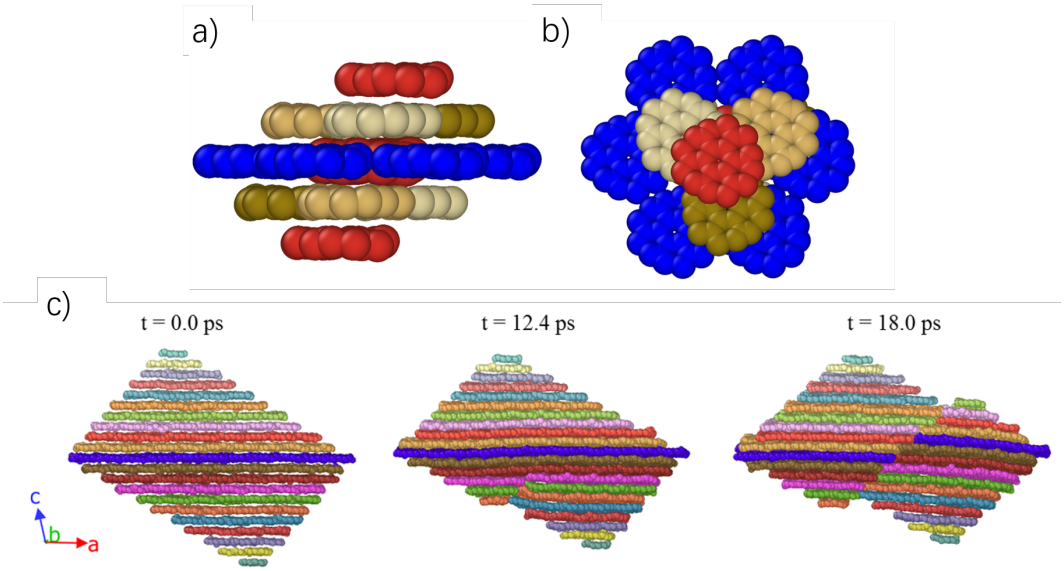

Figure 3.2: a) Top view and b) side view of a central TATB molecule (large red) with its six in-plane (navy) and eight out-of-plane (shades of brown and red) near-neighbor molecules. c) Snapshots of a selected molecule and its 670 near-neighbor molecules at time t for $\theta = 90°$ case. Molecular layers are colored according to distances away from the central molecular layer. The crystal lattice frame corresponding to the snapshots is shown on the lower left.

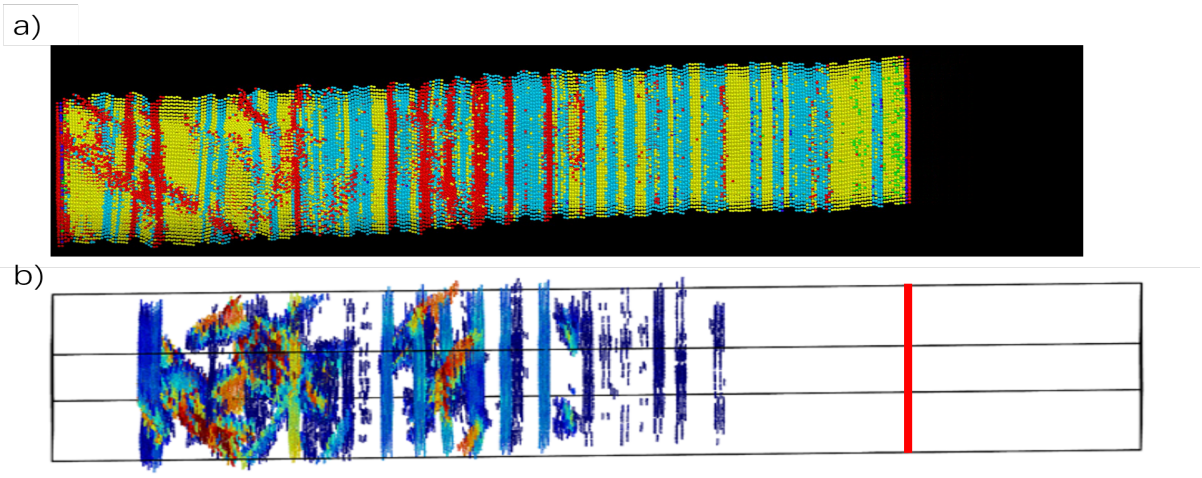

Figure 3.3: Snapshots of the system at the time of maximum compression for $\theta = 90°$ analyzed using a) Strain Functional analysis and b) NNRD analysis. The red line in b) indicates the position of the free surface at that instant. Molecules close to the piston and the free surface are excluded from the NNRD calculation.

qualitatively: molecules with NNRD values above the threshold shown in panel (b) are classified as 'disordered' by the GMM (shown in red in panel (a)). However, the two types of compressed molecules that are shown in cyan and yellow using the SFDs (panel (a)) are not distinguished by the NNRD analysis due to their small NNRD values. While the NNRD analysis is useful in determining deformations associated with large molecular displacements, it fails to provide information about the specific deformation mechanism. As a result, it becomes difficult to distinguish among molecular displacements due to thermal fluctuations; deformations with small NNRD such as basal-plane layer sliding, twinning, and buckling; and deformations with large NNRD such as shearing and dislocations. In part, this is because the NNRD threshold values are arbitrary. Prior knowledge about the ranges of NNRD values that correspond to different kinds of deformation is required to properly interpret the results. Whereas the NNRD analysis only focuses on defined near-neighbor molecule displacements, the SF analysis takes the entire local neighborhood into consideration, including information on both number density and geometry of the environment. When an unsupervised machine learning method, the GMM, is applied to the set of SFDs, the result is a more comprehensive and interpretable classification of the molecules. Compared with the NNRD analysis, the SF analysis allows classification without *a priori* knowledge of the initial structure of the neighbor environment and can be readily applied to materials with any symmetry class.

3.4.2 Application to shock-induced pore collapse in oriented TATB

To further test the SF analysis, we apply it to results of shock-induced pore collapse in oriented TATB crystals. The GMM is trained using the data from the shock simulations of the 90°-oriented crystal as discussed in Section 3.4.1, and the same

classification with five classes has been applied here. In both cases, the crystal orientation is for shock propagating parallel to the surface-normal vector of the molecular layers. Snapshots of the system prior to the shock (panel (a)) and at the time of maximum compression (panel (b)) are shown in Figure 3.4. Molecules near the free surfaces (both ends of the simulation cell and at the pore surface) are identified as 'disordered' molecules. The system is at thermal equilibrium ($T = 300$ K) before the initiation of shock, and the basal plane sliding mentioned earlier and in Ref. 38 is likely the cause of the two distinct groups (shown in navy and green). After shock wave passage, molecules behind the shock front are classified into three groups: 'compressed' molecules (shown in cyan and yellow) and 'disordered' molecules (shown in red). Figure 3.4(b) is a depiction of the system at the time of maximum compression. The pore has completely collapsed, and the shock wave generated with the closure of the pore has reached the upper end of the simulation cell. The shock front, which has a curved shape, is clearly shown as the boundary between the 'compressed (cyan and yellow)' and 'uncompressed (navy and green)' molecules.

The shock wave profile is rather complex and is better viewed in conjunction with the animation in Appendix VI. The shock wave initially propagates vertically up and becomes bend around the curved pore surface. Waves on either side of the pore travel at a greater speed than in the center of the simulation cell, forming a shock wave front with a 'v-shape'. Reflected waves are generated from the top surface when the shock waves on either side of the pore reach that end of the simulation cell, leading to a rarefaction that propagates back into what was originally compressed material on the downstream side of the pore, causing it to relax. Meanwhile, the pore collapses and sends out a blasting wave that propagates outward away from the pore. The blasting wave meets and overtakes the reflected waves half-way above the equator. The snapshot shown in Figure 3.4(b) is captured at the instant of the blasting wave

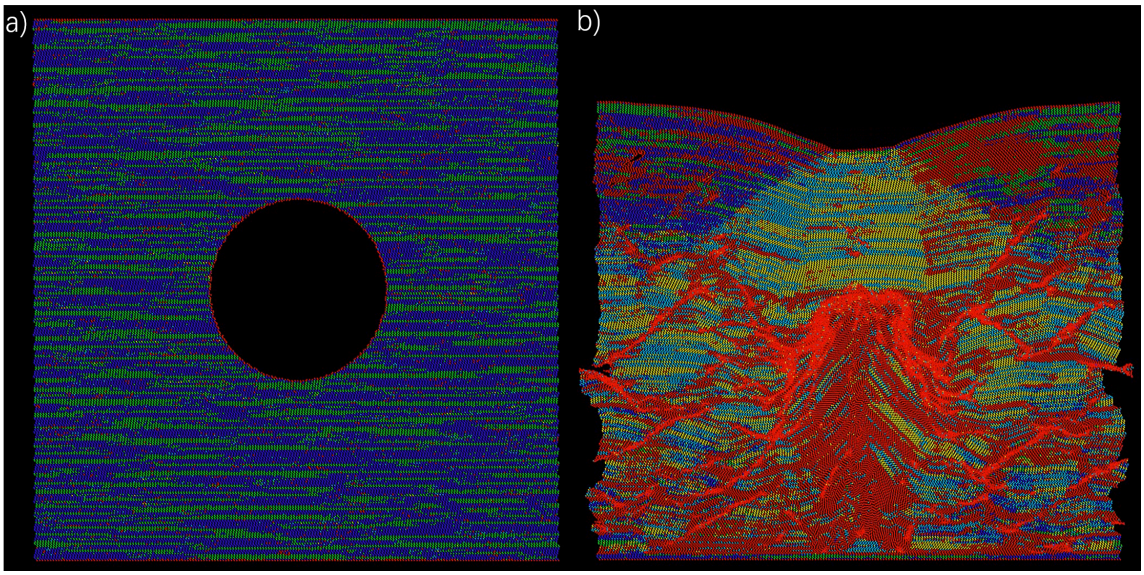

Figure 3.4: States of the system during shock-induced pore collapse in TATB crystals with an orientation of $\theta = 90°$ at a) $t = 0$ and b) $t = t_{max}$. Here, t_{max} is the instant when the shock wave generated by pore collapse has just reached the top end of the simulation cell. Molecular COM positions are rendered using the unwrapped coordinates in the lab frame. The color scheme is the same as in Figure 3.1.

that is generated by the pore closure has reached the top end of the simulation cell.

The 'disordered' molecules can be, intuitively, divided mainly into two categories: 'disordering' due to pore collapse and 'disordering' due to dislocations. Molecules belonging to the first category are concentrated between the piston and upstream of the original pore (bright red region in Figure 3.4(b)), and this 'disordering' is mainly caused by the collapse of the pore. The later type of 'disordered' molecules, which are further away from the location of pore closure and have a pattern that is reminiscent of tree branches, are probably results of propagation of dislocations across multiple molecular layers. Note 'disordered' molecules in the unloading regions (red regions in the upper corners in Figure 3.4(b)) are unlikely to fall into either of the categories mentioned above. It is difficult to categorize the 'disordered' molecules near the location of pore closure; various numbers of classifications of the GMM have been tested with limited improvement of the results.

3.5 Conclusions

The Strain Functional Descriptors (SFDs) developed by Mathew *et al.*[204] is a set of formally complete and rotationally invariant descriptors that can be used to characterize particle geometries from MD simulations. Discrete quantities associated with the particles (here, molecular COMs) such as number density are mapped onto continuous fields using a Gaussian kernel. Local particle configurations are derived from n^{th} order central moments of the local number density. Initial moments in Cartesian coordinates are transformed into the Solid Harmonics polynomial basis using SO(3) decompositions. The rotationally invariant SFDs are constructed through the Clebsch-Gordan coupling. These descriptors characterize the particle environment in terms of size, shape, and orientation of the neighborhood and can be used to identify crystal symmetries, defect structures, and phase transformations. With the application of unsupervised machine learning algorithms, the SFDs can be used as an automated tool for analysis of deformation mechanisms and defect structures in MD simulations.[204]

In this work, an existing SF analysis code was modified to incorporate periodic boundary conditions and enable it to handle triclinic (non-orthogonal) simulation boxes. We have demonstrated its ability to successfully characterize and predict deformations and defects in both uncompressed and shock-compressed samples of the triclinic molecular crystal TATB. Classifications results from the unsupervised learning algorithm GMM have shone light on the mechanical shock response of the crystal and provided data for further analyses of deformation mechanisms. Unlike many of the structural analysis methods that are limited to high-symmetry crystals, the SFDs can be applied to materials with any symmetry class.

We notice that random noise exists in both simulations considered in this study.

Several measures can be taken to improve on this. The GMM is trained using results from the MD simulations at three time instants. The random noise in classification might be reduced by training the GMM with time-averaged MD results. In addition, we note that only the size and shape descriptors were included in the PCA performed in this study. While this may be sufficient for systems with high symmetry, a more inclusive set of descriptors which also includes orientation perhaps will yield better classifications, especially for materials with lower symmetries. With the GMM, the distribution of the principal components is assumed to be Gaussian. Application of other machine learning algorithms such as (unsupervised) k-means clustering[220,221] or (supervised) K-Nearest Neighbor (KNN)[222] may provide insight on choosing the best clustering algorithm for low-symmetry crystal system. The SF analysis can also be applied to systems of TATB crystals with other orientations, and further studies to interpret the classification are much needed.

3.6 Acknowledgments

This work was performed under the auspices of the ASC PEM HE Mesoscale Project (Advanced Simulation and Computing Program, Physics and Engineering Models, High Explosives Mesoscale Project) from the Los Alamos National Laboratory (LANL). The work on the MD simulations were supported by grant numbers FA-9550-16-1-0437 and FA9550-14-1-0360 from the U.S. Air Force Office of Scientific Research (AFOSR) within the Dynamic Materials and Interactions (DMI) portfolio (program officer: Dr. Jennifer Jordan and Dr. Martin J. Schmidt). The MD simulations were enabled by a special grant of 500,000 high-priority core-hours on the "Lewis" high-performance institutional computing infrastructure provided by Research Computing Support Services at the University of Missouri-Columbia. The Lewis cluster is partially supported

by a grant from the National Science Foundation under grant number CNS-1429294. The author acknowledges Dr. Edward Kober for the internship opportunity at LANL, and Dr. Nithin Mathew and Dr. Edward Kober for fruitful discussions.

Chapter 4

Lessons Learned and Helpful Tips

4.1 Introduction

As a young graduate student who knew little about the topic of theoretical chemistry, let alone molecular dynamics simulations, I was lost for quite some time. It took me a very long time before I began to gain any understanding of the complex theories of molecular dynamics and the complicated programming commands of LAMMPS. What I did not know was that obtaining an understanding of these concepts was only the bare minimum to perform an MD simulation correctly. There are myriad ways to fail, and each of them is unique. While some of the mistakes are easy to catch and fix, some are easy to miss, especially for beginners.

Mistakes are inevitable during any learning process. In fact, it is one of the necessary components of the human learning process. Though usually not reported in the literature, many mistakes are valuable learning sources for forthcoming graduate students. Whereas students may learn better when they make these mistakes themselves, similar (learning) experiences (through failures) can be obtained by reading

about others'. Here, I include a few lessons that I have learned during my professional life, hoping these can be of a little help for anyone who is reading this.

4.2 Buck/coul/long never ends

I still remember that when I first started my graduate study, my advisor had warned me repeatedly that I must understand every single command line before I started run any simulations, and I must admit that I did not at the beginning. Being a student with no prior experiences in programming or running MD simulations, learning to drive a complex program such as LAMMPS was difficult enough for me. As I became more familiar with LAMMPS and started to gain a better understanding of the program and the command lines, I started to realize the difficulties in performing a simulation with the correct setup and parameters. Some of the mistakes I made could probably have been prevented if I had understood the exact meaning of each command line specified in simulations.

The example that strikes me the most is the effect of the non-bonded long-range interaction terms of the force field on the angular momentum of the system. The objectives of the project were to understand the concept of normal-mode analysis, learn and implement it, and become familiar with performing MD simulations using LAMMPS. The system contained a single molecule of a hexahydro-1,3,5-trinitro-1,3,5-s-triazine (RDX) bonded with a phenyl group, which is referred to as phenyl-RDX for the rest of this chapter. The chemical structure of the phenyl-RDX molecule is shown in Figure 4.1. The goal was to simulate the dynamics of an isolated molecule. The simulation box had a cubic shape with an edge length of 120 Å, and the phenyl-RDX molecule was placed at the origin of the simulation cell; that is, with the molecular COM position located at (0, 0, 0). To conduct the normal-mode analysis, a 60 ps

NVT dynamics was first performed at a final temperature of 298 K, followed by a 100 ps long NVE dynamics equilibration. The initial kinetic energies were randomly selected from a Maxwell (Gaussian) distribution and adjusted to yield zero net linear and angular momentum. The total energy, linear momentum, and angular momentum of the system were calculated and monitored during the simulations. Conservations of fundamental classical mechanical quantities needed to be confirmed before performing any analyses.

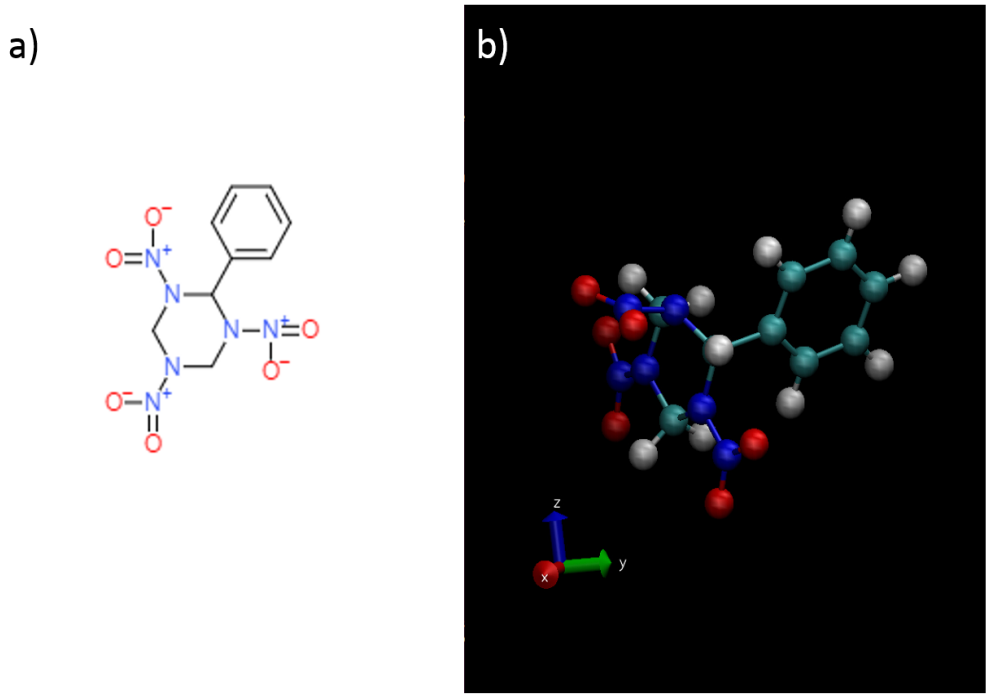

Figure 4.1: a) 2D and b) 3D diagrams of the phenyl-RDX molecule. The benzene and the RDX molecules are connected *via* a C-C single bond. Carbon atoms are shown in cyan, hydrogen atoms are shown in white, oxygen atoms are shown in red, and nitrogen atoms are shown in navy.

During the NVT and NVE dynamics, the phenyl-RDX molecule was found to start rotating (gain angular momentum) shortly after the beginning of the simulation. The

calculated angular momentum of the system initially started at zero and increased steadily for the rest of the simulation, despite the fact that it was defined to be zero at the beginning of the simulation and should have remained at zero throughout the entire simulation because it is a constant of the motion for an isolated system. The cause of this (surprising) result was investigated and was found to be a single command line in the LAMMPS input script. Among the multiple command lines which define the force field of this molecule, one of them describes the non-bonded long-range interaction calculations. This command line and its corresponding evaluation method are circled in Figure 4.2. The Buckingham and Coulombic potential terms defined in the 'buck/coul/long' *pair_style* have the following form

$$E = Ae^{-r/\rho} - \frac{C}{r^6} \tag{4.1}$$

$$E = \frac{Cq_iq_j}{\epsilon r} \tag{4.2}$$

where r stands for the effective interatomic distance for the potential calculations, q is the ionic charge of atoms, and ρ, ϵ, A, and C are parameters. Here, $r < r_c$, and the cutoff distance r_c is set to be 40.0 Å for both the Buckingham and Coulombic potential terms (shown as the two numbers after the 'buck/coul/long' command line).

Intuitively, with a cutoff radius that is less than half of the simulation box edge length, the long-range non-bonded interactions should *not* introduce any artificial effects. *However*, the option 'long' means that no hard cutoff is applied for the Buckingham or the Coulombic potential energy calculations. Instead, r_c denotes the distance which long-range interactions calculated in real space within the cutoff radius are replaced by calculation in reciprocal space (*i.e.*, K-space). With the periodic boundary conditions in conjunction with *long*, the original phenyl-RDX molecule is

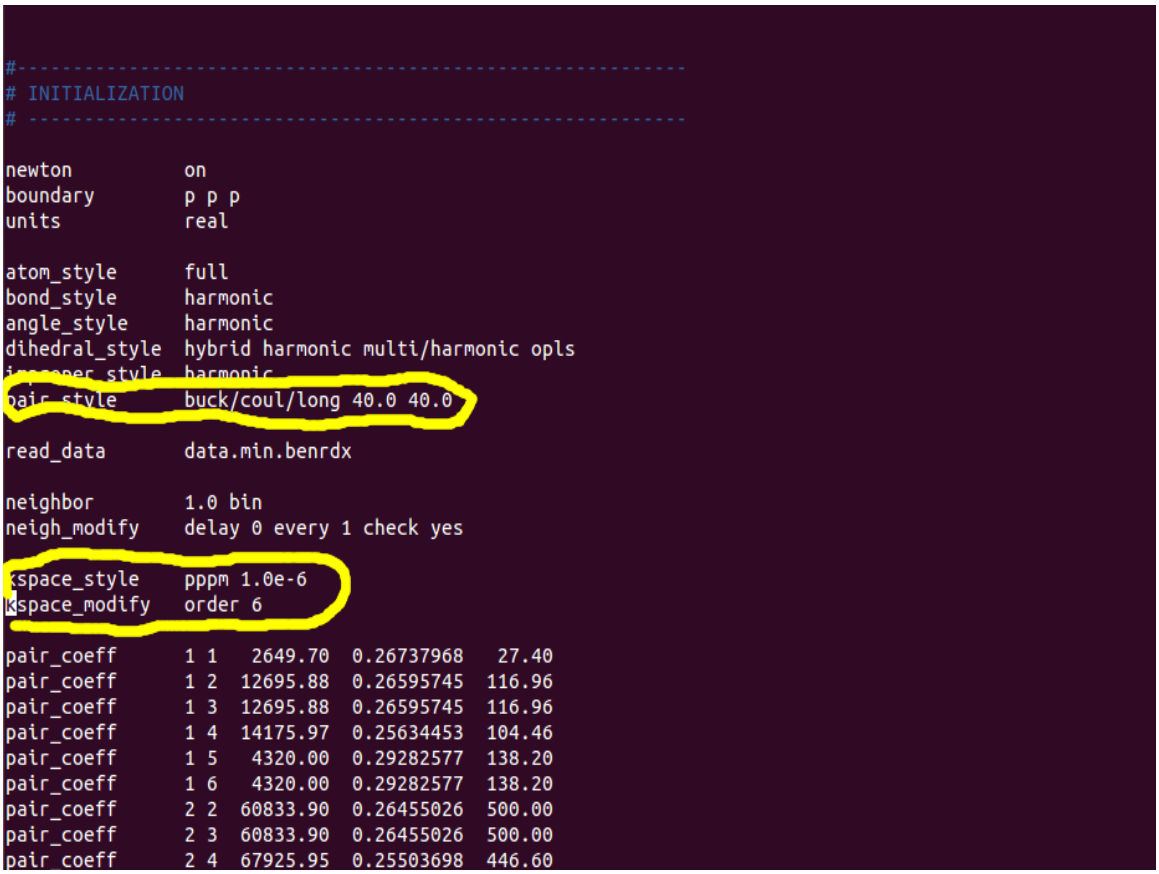

Figure 4.2: Snapshot of part of the input script for NVT and NVE dynamics performed using LAMMPS. Command lines relevant to non-bonded long-range interaction calculations are circled.

interacting slightly with its periodic images, resulting in weak forces that cause the rotational acceleration of the molecule.

The solution to this problem was straightforward. The angular-momentum problem was removed by switching from the evaluation option 'long' to 'cut', indicating a hard cutoff is applied for the potential energy and force calculations. In Figure 4.3, the angular momentum of the system calculated with a hard cutoff for the long-range interactions remains at zero throughout both the NVT and NVE dynamics.

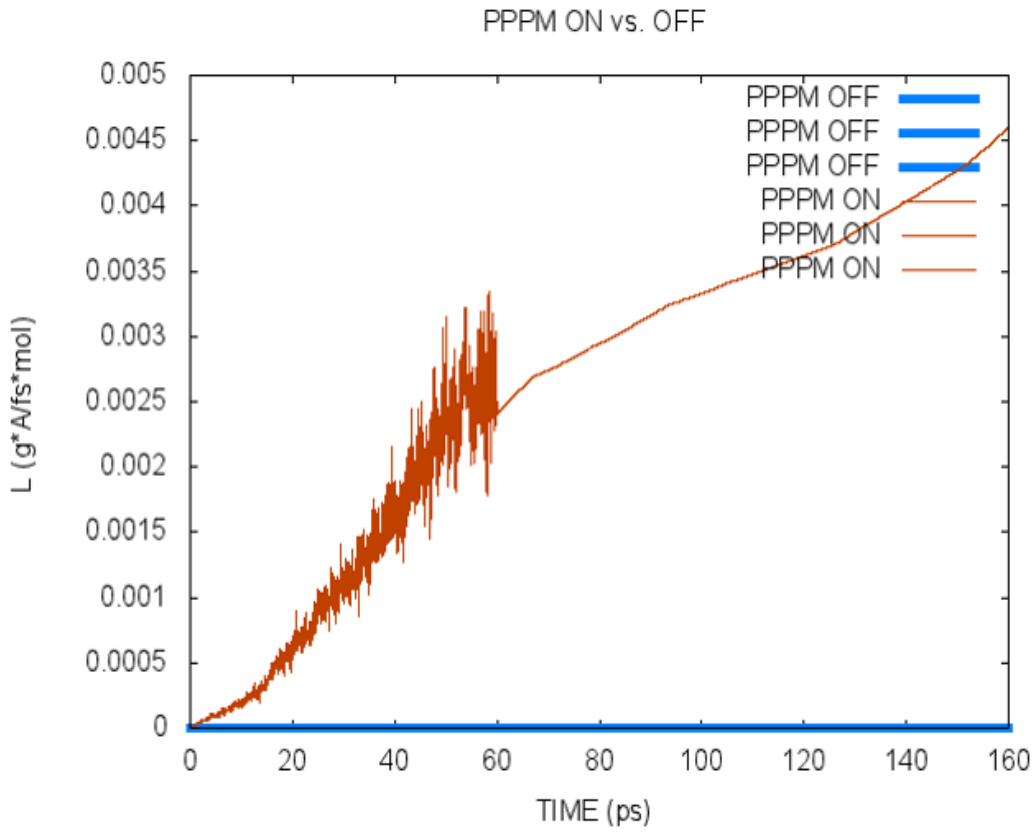

Figure 4.3: Angular momentum $|L|$ of the system evaluated with (denoted as 'PPPM OFF') and without (denoted as 'PPPM ON') a hard cutoff. The increasing $|L|$ of the system with infinite long-range interactions is shown in orange, and $|L|$ of the system with a hard cutoff of the long-range interactions is shown in blue. Note that for the case without a hard cutoff (orange), the noisy portion is due to NVT dynamics, and the smooth (but increasing) portion is for NVE dynamics.

This simple example has clearly illustrated the effect of long-range interactions on the system properties calculations. It has also demonstrated the importance of a complete understanding of the simulation setup. As shown in the previous paragraphs, the meaning of the cutoff radius r_c can change with the calculation options, and a change in a calculation option could eventually lead to possible failure of the simulation. The importance of a complete understanding of the simulation setup details cannot be stressed enough. To perform an MD simulation correctly, one has to be extremely careful with the simulation design as well as the setup details.

4.3 In shock simulations the thickness of the piston matters

One tricky aspect of running MD simulations is that successfully running the simulations without "segmentation faults" does not guarantee the correctness of the results. This is similar to computer programming: A code that "runs" is not guaranteed to yield results. A comprehensive understanding of the simulation setup and careful selections of parameters are keys to a successful and accurate simulation. In addition to a complete understanding of the simulation setup, details of simulation design also play an essential role in performing a valid, high-quality simulation. Here, we present a (failed) case study of MD shock simulations of TATB single crystals with a very thin piston as an example to demonstrate the importance of simulation design details.

In my MD shock simulations, a small region of the sample material is often defined as the rigid piston for the generation of shock waves in the system. In a reverse-ballistic configuration, the flexible sample impacts the piston and a shock wave that propagates through the flexible sample is generated. In a piston-driven configuration, the rigid piston (in which the molecules are completely frozen) compresses the flexible

sample at a constant velocity. In both cases, the thickness of the piston is an important element of simulation design. If the piston is too thick, then less data (sample material) is available for post analyses; if the piston is too thin, then material will pass through the rigid piston upon impact. Therefore, the optimal thickness of the piston should be the minimum width that is able to prevent molecules from passing through. In MD shock simulations of molecular crystals, many factors, such as the crystal orientations, molecular geometry, unit cell lengths, and impact speeds, need to be considered when determining the piston thickness. In general, a piston commonly has the thickness that equals to a couple of unit cell lengths, approximately 20 Å to 30 Å.

Figure 4.4 shows three MD shock simulations of oriented TATB single crystals using a reverse-ballistic configuration with a piston thickness of 10 Å. In this (failed) study, seven crystal orientations, ranging from 0° to 90° with increments of 15°, are considered. Simulation details for this study can be found in Refs. 112 and 116. (The piston thickness is changed to 20 Å in Refs. 112 and 116 while keeping other procedures the same.) Shortly after the simulation started, molecules from the flexible sample that are in contact with the piston are pressed strongly against it and some are pushed through the "empty spaces" in the rigid piston (regions of lower atomic density), resulting in individual TATB molecules "flying" into the vacuum region at the other end of the simulation cell due to the periodic boundary conditions. Results have indicated that a 10 Å thick piston is sufficient for shock simulations of crystal orientations $\theta \geq 60°$ (not shown here), while for $\theta < 60°$, molecules are extruded through the piston.

Questions may be raised such as "Have you not used one orientation as the study case for such a thin piston before applying it to other orientations?" As a matter of fact, the shock simulation of $\theta = 90°$ was used as a test case for such piston thickness,

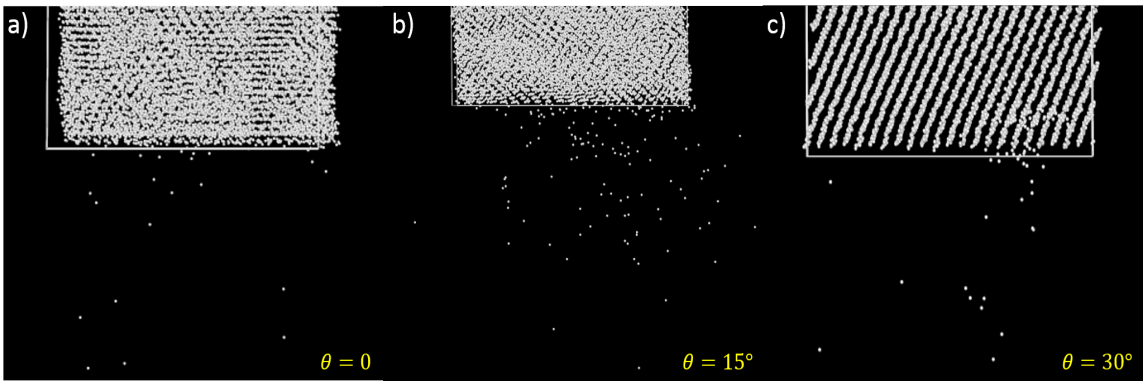

Figure 4.4: Extrusion of TATB molecules due to the extremely thin piston for a) $\theta = 0$, b) $\theta = 15°$, and c) $\theta = 30°$. Molecules are represented as particles using the molecular COM positions.

and in this case 10 Å worked well. Unfortunately, this was only true for orientations with large values of θ. As a young graduate student, I was naive to think that if it can be applied to one case, it can be applied to all. As demonstrated using the case study, simulation details play a crucial role in performing the correct simulations correctly. There are infinite ways to introduce mistakes in a simulation. Although many of them could possibly be avoided based on previous experiences, some of them are difficult to detect especially for inexperienced graduate students. Details make a huge difference in terms of correctness and performance of the simulations.

4.4 Optimal choice of the summation method

In computer programming, the utmost important thing is to verify and validate a code, ensuring the correctness of both the code itself and its results. The next step is to improve its efficiency. Earlier in this chapter, we have discussed two key aspects of performing a *correct* MD simulation *correctly*. We shall now shift our focus to the efficiency improvement on MD simulations.

The massively parallel computer program LAMMPS offers a variety of options for

a simulation. As seen in the first example, several computing methods, each with multiple options, are available for a single MD simulation. Those options can have an effect on the correctness and the performance of the simulations. The user needs to select the options that are most appropriate for their simulation.

The effect of the different computing options on the efficiency of a simulation sometimes can be very intuitive. Using the calculation of Coulombic interactions as an example, it is obvious that a longer cutoff radius, which means more computations, will take a longer wall time to complete. Sometimes such effect on efficiency cannot be easily predicted without tests and comparisons. Here, we present a case study of the effects of the summation methods on both the efficiency and the accuracy of the potential energy and force calculations in a MD simulation.

There are three independent variables in this study: numbers of atoms in the system, the value of cutoff radius r_c, and the summation method for long-range interactions. One of the variables is varied while keeping the others the same. Four system sizes, five cutoff radius lengths, and three summation methods are considered, yielding a total of 60 simulations. The four systems contain 10,000 atoms, 100,000 atoms, 1 million atoms, and 10 million atoms, respectively. The value of the cutoff radius ranges from 11 Å to 15 Å with increments of 1 Å. And the three summation methods applied are the Particle-Particle Particle-Mesh (PPPM) solver,[223] the Wolf summation method,[166] and the Damped Shifted Force (DSF) method.[224] The equation for the pairwise Coulombic energy is shown in Eq. 4.2. In the PPPM solver, the atomic charges are first mapped onto a 3D mesh, the electric fields are evaluated using a 3D fast Fourier transform (FFT), and charges are interpolated on the mesh and mapped back onto the atoms. The evaluation method proposed by Wolf *et al.* has the following form

$$E_i = \frac{1}{2}\sum_{j\neq i}\frac{q_i q_j erfc(\alpha r_{ij})}{r_{ij}} + \frac{1}{2}\sum_{j\neq i}\frac{q_i q_j erf(\alpha r_{ij})}{r_{ij}} \tag{4.3}$$

where the pairwise Coulombic energy is damped *via* the complementary error function. This method uses a charge-neutralized sphere when evaluating the potential energy, and the cutoff radius r_c is defined by the user. The DSF method is an extension of the Wolf summation and aims at resolving the issue of force discontinuity at the cutoff radius. An additional force term, which is derived from the standard shifted potential, is incorporated into the potential energy equation proposed by Wolf *et al.*

$$E_i = q_i q_j [\frac{erfc(\alpha r_{ij})}{r_{ij}} - \frac{erfc(\alpha r_c)}{r_c} + (\frac{erfc(\alpha r_c)}{r_c^2} + \frac{2\alpha}{\sqrt{\pi}}\frac{exp(-\alpha^2 r_c^2)}{r_c})(r_{ij} - r_c)] \tag{4.4}$$

An energy-drift issue in the Wolf method has been improved by including the shifted force term in the DSF method.

Note the option 'coul/long' is applied in conjunction with the PPPM solver, and the cutoff radius indicates in which subspace (real or reciprocal) the energy calculation is carried out. In each simulation, 200 steps of NVT dynamics at 300 K was performed with the initial atomic velocities selected from a Maxwell (Gaussian) distribution. The accuracy (of potential energy and force calculations) and efficiency (the wall time) of the simulations are examined across all simulations to identify the optimal choice of summation method and parameters that yields the most accurate results with the highest efficiency. Here, all simulations were performed on systems of perfect β-HMX crystal, which is monoclinic with two molecules per unit cell. Simulation cells were generated as replications of β-HMX unit cell under standard ambient condition, of which the lattice parameters were predicted using the force field developed by Smith

and Bharadwaj[225,226] and later refined by Kroonblawd *et al.*[70]

First, we examine the effect of cutoff radius on the accuracy of potential energy and forces calculations. Simulations of a given size were performed starting from identical initial atomic configurations. The potential energy and forces were evaluated for the same atomic configurations using various cutoff radius and summation methods of a given simulation cell size. The results computed using the PPPM solver are treated as "ground truth" for this comparison. The shortest cutoff radius r_c that gives the best accuracy is selected for further analyses in order to obtain that accuracy with the highest efficiency. The effects of the simulation size and the summation method on computing efficiency are studied to provide a base for determining the optimal r_c value for different simulation sizes and summation methods.

The accuracy of potential-energy calculations was evaluated using the percentage difference between the values computed using either the Wolf or DSF method and the values computed using the PPPM solver. The cutoff radius exhibits minimal effect on the potential-energy calculations. The percentage difference of potential energy calculated using the Wolf method increases from 0.003% to 0.05% with an increasing cutoff radius regardless of the system size. Although the relative increase of the percentage difference is almost a factor of 20, the absolute change of the percentage difference is negligible. For practical purposes, the potential energy differences between the Wolf summation method and the PPPM solver can be treated as zero. On the other hand, the percentage difference of potential energy calculated using the DSF method shows a large deviation, ranging from 0.04% to -8.67%. This range is mainly due to variation in simulation sizes, and the effect of cutoff radius is negligible. (For system sizes smaller than 10 million atoms, the percentage difference in potential energy between DSF and PPPM is approximately -8.7% regardless of the cutoff radius; for the system containing 10 million atoms, the percentage difference ranges from 0.04% to

0.08% with no obvious correlation with the cutoff radius.) The percentage difference in calculated forces was evaluated for the three Cartesian components individually using the following equation

$$\%difference = \frac{F_i^{DSF} - F_i^{PPPM}}{|\mathbf{F^{PPPM}}|} \times 100\% \tag{4.5}$$

where *i, j, k* are the Cartesian force components. For forces computed using the Wolf method, the percentage differences are in the hundredths decimal place. The maximum percentage difference in forces calculation using the DSF method is around 2% in magnitude. In conclusion, the simulation size has a large impact on the percentage differences in the potential-energy and force calculations, and the effect of the cutoff radius is minimal for a given simulation size. Because the computational efficiency decreases as the cutoff radius increases, a cutoff radius of 11 Å is selected as the optimal value for future MD simulations.

The computational efficiency of the four simulation sizes using three summation methods is evaluated with a cutoff radius of 11 Å only. It is computed as the percentage difference of wall-clock time between the DSF or Wolf method and the PPPM solver. The same number of computing cores were used for a given simulation size. The wall time for running 200 steps of NVT dynamics is shown in Table 4.1.

The computational efficiency increases by 4% to 25% (with an increasing system size) compared with the PPPM solver when using the DSF method, and it decreases by 70% to 120% (with an decreasing system size) when using the Wolf summation method. (The lower efficiency of the Wolf method was not expected based on its high efficiency compared to PPPM method for systems of TATB crystals (Appendix III) discussed in Chapter 2. This might be due to the large skewness of simulation cells of β-HMX crystals, whereas simulation cells of TATB crystals were approximately

Table 4.1: Wall-clock time for running 200 steps of NVT dynamics at 300 K with various summation methods and system sizes.

Method	Number of Atoms	Wall Time (s)
PPPM	10,000	2.41
DSF	10,000	2.23
Wolf	10,000	5.21
PPPM	100,000	18.63
DSF	100,000	17.82
Wolf	100,000	40.40
PPPM	1,000,000	215.28
DSF	1,000,000	193.38
Wolf	1,000,000	412.37
PPPM	10,000,000	2241.46
DSF	10,000,000	1679.05
Wolf	10,000,000	3758.98

orthorhombic.) The DSF method provides a better "efficiency", but its potential-energy and force calculations are less accurate than when using the Wolf method. We realize the potential-energy value depends on its reference state, which may explain the deviations in the potential energy calculations. However, the 2% deviation in the force calculations is less desirable.

In addition to the comparisons discussed above, the efficiency of different ways to implement the 'buck/coul/long' pairwise style is examined for the four simulation sizes. The Buckingham and Coulombic potentials can be evaluated using a single option (pairwise style 'buck/coul/long') or two separate options (pairwise style 'buck' in conjunction with 'coul/long'). The later implementation has been applied in the comparisons shown up to this point. The wall time using both implementations is shown in Table 4.2.

The computational efficiency is increased by approximately 20% regardless of the simulation size when using a single pairwise option compared to using two separate

Table 4.2: Similar to Table 4.1 but performed using various pairwise styles and simulation sizes.

Pairwise Style	Number of Atoms	Wall Time (s)
Buck, coul/long	10,000	2.41
Buck/coul/long	10,000	1.97
Buck, coul/long	100,000	18.63
Buck/coul/long	100,000	14.70
Buck, coul/long	1,000,000	215.28
Buck/coul/long	1,000,000	161.78
Buck, coul/long	10,000,000	2241.46
Buck/coul/long	10,000,000	1871.10

options. The potential energy and forces evaluated using the two implementations are identical. We conclude, based on the results discussed above, that the optimal choice for the long-range interaction evaluations in our MD simulations is the pairwise style 'buck/coul/long' with an 11 Å cutoff radius. This choice of cutoff radius and summation method will be applied in our future MD simulations.

4.5 Conclusion

Failed simulations are often as valuable for learning as "successful" ones. In this chapter, I aimed to provide a few tips for performing MD simulations that I learned from personal experiences. The key to successfully perform MD simulations involves mindful simulation design, detailed simulation planning, careful parameter selections, and a complete understanding of the simulation setup. In addition, in the last example, the accuracy and efficiency of multiple summation methods are examined over different cutoff radius distances and simulation sizes. The optimal cutoff radius and summation method were determined and will be applied in our future MD simulations.

Instead of making an exhaustive list of all the mistakes and lessons that I learned from the past, my goal was only to provide a few ideas on simulation design and setup. There is more value in making mistakes than a new student might realize, and they should be recorded and passed down to the forthcoming graduate students. By sharing some of my past experiences in running MD simulations, I want to use them as the "bricks to attract jades" (to encourage others to come forward with their valuable contributions by providing an example first). Hopefully these experiences can be helpful for future graduate students in their research.

Chapter 5

Conclusions and Future Work

In this dissertation, the anisotropic thermal and mechanical shock response of the energetic organic crystal 1,3,5-triamino-2,4,6-trinitrobenzene (TATB) is investigated using molecular dynamics (MD) simulations with a non-reactive fully-flexible force field. Due to the difficulties in synthesizing perfect TATB single crystals, fundamental experimental data for TATB single crystals is lacking. Results from MD simulations play an important role in providing insights into the physical and mechanical properties of TATB single crystals at the microscopic scale. In addition, MD simulation results also serve as the foundation for building and improving the constitutive laws used at the mesoscopic level.

The thermal and mechanical response of shock-induced pore collapse in oriented TATB crystals was studied using the classical MD simulations in Chapter 2. Three crystal orientations, bracketed by the limiting cases in which the shock wave propagates parallel and perpendicular to the molecular layers, were considered. Quasi-2D systems of different crystal orientations were constructed with a 50.0 nm diameter pore positioned in the center of the simulation cell. The shock-induced pore collapse

of TATB crystals was explored for three impact speeds, 0.5 km s^{-1}, 1.0 km s^{-1}, and 2.0 km s^{-1}, yielding collapse mechanisms ranging from visco-plastic to hydrodynamic. The results indicate that for higher impact speeds, hydrodynamic-like collapse and the formation of shear bands may be the major cause of hotspot formation; for lower impacts, the crystal anisotropy and mechanical deformations may have a significant effect on hotspot generation.

A head-to-head comparison of MD and continuum pore-collapse simulations was also conducted. While the force field used in the MD simulations accounts for the anisotropy of the crystal, the continuum model used in this study is isotropic. Results from the MD and continuum simulations were in good agreements in broad aspects such as shock waves propagations, temperature distributions, pore-collapse mechanism, and evolution of pore areas. Differences were observed in quantities that are important in the hotspot ignition and growth, including the distributions of high temperatures. These differences are believed to result from anisotropy and deformations that are present in the MD simulations only. Treating the results from the MD simulations as 'ground truth', the discrepancy between the MD and continuum simulations suggests a pressing need to incorporate crystal plasticity and anisotropy in the continuum model.

To automate the analysis of deformations of TATB crystals, the Strain Functional analysis, coupled with the machine learning techniques Principal Component Analysis and the Gaussian Mixture Model, was applied to MD simulation results of shock-compressed TATB crystals. Strain Functional Descriptors comprise an exhaustive set of rotationally invariant descriptors that can be used to characterize the local geometries. Discrete molecular quantities such as number density and orientation parameters were mapped onto continuous fields *via* a Gaussian kernel. The rotationally invariant descriptors were obtained from the n^{th} order central moments expressed

using the Solid Harmonics polynomial basis. These descriptors contain geometric meanings of the local configurations in terms of size, shape, and orientation.

In conjunction with the unsupervised machine learning algorithms, the SFD successfully identified the basal plane sliding prior to and after the passage of shock waves in TATB in addition to the dislocations and shearing in the systems without and with the presence of a pore. The classification results may be improved in several ways, such as training the ML models with time-averaged data to reduce thermal noise, including the orientation descriptors in the SF analysis as part of the training data set, using a different dimensionality reduction technique, and applying a different clustering scheme. The structure of TATB crystal belongs to the most general (lowest, triclinic) symmetry class, and thus is a good candidate for a case study of the SF analysis. With the success for TATB crystals, the SF analysis should be readily applicable to materials with any symmetry class.

In Chapter 4, a couple of lessons of running MD simulations that I have learned from past experiences were included, hoping to provide a few helpful tips for new graduate students. Mistakes in running MD simulations can often be beneficial learning experiences. To successfully perform MD simulations requires careful simulation design and planning, a comprehensive understanding of the simulation setup, and mindful parameter selections. Preliminary tests are often necessary to determine the optimal simulation parameter values and setup. Hopefully those examples can be helpful and inspiring for the readers.

Understanding the hotspot ignition and growth process requires insights from all scales, ranging from the nanoscale to the macroscale. Simulations at the mesoscale can serve as the bridge between the two extremes. Therefore, it is essential to develop constitutive laws, guided by results of MD simulations and experiments, that accurately describe the material behaviors. The triclinic crystal TATB is an ideal

candidate for model development and testing due to its low symmetry and highly anisotropic thermal and mechanical response to external perturbation. Incorporation of plasticity in the mesoscale model is much in need to account for the anisotropic material behaviors presented in simulations and experiments and leads to challenging yet interesting studies in the future.

Chapter 6

APPENDICES

6.1 Appendix I: LAMMPS Implementation of the Short-Range R^{-12} Repulsion Term into the Buckingham-plus-Coulomb Non-Bonded Potential Energy

The intermolecular non-bonded potential energy $U^{NB}(R)$ consists of the sum of two-body repulsion and dispersion terms $U^{RD}(R)$ and Coulomb electrostatic interactions $U^{coul}(R)$:

$$\begin{aligned} U^{NB}(R) &= U^{RD}(R) + U^{coul}(R) \\ &= \sum_{i>j} \left[A_{\alpha\beta} exp(-B_{\alpha\beta} R_{ij}) - C_{\alpha\beta} R_{ij}^{-6} + D(\frac{12}{B_{\alpha\beta} R_{ij}})^{12} \right] \\ &+ \sum_{i>j} (\frac{q_i q_j}{4\pi\epsilon_0 R_{ij}}). \end{aligned} \tag{6.1}$$

However, the pair_style *buck* available in LAMMPS *does not* include the repulsion term.

$$U_{Buck} = Ae^{-R/\rho} - CR^{-6}, R < R_{cut}. \tag{6.2}$$

We incorporated the R^{-12} repulsion term *without modifying the LAMMPS source code* by adding a Lennard-Jones 12-6 term,

$$U_{Lj} = 4\epsilon \left[(\frac{\sigma}{R})^{12} - (\frac{\sigma}{R})^{6} \right], R < R_{cut}. \tag{6.3}$$

This was accomplished by using the *hybrid/overlay* command with the pair_styles *buck* and *lj*. The Coulomb potential is unaffected by this procedure and thus is not mentioned further in what follows.

The combination of the pair_styles *buck* and *lj* must satisfy the following requirements:

- The sum of the coefficients of the two R^{-6} terms in Eqs. 6.2 and 6.3 must equal the coefficient $C_{\alpha\beta}$ in the original force field (Eq. 6.1).
- The coefficient of the R^{-12} term in Eq. 6.3 must be equal to the value $D(\frac{12}{B_{\alpha\beta}})^{12}$ that appears in the original force field (Eq. 6.1).

There exists an infinite number of combinations for parameters C, ϵ, and σ that satisfy these two requirements. We chose to set $\epsilon = \frac{D}{4}$ and $\sigma = \frac{12}{B_{\alpha\beta}}$ for the pair_style *lj* (Eq. 6.3). For pair_style *buck*, the parameters A and ρ in Eq. 6.2 are set to the same values as $A_{\alpha\beta}$ and $1/B_{\alpha\beta}$, respectively, in Eq. 6.1. With these choices, the parameter C is given by:

$$C = C_{\alpha\beta} - 4\epsilon\sigma^6 = C_{\alpha\beta} - D(\frac{12}{B_{\alpha\beta}})^6. \tag{6.4}$$

6.2 Appendix II: LAMMPS Input Syntax and Coefficient Values for Implementing Eq. 6.1 in terms of Eqs. 6.2 and 6.3

Figure 6.1 depicts the structure of a TATB molecule and identifies the six atoms types used. Following the figure, LAMMPS input file syntax is provided that implements Eq. 6.1 in terms of Eqs. 6.2 and 6.3.

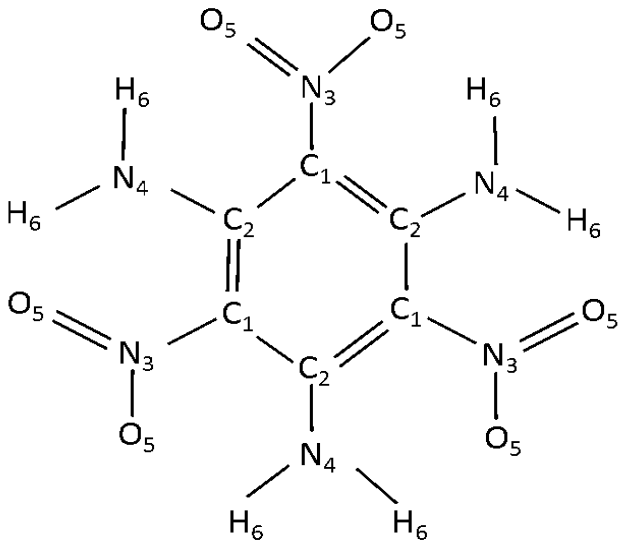

Figure 6.1: TATB atom types.

pair_style hybrid/overlay buck 11.0 lj/cut 11.0 coul/wolf 0.2 11.0

pair_coeff 1 1 buck 107023.9 0.27469 553.95

pair_coeff 1 1 lj/cut 0.0000125 3.2963

pair_coeff 1 2 buck 107023.9 0.27469 553.95

pair_coeff 1 2 lj/cut 0.0000125 3.2963

pair_coeff 1 3 buck 37103.2 0.28873 484.21

pair_coeff 1 3 lj/cut 0.0000125 3.4647

pair_coeff 1 4 buck 62222.2 0.28969 679.44

pair_coeff 1 4 lj/cut 0.0000125 3.4763

pair_coeff 1 5 buck 41281.1 0.27453 363.87

pair_coeff 1 5 lj/cut 0.0000125 3.2944

pair_coeff 1 6 buck 16829.5 0.24890 67.49

pair_coeff 1 6 lj/cut 0.0000125 2.9867

pair_coeff 2 2 buck 107023.9 0.27469 553.95

pair_coeff 2 2 lj/cut 0.0000125 3.2963

pair_coeff 2 3 buck 37103.2 0.28873 484.21

pair_coeff 2 3 lj/cut 0.0000125 3.4647

pair_coeff 2 4 buck 62222.2 0.28969 679.44

pair_coeff 2 4 lj/cut 0.0000125 3.4763

pair_coeff 2 5 buck 41281.1 0.27453 363.87

pair_coeff 2 5 lj/cut 0.0000125 3.2944

pair_coeff 2 6 buck 16829.5 0.24890 67.49

pair_coeff 2 6 lj/cut 0.0000125 2.9867

pair_coeff 3 3 buck 13783.9 0.30000 423.25

pair_coeff 3 3 lj/cut 0.0000125 3.6000

pair_coeff 3 4 buck 23210.0 0.30080 593.91

pair_coeff 3 4 lj/cut 0.0000125 3.6096

pair_coeff 3 5 buck 14298.9 0.28861 318.05

pair_coeff 3 5 lj/cut 0.0000125 3.4633

pair_coeff 3 6 buck 4827.6 0.27001 58.97

pair_coeff 3 6 lj/cut 0.0000125 3.2401

pair_coeff 4 4 buck 39091.8 0.30159 833.37

pair_coeff 4 4 lj/cut 0.0000125 3.6190

pair_coeff 4 5 buck 23978.2 0.28957 446.30

pair_coeff 4 5 lj/cut 0.0000125 3.4748

pair_coeff 4 6 buck 8017.4 0.27135 82.76

pair_coeff 4 6 lj/cut 0.0000125 3.2562

pair_coeff 5 5 buck 15923.1 0.27438 239.01

pair_coeff 5 5 lj/cut 0.0000125 3.2925

pair_coeff 5 6 buck 6509.2 0.24864 44.32

pair_coeff 5 6 lj/cut 0.0000125 2.9837

pair_coeff 6 6 buck 7584.2 0.18923 8.22

pair_coeff 6 6 lj/cut 0.0000125 2.2707

pair_coeff * * coul/wolf

6.3 Appendix III: Wolf *vs.* PPPM

For the exactly same system of TATB crystals, NVE dynamics was performed for a single step with a time step of 0.1 fs, where the potential energy of the system was computed using the Particle-Particle-Particle Mesh (PPPM) method and the Wolf summation available in LAMMPS. A comparison of the components of selected atomic forces in the lab frame (Cartesian coordinates) computed using the two methods is shown in Figure 6.2. Atomic forces for the two cases are almost identical. However, the computational time is reduced by a factor of 10 using the Wolf summation for systems discussed in Chapter 2.

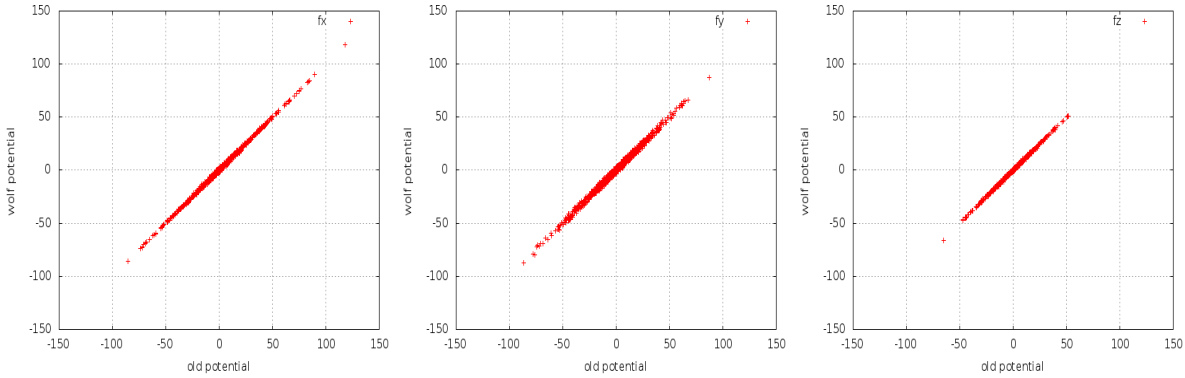

Figure 6.2: Components of atomic forces computed using both the PPPM and Wolf methods.

6.4 Appendix IV: 2D Temperature-Difference Maps at Instants of Complete Pore Collapse

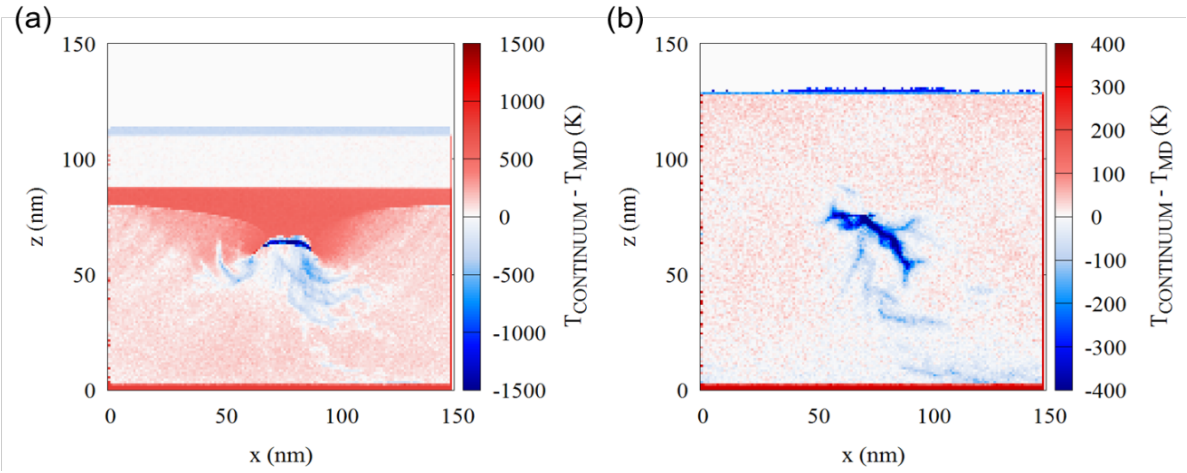

Figure 6.3: 2D maps of the difference between temperatures computed using MD and continuum mechanics, at the instants of complete pore closure, for impact speeds of (a) 2.0 km s^{-1} and (b) 0.5 km s^{-1}. Red indicates higher temperature from continuum mechanics than from MD and blue the opposite situation. White corresponds to zero difference. The color scales for the two panels differ.

Figure 6.3 contains representative 2-D maps of the difference $T_{CONTINUUM} - T_{MD}$ at the respective instants of complete pore closure, for impact speeds of (a) 2.0 km s^{-1} and (b) 0.5 km s^{-1}. Red corresponds to regions where the temperature from continuum mechanics is higher than that from MD. Blue indicates the opposite situation. A temperature difference of zero appears in white. Note that the color scales for the two panels differ. The continuum simulations used the classical specific heat and the melt curve from MD. The MD simulations are for the crystal orientation $\theta = 45°$. A 1 nm $\times$ 1 nm grid resolution was used for the comparison.

The instants of complete pore closure were chosen as well-defined times for comparison *in the frame of the pore collapse*, despite that the physical times for the continuum and MD simulations differ somewhat due to differing shock speeds and pore-collapse rates and mechanisms. The specific instants for the 2.0 km s^{-1} impact

(panel (a)) are $t_{CONTINUUM} = 19.83$ ps and $t_{MD} = 17.9$ ps. Those for the 0.5 km s^{-1} impact (panel (b)) are $t_{CONTINUUM} = 43.29$ ps and $t_{MD} = 45.6$ ps.

The figure suggests that, overall, MD predicts somewhat higher temperatures than continuum mechanics in the vicinity of the collapse, especially for the weaker shock. It also highlights the complicated material mechanics and flow in the MD that is not captured by the isotropic model used in the continuum simulations.

Care is required for the interpretation of the plots for material away from the collapse region, due to effects both of calculating differences at different physical times and because of the Galilean transformation used to bring the two simulations into a common reverse-ballistic frame. For example, focusing on panel (a), the bright red region above the pore, with an essentially white region above it, arises because the lead shock in the continuum simulation has advanced further than for the MD simulation at the respective instants of analysis; the horizontal red-white boundary, and the height of the red region below it, indicates this difference in propagation distance. The white region above the boundary corresponds to a region for which the shock has not arrived in either simulation, thus both the continuum and MD temperatures are 300 K to within statistical fluctuations in the MD. The red strip at the bottom of the panel is due to the piston in the MD. The light blue strip near the top of the panel is an artifact of the Galilean transformation applied to the continuum data: After the transformation, there are no cells in the continuum in that part of the domain. Defining the continuum temperature in such regions to be zero, $T_{CONTINUUM} - T_{MD} = -300$ K.

6.5 Appendix V: Animations of TATB Pore Collapse Simulated Using Molecular Dynamics

Animations of the molecular dynamics simulations of pore collapse are provided in two sets of movie files named as *TATBPoreCollapseRing∗deg#kms.mov* and *TATBPoreCollapseMovie∗deg#kms.mov*, where $*$ represents the crystal orientation and # represents the impact speed. The first set contains all-atom animations of the collapse for concentric, color-coded semi-annuli of material initially in the vicinity of the pore for all nine simulations. The second set contains animations of those same nine simulations, but showing molecular centers of mass for all molecules in the samples. All animations of a given type were prepared with the same physical-time frame rate to facilitate even-handed comparisons when viewed simultaneously. The animations are intended to be viewed in connection with the discussion in Sec. 2.1.2 of the main article.

6.6 Appendix VI: Animations of Strain Functional Analysis on Shock-Compressed TATB Crystals

Animations of the molecular dynamics shock simulations of TATB crystals are provided in movie files named as *SFD_TATBSingleCrystal.mov* (for the 90°-oriented single crystal) and *SFD_TATBPoreCollapse.mov* (for the pore collapse of TATB). Molecules are represented using their COM positions and are classified (colored) using the Strain Functional Analysis. The animations are intended to be viewed in connection with the discussion in Sec. 3.4.1 and Sec. 3.4.2 of the main article.

Bibliography

[1] W. C. Davis. High explosives: the interaction of chemistry and mechanics. *Los Alamos Sci.*, 2:48, 1981.

[2] Y. Deng. *Ancient Chinese Inventions*. Cambridge University Press, Cambridge, England, 2011.

[3] R. Meyer, J. Köhler, and A. Homburg. *Explosives*. Wiley-VCH, Weinheim, 1993.

[4] M. A. Cook. *The Science of High Explosives*. Reinhold Publishing Corporation, New York, NY, 1958.

[5] R. Courant and K. O. Friedrichs. *Supersonic Flow and Shock Waves*. Springer, Verlag, NK, 1976.

[6] P. W. Cooper. *Explosives Engineering*. Wiley, Hoboken, NJ, 1999.

[7] Y. B. Zeldóvich and Y. P. Raizer. *Physics of Shock Waves and High-Temperature Hydrodynamic Phenomena*. Dover Publications, Inc., New York, NY, 2002.

[8] F. P. Bowden and A. D. Yoffe. *Initiation and Growth of Explosion in Liquids and Solids*. Cambridge University Press, Cambridge, England, 1952.

[9] C. H. Johansson and P. A. Persson. *Detonics of High Explosives*. Academic Press, Cambridge, MA, 1970.

[10] C. L. Mader. *Numerical Modeling of Detonations*. University of California Press, Oakland, CA, 1979.

[11] C. L. Mader. *Numerical Modeling of Explosives and Propellants*. CRC Press, Boca Raton, FL, 1998.

[12] W. Fickett and W. C. Davis. *Detonation Theory and Experiment*. Dover Publications, Mineola, NY, 2000.

[13] R. W. Armstrong. Dislocation mechanics aspects of energetic material composites. *Rev. Adv. Mater. Sci.*, 19:13, 2009.

[14] H. Eyring, R. E. Powell, G. H. Duffey, and R. B. Parlin. The stability of detonation. *Chem. Rev.*, 45:69, 1949.

[15] A. W. Campbell, W. C. Davis, J. B. Ramsay, and J. R. Travis. Shock initiation of solid explosives. *Phys. Fluids*, 4:511, 1961.

[16] W. J. M. Rankine. On the thermodynamic theory of waves of finite longitudinal disturbances. *Philo. Trans. Royal Soc.*, 160:277, 1870.

[17] H. Hugoniot. Memoir on the propagation on movements in bodies, especially perfect gases (first part). *J. l'École Polytechnique*, 57:3, 1887.

[18] D. L. Chapman. On the rate of explosion in gases. *Philos. Mag.*, 47:90, 1899.

[19] E. Jouguet. On the propagation of chemical reactions in gases. *J. Math. Pureset Appl.*, 1:347, 1905.

[20] Y. B. Zel'dovich. On the theory of the propagation of detonation waves in gaseous systems. *J. Exp. Theor. Phys. (USSR)*, 10:542, 1940.

[21] J. von Neumann. *Theory of Detonation Waves*, volume Vol. 6. Pergamon Press, New York, NY, 1963.

[22] W. Doering. On detonation processes in gases. *Ann. Phys.*, 43:421, 1943.

[23] J. V. Neumann. Theory of detonation waves, 1942.

[24] N. K. Bourne. On the laser ignition and initiation of explosives. *Proc. R. Soc. Lond. A*, 457:1401, 2001.

[25] J. E. Field, N. K. Bourne, S. J. P. Palmer, and S. M. Walley. Hot spot ignition mechanisms for explosives and propellants. *Philos. Trans. R. Soc. London A*, 339:269, 1992.

[26] J. E. Field. Hot spot ignition mechanisms for explosives. *Acc. Chem. Res.*, 25:489, 1992.

[27] M. P. Allen and D. J. Tildesley. *Computer Simulation of Liquids*. Oxford University Press, New York, NY, 1987.

[28] D. Frenkel and B. Smit. *Understanding Molecular Simulation: from Algorithms to Applications*. Academic Press, San Diego, CA, 2002.

[29] A. Strachan. Normal modes and frequencies from covariances in molecular dynamics or Monte Carlo simulations. *J. Chem. Phys.*, 120:1, 2004.

[30] A. Piryatinski, S. Tretiak, T. D. Sewell, and S. D. McGrane. Vibrational spectroscopy of polyatomic materials: Semiempirical calculations of anharmonic

couplings and infrared and raman linewidths in naphthalene and PETN crystals. *Phys. Rev. B*, 75:214306, 2007.

[31] A. Pereverzev and T. D. Sewell. Terahertz normal mode relaxation in pentaerythritol tetranitrate. *J. Chem. Phys.*, 134:014513, 2011.

[32] A. Pereverzev and T. D. Sewell. Molecular dynamics study of the effect of pressure on the terahertz-region infrared spectrum of crystalline pentaerythritol tetranitrate. *Chem. Phys. Lett.*, 515:32, 2011.

[33] A. Pereverzev, T. D. Sewell, and D. L. Thompson. Molecular dynamics study of the pressure-dependent terahertz infrared absorption spectrum of α- and γ-RDX. *J. Chem. Phys.*, 139:044108, 2013.

[34] A. Pereverzev and T. D. Sewell. Obtaining the hessian from the force covariance matrix: Application to crystalline explosive petn and rdx. *J. Chem. Phys.*, 142:134110, 2015.

[35] A. Pereverzev and T. D. Sewell. A theoretical study of the relaxation of a phenyl group chemisorbed to an RDX freestanding thin film. *J. Chem. Phys.*, 145:054503, 2016.

[36] M. P. Kroonblawd and T. D. Sewell. Theoretical determination of anisotropic thermal conductivity for crystalline 1,3,5-triamino-2,4,6-trinitrobenzene (TATB). *J. Chem. Phys.*, 139:074503, 2013.

[37] M. P. Kroonblawd and T. D. Sewell. Theoretical determination of anisotropic thermal conductivity for initially defect-free and defective TATB single crystals. *J. Chem. Phys.*, 141:184501, 2014.

[38] N. Mathew and T. D. Sewell. Generalized stacking fault energies in the basal plane of triclinic molecular crystal 1,3,5-triamino-2,4,6-trinitrobenzene (TATB). *Philos. Mag.*, 95:424, 2015.

[39] N. Mathew, T. D. Sewell, and D. L. Thompson. Anisotropy in surface-initiated melting of the triclinic molecular crystal 1,3,5-triamino-2,4,6-trinitrobenzene: A molecular dynamics study. *J. Chem. Phys.*, 143:094706, 2015.

[40] M. P. Kroonblawd, T. D. Sewell, and J.-B. Maillet. Characterization of energy exchange between inter- and intramolecular degrees of freedom in crystalline 1,3,5-triamino-2,4,6-trinitrobenzene (TATB) with implications for coarse-grained simulations of shock waves in polyatomic molecular crystals. *J. Chem. Phys.*, 144:064501, 2016.

[41] M. P. Kroonblawd and T. D. Sewell. Predicted anisotropic thermal conductivity for crystalline 1,3,5-triamino-2,4,6-trinitobenzene (TATB): Temperature and pressure dependence and sensitivity to intramolecular force field terms. *Prop., Explos., Pyrotech.*, 41:502, 2016.

[42] N. Mathew and T. D. Sewell. Nanoindentation of the triclinic molecular crystal 1,3,5-triamino-2,4,6-trinitrobenzene: A molecular dynamics study. *J. Phys. Chem. C*, 120:8266, 2016.

[43] M. P. Kroonblawd and T. D. Sewell. Anisotropic relaxation of idealized hot spots in crystalline 1,3,5-triamino-2,4,6-trinitrobenzene (TATB). *J. Phys. Chem. C*, 120:17214, 2016.

[44] N. Mathew, M. P. Kroonblawd, T. D. Sewell, and D. L. Thompson. Predicted melt curve and liquid-state transport properties of TATB from molecular dynamics simulations. *Mol. Simul.*, Published online 2018.

[45] A. Pereverzev and T. D. Sewell. Theoretical analysis of oscillatory terms in lattice heat-current time correlation functions and their contributions to thermal conductivity. *Phys. Rev. B*, 97:104308, 2018.

[46] R. Chitsazi, M. P. Kroonblawd, A. Pereverzev, and T. D. Sewell. A molecular dynamics simulation study of thermal conductivity anisotropy in β-octahydro-1,3,5,7-tetranitro-1,3,5,7-tetrazocine (β-HMX). *Model. Simul. Mater. Sc.*, 28:025008, 2020.

[47] A. Siavosh-Haghighi, R. Dawes, T. D. Sewell, and D. L. Thompson. Shock-induced melting of (100)-oriented nitromethane: Structural relaxation. *J. Chem. Phys.*, 131:064503, 2009.

[48] R. Dawes, A. Siavosh-Haghighi, T. D. Sewell, and D. L. Thompson. Shock-induced melting of (100)-oriented nitromethane: Energy partitioning and vibrational mode heating. *J. Chem. Phys.*, 131:224513, 2009.

[49] A. Siavosh-Haghighi, R. Dawes, T. D. Sewell, and D. L. Thompson. A molecular dynamics study of classical vibrational spectra in hydrostatically compressed crystalline nitromethane. *J. Phys. Chem. B*, 114:17177, 2010.

[50] L. He, T. D. Sewell, and D. L. Thompson. Molecular dynamics simulations of shock waves in oriented nitromethane single crystals. *J. Chem. Phys.*, 134:124506, 2011.

[51] L. He, T. D. Sewell, and D. L. Thompson. Molecular dynamics simulations of shock waves in oriented nitromethane single crystals: Plane-specific effects. *J. Chem. Phys.*, 136:034501, 2012.

[52] L. He, T. D. Sewell, and D. L. Thompson. Molecular dynamics simulations of shock waves in cis-1,4-polybutadiene melts. *J. Appl. Phys.*, 114:163517, 2013.

[53] L. A. Rivera-Rivera, T. D. Sewell, and Thompson D. L. Post-shock relaxation in crystalline nitromethane. *J. Chem. Phys.*, 138:084512, 2013.

[54] S. Jiang, T. D. Sewell, and D. L. Thompson. Molecular dynamics simulations of shock wave propagation through the crystal-melt interface of (100)-oriented nitromethane. *J. Phys. Chem. C*, 120:22989, 2016.

[55] R. M. Eason and T. D. Sewell. Shock-induced inelastic deformation in oriented crystalline pentaerythritol tetranitrate. *J. Phys. Chem. C*, 116:2226, 2011.

[56] R. M. Eason and T. D. Sewell. Molecular dynamics simulations of the collapse of a cylindrical pore in the energetic material α-RDX. *Journal of Dynamic Behavior of Materials*, 1:423, 2015.

[57] M. J. Cawkwell, K. J. Ramos, D. E. Hooks, and T. D. Sewell. Homogeneous dislocation nucleation in cyclotrimethylene trinitramine under shock loading. *J. Appl. Phys.*, 107:063512, 2010.

[58] D. Bedrov, J. B. Hooper, G. D. Smith, and T. D. Sewell. Shock-induced transformations in crystalline RDX: a constant-stress hugoniostat molecular dynamics simulation study. *J. Chem. Phys.*, 131:034712, 2009.

[59] A. Strachan, A. C. T. van Duin, D. Chakraborty, S. Dasgupta, and W. A. Goddard III. Shock waves in high-energy materials: The initial chemical events in nitramine RDX. *Phys. Rev. Lett.*, 91:098301, 2003.

[60] M. A. Wood, M. J. Cherukara, E. M. Kober, and A. Strachan. Ultrafast chemistry under nonequilibrium conditions and the shock to deflagration transition at the nanoscale. *J. Phys. Chem. C*, 119:22008, 2015.

[61] T.-R. Shan and A. P. Thompson. Shock-induced hotspot formation and chemical reaction initiation in PETN containing a spherical void. *J. Phys. Conf. Ser.*, 500:172009, 2014.

[62] T. Zhou, J. Lou, Y. Zhang, H. Song, and F. Huang. Hot spot formation and chemical reaction initiation in shocked HMX crystals with nanovoids: A large-scale reactive molecular dynamics study. *Phys. Chem. Chem. Phys.*, 18:17627, 2016.

[63] M. R. Manaa, L. E. Fried, C. F. Melius, M. Elstner, and Th. Frauenheim. Decomposition of HMX at extreme conditions: A molecular dynamics simulation. *J. Phys. Chem. A*, 106:9024, 2002.

[64] A. Strachan, E. M. Kober, A. C. T. van Duin, J. Oxgaard, and W. A. Goddard III. Thermal decomposition of RDX from reactive molecular dynamics. *J. Chem. Phys.*, 122:054502, 2005.

[65] M. N. Sakano, B. Hamilton, M. M. Islam, and A. Strachan. A role of molecular disorder on the reactivity of RDX. *J. Phys. Chem. C*, 122:27032, 2018.

[66] Y. Long and J. Chen. Systematic study of the reaction kinetics for HMX. *J. Phys. Chem. A*, 119:4073, 2015.

[67] K. Lee, S. Joshi, K. Chaudhuri, and D. S. Stewart. Mirrored continuum and molecular scale simulations of the ignition of high-pressure phase of RDX. *J. Chem. Phys.*, 144:184111, 2016.

[68] L. Liu, Y. Liu, S. V. Zybin, H. Sun, and W. A. Goddard III. Reaxff-*lg*: Correction of the reaxff reactive force field for london dispersion, with applications to the equations of state for energetic materials. *J. Phys. Chem. A*, 115:11016, 2011.

[69] M. N. Sakano, A. Hamed, E. M. Kober, N. Grilli, B. W. Hamilton, M. M. Islam, Koslowski M., and Strachan A. Unsupervised learning-based multiscale model of thermochemistry in 1,3,5-trinitro-1,3,5-triazinane (RDX). *J. Phys. Chem. A*, 124:9141, 2020.

[70] M. P Kroonblawd, N. Mathew, S. Jiang, and T. D. Sewell. A generalized crystal-cutting method for modeling arbitrarily oriented crystals in 3D periodic simulation cells with applications to crystal-crystal interfaces. *Comput. Phys. Commun.*, 207:232, 2016.

[71] T. D. Sewell and C. M. Bennett. Monte carlo calculations of the elastic moduli and pressure-volume-temperature equation of state for hexahydro-1,3,5-trinitro-1,3,5-triazine. *J. App. Phys.*, 88:88, 2000.

[72] O. Borodin, G. D. Smith, T. D. Sewell, and D. Bedrov. Polarizable and non-polarizable force fields for alkyl nitrates. *J. Phys. Chem. B*, 112:734, 2008.

[73] M. J. Cawkwell, T. D. Sewell, L. Zheng, and D. L. Thompson. Shock-induced shear bands in an energetic molecular crystal: Application of shock-front absorbing boundary conditions to molecular dynamics simulations. *Phys. Rev. B*, 78:014107, 2008.

[74] L. Verlet. Computer "Experiments" on classical fluids. I. thermodynamical properties of lennard-jones molecules. *Phys. Rev.*, 159:98, 1967.

[75] W. C. Swope, H. C. Andersen, P. H. Berens, and K. R. Wilson. A computer simulation method for the calculation of equilibrium constants for the formation of physical clusters of molecules: Application to small water clusters. *J. Chem. Phys.*, 76:637, 1982.

[76] E. Hairer, C. Lubich, and G. Wanner. Geometric numerical integration illustrated by the stömer/verlet method. *Acta Numerica*, 12:399, 2003.

[77] S. Plimpton. Fast parallel algorithms for short-range molecular dynamics. *J. Comp. Phys.*, 117:1, 1995.

[78] LAMMPS is available at http://lammps.sandia.gov.

[79] B. L. Holian. Atomistic computer simulations of shock waves. *Shock Waves*, 5:149, 1995.

[80] B. L. Holian and P. S. Lomdahl. Plasticity induced by shock waves in nonequilibrium molecular-dynamics simulations. *Science*, 280:2085, 1998.

[81] V. V. Zhakhovskii, K. Nishihara, and S. I. Anisimov. Shock wave structure in dense gases. *J. Exp. Theor. Phys.*, 66:99, 1997.

[82] E. J. Reed, L. E. Fried, and J. D. Joannopoulos. A method for tractable dynamical studies of single and double shock compression. *Phys. Rev. Lett.*, 23:235503, 2003.

[83] M. D. Nelms, M. P. Kroonblawd, and R. A. Austin. Pore collapse in single-crystal TATB under shock compression. *21st Biennial Conference of the APS Topical Group on Shock Compression of Condens. Matter*, 2019.

[84] P. Zhao, S. Lee, T. Sewell, and H. S. Udaykumar. Tandem molecular dynamics and continuum studies of shock-induced pore collapse in TATB. *Propellants, Explos. Pyrotech.*, 45:1, 2020.

[85] H. H. Cady and A. C. Larson. The crystal structure of 1,3,5-triamino-2,4,6-trinitrobenzene. *Acta Crystallogr.*, 18:485, 1965.

[86] D. Bedrov, O. Borodin, G. D. Smith, T. D. Sewell, D. M. Dattelbaum, and L. L. Stevens. A molecular dynamics simulation study of crystalline 1,3,5-triamino-2,4,6-trinitrobenzene as a function of pressure and temperature. *J. Chem. Phys.*, 131:224703, 2009.

[87] E. F. C. Byrd and B. M. Rice. Ab initio study of compressed 1,3,5,7-tetranitro-1,3,5,7-tetraazacyclooctane (HMX), cyclotrimethylenetrinitramine (RDX), 2,4,6,8,10,12-hexanitrohexaazaisowurzitane (CL-20), 2,4,6-trinitro-1,3,5-benzenetriamine (TATB), and pentaerythritol tetranitrate (PETN). *J. Phys. Chem. C*, 111:2787, 2007.

[88] L. L. Stevens, N. Velisavljevic, D. E. Hooks, and D. M. Dattelbaum. Hydrostatic compression curve for triamino-trinitrobenzene determined to 13.0 GPa with powder X-ray diffraction. *Prop., Explos., Pyrotech.*, 33:286, 2008.

[89] A. C. Landerville, M. W. Conroy, M. M. Budzevich, Y. Lin, C. T. White, and I. I. Oleynik. Equations of state for energetic materials from density functional theory with van der Waals, thermal, and zero-point energy corrections. *Appl. Phys. Lett.*, 97:251908, 2010.

[90] M. Budzevich, M. Conroy, A. Landerville, Y. Lin, I. Oleynik, and C. T. White. Hydrostatic equation of state and anisotropic constitutive relationships in 1,3,5-triamino-2,4,6-trinitrobenzene (TATB). *AIP Conf. Proc.*, 1195:545, 2009.

[91] M. R. Manna and L. E. Fried. Nearly equivalent intra- and intermolecular hydrogen bonding in 1,3,5-triamino-2,4,6-trinitrobenzene at high pressure. *J. Phys. Chem. C*, 116:2116, 2012.

[92] Q. Wu, W. Zhu, and H. Xiao. Comparative DFT- and DFT − D-based molecular dynamics studies of pressure effects in crystalline 1,3,5-triamino-2,4,6-trinitrobenzene at room temperature. *RCS Adv.*, 4:53149, 2014.

[93] I. A. Fedorov and Y. N. Zhuravlev. Hydrostatic pressure effects on structural and electronic properties of TATB from first principles calculations. *Chem. Phys.*, 436:1, 2014.

[94] A. A. Rykounov. Investigation of the pressure dependent thermodynamic and elastic properties of 1,3,5-triamino-2,4,6-trinitrobenzene using dispersion corrected density functional theory. *Appl. Phys. Lett.*, 117:215901, 2015.

[95] T. Plisson, N. Pineau, G. Weck, E. Bruneton, N. Guignot, and P. Loubeyre. Equation of state of 1,3,5-triamino-2,4,6-trinitrobenzene up to 66 GPa. *J. Appl. Phys.*, 122:235901, 2017.

[96] H. Qin, B.-L. Yan, M. Zhong, C.-L. Jiang, F.-S. Liu, B. Tang, and Q.-J. Liu. First-principles study of structural, elastic, and electronic properties of triclinic TATB under different pressures. *Phys. B: Condens. Matter*, 552:151, 2019.

[97] B. A. Steele, S. M. Clarke, M. P. Kroonblawd, I-F. W. Kuo, P. F. Pagoria, S. N. Tkachev, J. S. Smith, S. Bastea, L. E. Fried, J. M. Zaug, E. Stavrou, and Tschauner O. Pressure-induced phase transition in 1,3,5-triamino-2,4,6-trinitrobenzene (TATB). *Appl. Phys. Lett.*, 114:191901, 2019.

[98] D. S. Phillips, B. C. Schwarz, C. B. Skidmore, M. A. Hiskey, and S. F. Son. Some observations on the structure of TATB. *AIP Conf. Proc.*, 505:707, 2000.

[99] D. M. Hoffman and A. T. Fontes. Density distributions in TATB prepared by various methods. *Prop., Explos., Pyrotech.*, 35:15, 2010.

[100] B. S. Mallik, I-F. W. Kuo, L. F. Fried, and J. I. Siepmann. Understanding the solubility of triamino-trinitrobenzene in hydrous tetramethylammonium flouride: A first principles molecular dynamics simulation study. *Phys. Chem. Chem. Phys.*, 14:4884, 2012.

[101] M. Guerain, A. Forzy, Lecardeur A., and H. Trumel. Structure defect evolution of TATB-based comopunds induced by processing operations and thermal treatments. *Prop., Explos., Pyrotech.*, 41:494, 2016.

[102] R. H. Gee, S. Roszak, K. Balasubramanian, and L. E. Fried. *Ab initio* based force field and molecular dynamics simualtions of crystalline TATB. *J. Chem. Phys.*, 120:7059, 2004.

[103] N. Rai, D. Bhatt, J. I. Siepmann, and L. E. Fried. Monte carlo simulations of 1,3,5-triamino-2,4,6-trinitrobenzene (TATB): Pressure and temperature effects for the solid phase and vapor-liquid phase equilibria. *J. Chem. Phys.*, 129:194510, 2008.

[104] C. D. Wick, J. M. Stubbs, N. Rai, and J. I. Siepmann. Transferable potentials for phase equilibria. 7. primary, secondary, tetiary amines, nitroalkanes and nitrobenzene, nitriles, amides, pyridine, and pyrimidine. *J. Phys. Chem. B*, 109:18974, 2005.

[105] P. Lafourcade, C. Denoual, and J.-B. Maillet. Dislocation core structure at finite temperature inferred by molecular dynamics simulations of 1,3,5-triamino-2,4,6-trinitrobenzene single crystal. *J. Phys. Chem. C*, 121:7442, 2017.

[106] P. Lafourcade, C. Denoual, and J.-B. Maillet. Irreversible deformation mechanisms for 1,3,5-triamino-2,4,6-trinitrobenzene single crystal through molecular dynamics simulations. *J. Phys. Chem. C*, 122:14954, 2018.

[107] F. Müller-Plathe. A simple nonequilibrium molecular dynamics method for calculating the thermal conductivity. *J. Chem. Phys.*, 106:6082, 1997.

[108] A. Stolovy, Jr. E. C. Jones, J. B. Aviles, A. I. Namenson, and W. A. Fraser. Exothermic reactions in TATB initiated by an electron beam. *J. Chem. Phys.*, 78:229, 1983.

[109] P. Delavignette. Dissociation and plasticity of layer crystals. *J. Phys. Colloq.*, 35:181, 1974.

[110] S. Amelinckx. *Dislocations in Particular Structure*, volume Vol. 2. North-Holland, Oxford, 1979.

[111] M. R. Taw, J. D. Yeager, D. E. Hoods, T. M. Carvajal, and D. F. Bahr. The mechanical properties of as-grown noncubic organic molecular crystals assessed by nanoindentation. *J. Mater. Res.*, 32:2728, 2017.

[112] P. Zhao, M. P. Kroonblawd, N. Mathew, and T. Sewell. Strongly anisotropic thermomechanical response to shock wave loading in oriented samples of the triclinic molecular crystal 1,3,5-triamino-2,4,6-trinitrobenzene (TATB). *J. Phys. Chem. C*, page To be submitted, 2020.

[113] L. E. Fried and C. Tarver. Molecular dynamics simulation of shocks in porous TATB crystals. *AIP Conf. Proc.*, 370:179, 1996.

[114] L. Zhang, S. V. Zybin, A. C. T. van Duin, S. Dasgupta, W. A. Goddard III, and E. M. Kober. Carbon cluster formation during thermal decomposition of octahydro-1,3,5,7-tetranitro-1,3,5,7-tetrazocine and 1,3,5-triamino-2,4,6-trinitrobenzene high explosives from ReaxFF reactive molecular dynamics simulations. *J. Phys. Chem. A*, 113:10619, 2009.

[115] Y. Long and J. Chen. Theoretical study of the reaction kinetics and the detonation wave profile for 1,3,5-triamino-2,4,6-trinitrobenzene. *J. Appl. Phys.*, 120:185902, 2016.

[116] P. Zhao. Anisotropic shock response of 1,3,5-triamino-2,4,6-trinitrobenzene (TATB), 2018.

[117] E. F. John. Hot spot ignition mechanisms for explosives. *Acc. Chem. Res.*, 25:489, 1992.

[118] C. M. Tarver, S. K. Chidester, and A. L. III Nichols. Critical conditions for impact- and shock-induced hot spots in solid explosives. *J. Phys. Chem.*, 100:5794, 1996.

[119] R. Menikoff. Pore collapse and hot spots in HMX. *AIP Conf. Proc.*, 706:393, 2004.

[120] N. K. Rai and H. S. Udaykumar. Void collapse generated meso-scale energy localization in shocked energetic materials: Non-dimensional parameters, regimes, and criticality of hotspots. *Phys. Fluids*, 31:016103, 2019.

[121] W. Sun, J. E. Andrade, J. W. Rudnicki, and P. Eichhubl. Connecting microstructural attributes and permeability from 3D tomographic images of in situ shear-enhanced compaction bands using multiscale computations. *Geophys. Res. Lett.*, 38:1, 2011.

[122] W. C. Sun, M. R. Kuhn, and J. W. Rudnicki. A multiscale DEM – LBM analysis on permeability evolutions inside a dilatant shear band. *Acta Geotech.*, 8:465, 2013.

[123] A. Barua, S. Kim, Y. Horie, and M. Zhou. Ignition criterion for heterogeneous energetic materials based on hotspot size-temperature threshold. *J. Appl. Phys.*, 113:064906, 2013.

[124] W. Sun and A. Mota. A multiscale overlapped coupling formulation for large-deformation strain localization. *Comput. Mech.*, 54:803, 2014.

[125] S. Kim, C. Miller, Y. Horie, C. Molek, E. Welle, and M. Zhou. Computational prediction of probabilistic ignition threshold of pressed granular octahydro-1,3,5,7-tetranitro-1,2,3,5-tetrazocine (HMX) under shock loading. *J. Appl. Phys.*, 120:115902, 2016.

[126] R. Saurel, F. Fraysse, D. Furfaro, and E. Lapebie. Multiscale multiphase modeling of detonations in condensed energetic materials. *Comput. Fluids*, 159:95, 2017.

[127] O. Sen, N. K. Rai, A. S. Diggs, D. B. Hardin, and H. S. Udaykumar. Multi-scale shock-to-detonation simulation of pressed energetic material: A meso-informed ignition and growth model. *J. Appl. Phys.*, 124:085110, 2018.

[128] M. A. Wood, D. E. Kittell, C. D. Yarrington, and A. P. Thompson. Multiscale modeling of shock wave localization in porous energetic material. *Phys. Rev. B*, 97:014109, 2018.

[129] L. W. Perry, B. Clements, X. Ma, and J. T. Mang. Relating microstructure, temperature, and chemistry to explosive ignition and shock sensitivity. *Combust. Flame*, 190:171, 2018.

[130] S. Kim, Y. Wei, Y. Horie, and M. Zhou. Prediction of shock initiation thresholds and ignition probability of polymer-bonded explosives using mesoscale simulations. *J. Mech. Phys. Solids*, 114:97, 2018.

[131] S. Lee, O. Sen, N. K. Rai, K. K. Gaul, N. J.and Choi, and H. S. Udaykumar. Effects of parametric uncertainty on multi-scale model predictions of shock response of a pressed energetic material. *J. Appl. Phys.*, 125:235104, 2019.

[132] A. Nassar, N. K. Rai, O. Sen, and H. S. Udaykumar. Modeling mesoscale energy localization in shocked HMX, part I: Machine-learned surrogate models for the effects of loading and void sizes. *Shock Waves*, 29:537, 2019.

[133] S. Izvekov, P. W. Chung, and B. M. Rice. The multiscale coarse-graining method: Assessing its accuracy and introducing density dependent coarse-grain potentials. *J. Chem. Phys.*, 133:064109, 2010.

[134] S. Izvekov, M. Sellers, B. Barnes, J. Larentzos, J. Brennan, and B. Rice. Non-equilibrium multiscale coarse-grained simulation of energetic molecular crystalline materials. *Abstracts of Papers of the American Chemical Society*, 250, 2015.

[135] B. C. Barnes, J. K. Brennan, E. F. C. Byrd, S. Izvekov, J. P. Larentzos, and B. M. Rice. *Toward a Predictive Hierarchical Multiscale Modeling Approach for Energetic Materials*. Springer International Publishing, Cham, 2019.

[136] J. K. Brennan, M. Lísal, J. D. Moore, S. Izvekov, I. V. Schweigert, and J. P. Larentzos. Coarse-grain model simulations of nonequilibrium dynamics in heterogeneous materials. *J. Phys. Chem. Lett.*, 5:2144, 2014.

[137] B. C. Barnes, C. E. Spear, K. W. Leiter, R. Becker, J. Knap, M. Lísal, and J. K. Brennan. Hierarchical multiscale framework for materials modeling: Equation of state implementation and application to a taylor anvil impact test of RDX. *AIP Conf. Proc.*, 1793:080001, 2017.

[138] M. S. Sellers, M. Lísal, I. Schweigert, J. P. Larentzos, and J. K. Brennan. Shock simulations of a single-site coarse-grain RDX model using the dissipative particle dynamics method with reactivity. *AIP Conf. Proc.*, 1793:04008, 2017.

[139] N. K. Rai, M. J. Schmidt, and H. S. Udaykumar. High-resolution simulations of cylindrical void collapse in energetic materials: Effect of primary and secondary collapse on initiation thresholds. *Phys. Rev. Fluids*, 2:043202, 2017.

[140] A. Kapahi and H. S. Udaykumar. Three-dimensional simulations of dynamics of void collapse in energetic materials. *Shock Waves*, 25:177, 2015.

[141] N. K. Rai and H. S. Udaykumar. Three-dimensional simulations of void collapse in energetic materials. *Phys. Rev. Fluids*, 3:033201, 2018.

[142] A. Kapahi and H. S. Udaykumar. Dynamics of void collapse in shocked energetic materials: Physics of void-void interactions. *Shock Waves*, 23:537, 2013.

[143] R. A. Austin, N. R. Barton, J. E. Reaugh, and L. E. Fried. Direct numerical simulation of shear localization and decomposition reactions in shock-loaded HMX crystal. *J. Appl. Phys.*, 117:185902, 2015.

[144] N. Grilli, A. Dandekar, and M. Koslowski. Coupling crystal plasticity and phase-field damage to simulate β-HMX-based polymer-bonded explosive under shock load. *APS Shock Compression Condens. Matter*, 2017.

[145] H. K. Springer, S. Bastea, A. L. Nichols, C. M. Tarver, and J. E. Reaugh. Modeling the effects of shock pressure and pore morphology on hot spot mechanisms in HMX. *Propellants, Explos. Pyrotech.*, 43:805, 2018.

[146] N. Grilli and M. Koslowski. The effect of crystal orientation on shock loading of single crystal energetic materials. *Comput. Mater. Sci.*, 155:235, 2018.

[147] C. Duarte, M. Koslowski, and N. Grilli. Symp-Modeling the effect of plasticity and damage in β-HMX single crystals under shock loading. *21st Bienn. Conf. APS Top. Gr. Shock Compression Condens. Matter*, 2019.

[148] S. Roy, N. K. Rai, O. Sen, D. B. Hardin, A. S. Diggs, and H. S. Udaykumar. Modeling meso-scale energy localization in shocked HMX, part II: Training machine-learned surrogate models for void shape and void-void interaction effects. *Shock Waves*, page submitted, 2019.

[149] G. A. Levesque and P. Vitello. The effect of pore morphology on hot spot temperature. *Propellants, Explos. Pyrotech.*, 40:303, 2015.

[150] Springer J. K., C. M. Tarver, and S. Bastea. Effects of high shock pressures and pore morphology on hot spot mechanisms in HMX. *AIP Conf. Proc.*, 1793:080002, 2017.

[151] N. K. Rai, M. J. Schmidt, and H. S. Udaykumar. Collapse of elongated voids in porous energetic materials: Effects of void orientation and aspect ratio on initiation. *Phys. Rev. Fluids*, 2:043201, 2017.

[152] F. Rice and L. Simpson. The unusual stability of TATB: A review of the scientific literature. Technical Report UCRL-LR-103663, 1990.

[153] B. M. Dobratz. The insensitive high explosive triaminotrinitrobenzene (TATB): Development and characterization—1888 to 1994. Technical Report LA-13014-H, 1995.

[154] K. K. Baldridge and J. S. Siegel. Balancing steric and electronic factors in push-pull benzenes: An ab initio study on the molecular structure of 1,3,5-triamino-2,4,6-trinitrobenzene and related compounds. *J. Am. Chem. Soc.*, 115:10782, 1993.

[155] J. R. Kolb and H. F. Rizzo. Growth of 1,3,5-triamino-2,4,6-trinitrobenzene (TATB) I. anisotropic thermal expansion. *Propellants, Explos., Pyrotech.*, 4:10, 1979.

[156] I. G. Voigt-Martin, G. Li, A. A. Yakimanski, J. J. Wolff, and H. Gross. Use of electron diffraction and high-resolution imaging to explain why the non-dipolar 1,3,5-triamino-2,4,6-trinitrobenzene displays strong powder second harmonic generation efficiency. *J. Phys. Chem. A*, 101:7265, 1997.

[157] J. Sun, B. Kang, C. Xue, Y. Liu, Y. Xia, X. Liu, and W. Zhang. Crystal state of 1,3,5-triamino-2,4,6-trinitrobenzene (TATB) undergoing thermal cycling process. *J. Energ. Mater.*, 28:189, 2010.

[158] A. J. Davidson, R. P. Dias, D. M. Dattelbaum, and C. S. Yoo. 'Stubborn' triaminotrinitrobenzene: Unusually high chemical stability of a molecular solid to 150 GPa. *J. Chem. Phys.*, 135:174507, 2011.

[159] D. E. Taylor. Intermolecular forces and molecular dynamics simulation of 1,3,5-triamino-2,4,6-trinitrobenzene (TATB) using symmetry adapted perturbation theory. *J. Phys. Chem. A*, 117:3507, 2013.

[160] C. Zhang. Investigation of the slide of the single layer of the 1,3,5-triamino-2,4,6- trinitrobenzene crystal: Sliding potential and orientation. *J. Phys. Chem. B*, 111:14295, 2007.

[161] C. Zhang, X. Wang, and H. Huang. π-stacked interactions in explosive crystals: Buffers against external mechanical stimuli. *J. Am. Chem. Soc.*, 130:8359, 2008.

[162] M. M. Budzevich, A. C. Landerville, M. W. Conroy, Y. Lin, I. I. Oleynik, and C. T. White. Hydrostatic and uniaxial compression studies of 1,3,5-triamino-

2,4,6-trinitrobenzene using density functional theory with van der Waals correction. *J. Appl. Phys.*, 107:113524, 2010.

[163] O. U. Ojeda and T. Çağn. Hydrogen bonding and molecular rearrangement in 1,3,5-triamino-2,4,6- trinitrobenzene under compression. *J. Phys. Chem. B*, 115:12085, 2011.

[164] L. Valenzano, W. J. Slough, and W. Perger. Accurate prediction of second-order elastic constants from first principles: PETN and TATB. *AIP Conf. Proc.*, 1426:1191, 2012.

[165] H. C. Andersen. Rattle: A 'velocity' version of the shake algorithm for molecular dynamics calculations. *J. Comput. Phys.*, 52:24, 1983.

[166] D. Wolf, P. Keblinski, S. R. Phillpot, and J. Eggebrecht. Exact method for the simulation of coulombic systems by spherically truncated, pairwise r^{-1} summation. *J. Chem. Phys.*, 110:8254, 1999.

[167] E. Bitzek, P. Koskinen, F. Gähler, M. Moseler, and P. Gumbsch. Structural relaxation made simple. *Phys. Rev. Lett.*, 97:170201, 2006.

[168] S. Nosé. A unified formulation of the constant-temperature molecular-dynamics methods. *J. Chem. Phys.*, 81:511, 1984.

[169] W. G. Hoover. Canonical dynamics: Equilibrium phase-space distributions. *Phys. Rev. A*, 31:1695, 1985.

[170] H. S. Udaykumar, L. Tran, D. M. Belk, and K. J. Vanden. An eulerian method for computation of multimaterial impact with ENO shock-capturing and sharp interfaces. *J. Comput. Phys.*, 186:136, 2003.

[171] A. Kapahi, S. Sambasivan, and H. S. Udaykumar. A three-dimensional sharp interface cartesian grid method for solving high speed multi-material impact, penetration and fragmentation problems. *J. Comput. Phys.*, 241:308, 2013.

[172] O. Sen, S. Davis, G. Jacobs, and H. S. Udaykumar. Evaluation of convergence behavior of metamodeling techniques for bridging scales in multi-scale multi-material simulation. *J. Comput. Phys.*, 294:585, 2015.

[173] J. C. Simo and T. J. R. Hughes. *General Return Mapping Algorithms for Rate-Independent Plasticity.* Elsevier, New York, 1987.

[174] F. M. Najjar, W. M. Howard, and L. E. Fried. Grain-scale simulations of hot-spot initiation for shocked TATB. *AIP Conf. Proc.*, 1195:49, 2009.

[175] R. Menikoff and T. D. Sewell. Constituent properties of HMX needed for mesoscale simulations. *Combust. Theory Model.*, 6:103, 2002.

[176] C. Yoo and H. Cynn. Equation of state , phase transition, decomposition of β-HMX (octahydro-1,3,5,7-tetranitro-1,3,5,7-tetrazocine) at high pressures. *J. Chem. Phys.*, 111:10229, 1999.

[177] B. L. Wescott, D. S. Stewart, and W. C. Davis. Equation of state and reaction rate for condensed-phase explosives. *J. Appl. Phys.*, 98:053514, 2005.

[178] R. P. Fedkiw, B. Aslam, T. adn Merriman, and S. Osher. A non-oscillatory eulerian approach to interfaces in multimaterial flows (the ghost fluid method). *J. Comput. Phys.*, 152:457, 1999.

[179] S. Osher and J. A. Sethian. Fronts propagating with curvature-dependent speed: Algorithms based on Hamilton-Jacobi formulations. *J. Comput. Phys.*, 79:12, 1988.

[180] L. B. Tran and H. S. Udaykumar. A particle-level set-based sharp interface cartesian grid method for impact, penetration, and void collapse. *J. Comput. Phys.*, 193:469, 2004.

[181] E. L. Lee and C. M. Tarver. Phenomenological model of shock initiation in heterogeneous explosives. *Phys. Fluids*, 23:2362, 1980.

[182] R. Menikoff and M. S. Shaw. The surf model and the curvature effect for PBX 9502. *Combust. Theory Model.*, 16:1140, 2012.

[183] T. D. Aslam. The reactants equation of state for the tri-amino-tri-nitro-benzene ($/rmTATB$) based explosive PBX 9502. *J. Appl. Phys.*, 122:035902, 2017.

[184] J. D. Honeycutt and Andersen H. C. Molecular dynamics study of melting and freezing of small Lennard-Jones clusters. *J. Phys. Chem.*, 91:4950, 1987.

[185] A. Stukowski. Structure identification methods for atomistic simulations of crystalline materials. *Model. Simul. Mater. Sci. Eng.*, 20:045021, 2012.

[186] C. Kelchner, S. Plimpton, and J. Hamilton. Dislocation nucleation and defect structure during surface indentation. *Phys. Rev. B*, 58:85, 1998.

[187] P. Steinhardt, D. Nelson, and M. Ronchetti. Bond-orientational order in liquids and glasses. *Phys. Rev. B*, 28:784, 1983.

[188] G. J. Ackland and A. P. Jones. Applications of local crystal structure measures in experiment and simulation. *Phys. Rev. B*, 73:054104, 2006.

[189] E. Maras, O. Trushin, A. Stukowski, T. Ala-Nissila, and H. Jónsson. Global transition path search for dislocation formation in Ge on Si (001). *Comput. Phys. Commun.*, 205:13, 2016.

[190] G Voronoi. Nouvelles applications des paramètres continus à la théorie des formes quadratiques. *J. Reine Angew. Math*, 133:97, 1907.

[191] A. S. Keys, C. R. Iacovella, and S. C. Glotzer. Characterizing complex particle morphologies through shape matching: Descriptors, applications, and algorithms. *J. Comput. Phys.*, 230:6438, 2011.

[192] P. M. Larsen, S. Schmidt, and J. Schiøtz. Robust structural identification via polyhedral template matching. *Model. Simul. Mater. Sci. Eng.*, 24:055007, 2016.

[193] A. Stukowski, V. V. Bulatov, and A. Arsenlis. Automated identification and indexing of dislocations in crystal interfaces. *Model. Simul. Mater. Sci. Eng.*, 20:085007, 2012.

[194] A. Stukowski. A triangulation-based method to identify dislocations in atomistic models. *J. Mech. Phys. Solids*, 70:314, 2014.

[195] C. Begau, J. Hua, and A. Hartmaier. A novel approach to study dislocation density tensors and lattice rotation patterns in atomistic simulations. *J. Mech. Phys. Solids*, 60:711, 2012.

[196] E. A. Lazar, J. Han, and D. J. Srolovitz. Topological framework for local structure analysis in condensed matter. *Proc. Natl. Acad. Sci.*, 112:5769, 2015.

[197] A. P. Bartók, M. C. Payne, R. Kondor, and G. Csányi. Gaussian approximation potentials: The accuracy of quantum mechanics, without the electrons. *Phys. Rev. Lett.*, 104:136403, 2010.

[198] A. P. Bartók, R. Kondor, and G. Csányi. On representig chemical environments. *Phys. Rev. B*, 87:184115, 2013.

[199] W. J. Szlachta, A. P. Bartók, and G. Csányi. Accuracy and transferability of Gaussian approximation potential models for tungsten. *Phys. Rev. B*, 90:104108, 2014.

[200] V. L. Deringer and G. Csányi. Machine learning based interatomic potential for amorphous carbon. *Phys. Rev. B*, 95:094203, 2017.

[201] S. De, A. P. Bartók, G. Csányi, and M. Ceriotti. Comparing molecules and solids across structural and alchemical space. *Phys. Chem. Chem. Phys.*, 18:13754, 2016.

[202] C. W. Rosenbrock, E. R. Homer, G. Csányi, and G. L. W. Hart. Discovering the building blocks of atomic systems using machine learning: Application to grain boundaries. *Npj Comput. Mater.*, 3:29, 2017.

[203] A. Stukowski. Computational analysis methods in atomistic modeling of crystals. *JOM*, 66:399, 2014.

[204] N. Mathew, J. P. Adams, C. M .and Tavenner, and E. M. Kober. Development of strain functionals to characterize atomistic simulations. *To be submitted*, 2020.

[205] F. A. Sadjadi and E. L. Hall. Three-dimensional moment invariants. *IEEE Trans. Pattern Anal. Mach. Intell.*, PAMI-2:127, 1980.

[206] A. P. Thompson, L. P. Swiler, C. R. Trott, S. M. Foiles, and G. J. Tucker. Spectral neighbor analysis method for automated generation of quantum-accurate interatomic potential. *J. Comput. Phys.*, 285:316, 2015.

[207] M. A. Wood and A. P. Thompson. Extending the accuracy of the SNAP interatomic potential form. *J. Chem. Phys.*, 148:241721, 2018.

[208] A. V. Shapeev. Moment tensor potentials: A class of systematically improvable interatomic potentials. *Multiscale Model. Simul.*, 14:1153, 2016.

[209] E. V. Podryabinkin and A. V. Shapeev. Active learning of linearly parametrized interatomic potentials. *Comput. Mater. Sci.*, 140:171, 2017.

[210] C.-H. Lo and H.-S. Don. 3-D moment forms: Their construction and application to object identification and positioning. *IEEE Trans. Pattern Anal. Mach. Intell.*, 11:1053, 1989.

[211] A. R. Edmonds. *Angular Momentum in Quantum Mechanics*. Princeton University Press, Princeton, NJ, 3rd edition, 1974.

[212] J. Jerphagnon, D. Chemla, and R. Bonneville. The description of the physical properties of condensed matter using irreducible tensors. *Adv. Phys.*, 27:609, 1978.

[213] M. Arroyo and M. Ortiz. Local *Maximum-Entropy* approximation schemes: A seamless bridge between finite elements and meshfree methods. *Int. J. Number. Methods Eng.*, 65:2167, 2006.

[214] K. Pearson. On lines and planes of closest fit to systems of points in space. *Philos. Mag.*, 2:559, 1901.

[215] C. M. Bishop. *Pattern Recognition and Machine Learning*. Springer-Verlag, Berlin, Heidelberg, 2006.

[216] F. Pedregosa, G. Varoquaux, A. Gramfort, V. Michel, B. Thirion, O. Grisel, M. Bolndel, P. Prettenhofer, R. Weiss, V. Dubourg, J. Vanderplas, A. Passos, D. Cournapeau, M. Brucher, M. Perrot, and E. Duchesnay. Scikit-learn: Machine learning in python. *J. Mach. Learn. Res.*, 12:2825, 2011.

[217] A. Stukowski. Visualization and analysis of atomistic simulation data with ovito - the open visualization tool. *Modeling Simul. Mater. Sci. Eng.*, 18:015012, 2010.

[218] J. A. Zimmerman, C. L. Kelchner, P. A. Klein, J. C. Hamilton, and S. M. Foiles. Surface step effects on nanoindentation. *Phys. Rev. Lett.*, 87:1, 2001.

[219] E. Jaramillo, T. D. Sewell, and A. Strachan. Atomic-level view of inelastic deformation in a shock loaded molecular crystal. *Phys. Rev. B*, 76:064112, 2007.

[220] S. P. Lloyd. Least squares quantization in PCM. *IEEE Trans. Inf. Theory*, 28:129, 1982.

[221] E. W. Forgy. Cluster analysis of multivariate data: Efficiency versus interpretability of classifications. *Biometrics*, 21:768, 1965.

[222] N. S. Altman. An introduction to kernel and nearest-neighbor nonparametric regression. *Am. Stat.*, 46:175, 1992.

[223] R. W. Hockney and J. W. Eastwood. *Computer Simulation Using Particles*. Hilger, New York, NY, 1988.

[224] C. J. Fennell and J. D. Gezelter. Is the Ewald summation still necessary? Pairwise alternatives to the accepted standard for long-range electrostatics. *J. Chem. Phys.*, 124:234104, 2006.

[225] G. D. Smith and R. K. Bharadwaj. Quantum chemistry based force field for simulations of HMX. *J. Phys. Chem. B*, 103:3570, 1999.

[226] D. Bedrov, G. D. Smith, and T. D. Sewell. Thermal conductivity of liquid octahydro-1,3,57-tetranitro-1,3,5,7-tetrazocine (HMX) from molecular dynamics simulations. *Chem. Phys. Lett.*, 324:64, 2000.

VITA

Puhan Zhao was born in Beijing, China. She came to St. Louis, Missouri in 2005. After graduating from Clayton High School in 2009, she entered Truman State University and received the Bachelor of Science degree in Chemistry in 2013. Later, she continued her education at University of Missouri-Columbia, where she received both the Master of Science and PhD. in Chemistry under the guidance of Prof. Tommy Sewell. During the summer of 2019, she did an internship with Dr. Edward Kober in the Theoretical Division of the Los Alamos National Laboratory. She will continue her post-doctoral research with Prof. Sewell.